Barker, P.F., Camerlenghi, A., Acton, G.D., et al., 1999
Proceedings of the Ocean Drilling Program, Initial Reports Volume 178

8. Site 1101[1]

Shipboard Scientific Party[2]

BACKGROUND AND SCIENTIFIC OBJECTIVES

Site 1101 (Fig. **F1**) lies on sediment Drift 4 (Rebesco et al., 1996, 1997) approximately midway between proposed sites APSHE-05A and APSHE-06A, alternates of Sites 1096 and 1095, respectively.

The opportunity to drill another site on the continental rise of the Pacific margin of the Antarctic Peninsula arose from the persistently unfavorable sea state encountered on the continental shelf while attempting to drill Site 1100 (vessel heave during drilling in shallow water is restricted to 2 m). Site 1101 was chosen to provide answers to questions raised by drilling at Sites 1095 and 1096. Clearance to drill the new location was received from the Ocean Drilling Program on 14 March 1998.

The questions that motivated drilling at Site 1101 were

1. Is the sedimentary record from the late Miocene to present obtained at Sites 1095 and 1096 representative of the entire Pacific margin of the Antarctic Peninsula? Does the regional correlation between seismic units observed in multichannel seismic (MCS) profiles (Rebesco et al., 1997) reflect actual litho- and biostratigraphic correlation?
2. Is there evidence for the late Pliocene Eltanin meteorite impact (Gersonde et al., 1997)? At Site 1096, sedimentary evidence of the meteorite impact may exist in the form of a coarse and well-sorted massive sand bed in a predominantly fine muddy sedimentary sequence. An additional site on the continental rise would test this possibility by seeking a similar anomalous, coeval event.

Site 1101 lies on seismic profile IT92-114 (Fig. **F2; "Appendix,"** p. 24, and Fig. **AF1,** p. 59, both in the "Leg 178 Summary" chapter), where the

F1. Location of Site 1101 on Drift 4 with MCS profile IT92-114 and 3.5-kHz profile, **p. 25.**

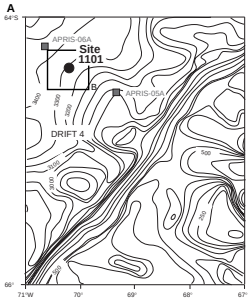

F2. Seismic windows at proposed sites APRIS-06A and -05A, **p. 27.**

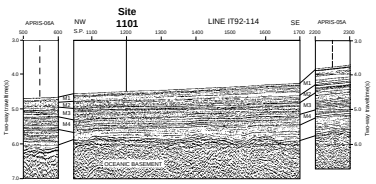

[1]Examples of how to reference the whole or part of this volume.
[2]Shipboard Scientific Party addresses.

uppermost seismic Unit M1 (inferred age: late Pliocene to present) lies within reach of the advanced hydraulic piston corer (APC) at ~200 meters below seafloor (mbsf). It is also within a GLORIA survey of the northeastern part of the upper rise (Tomlinson et al., 1992; Rebesco et al., 1996). The base of Unit M1 lies at ~330 mbsf at proposed site APRIS-05A and ~130 mbsf at APRIS-06A (the two original sites on Drift 4). Site 1101 lies in a water depth of 3280 m, 32.5 km southeast of site APRIS-06A and 52.5 km northwest of site APRIS-05A.

In addition, we considered that if the unfavorable sea state for continental shelf drilling continued, Site 1101 could be deepened to penetrate the Miocene Unit M3, below ~350 mbsf, and possibly even M4 at much greater depth beneath an acoustically anomalous Pliocene M2 unit.

The 3.5-kHz sub-bottom profiler record acquired on approach to Site 1101 (Fig. F3) shows a gently dipping, smooth seafloor, with acoustic penetration of ~50 ms (40 m) through parallel reflectors.

F3. 3.5-kHz sub-bottom profile across Site 1101, acquired during site approach, p. 28.

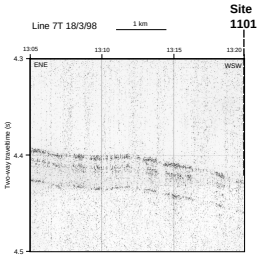

OPERATIONS

Site 1101 (located between scientific prospectus sites APRIS-05A and -06A) was selected as an additional site, where several leg objectives could be accomplished while waiting for the heave to subside on the continental shelf. Hence, the order of events included leaving Hole 1100D at 2030 hr on 17 March, arriving at Site 1101 at 1030 hr on 18 March, conducting coring operations, and then returning to Hole 1100D (see "Operations," p. 3, in the "Shelf Transect [Sites 1100, 1102, and 1103]" chapter). The 122-nmi transit to Site 1101 was accomplished at an average speed of 8.8 kt, slower than normal because the ship traveled through a 5-m swell combined with 2.3-m seas.

Hole 1101A

Hole 1101A was spudded at 1805 hr on 18 March with a standard APC/extended core barrel (XCB) bottom-hole assembly and C-3 bit. Water depth was estimated from recovery of the mudline in Core 1H as 3291.2 m. APC coring advanced to 142.7 mbsf (Core 16H); XCB coring continued to 217.7 mbsf (Core 24X), with 99.1% core recovery for the hole (Table T1). Adara tool temperature estimates were made with Cores 1H, 2H, 4H, 7H, and 10H, and the first two deployments also measured bottom-water temperature. The ship then abandoned Hole 1101A and returned to Hole 1100D for what appeared to be favorable weather over the continental shelf sites. The beacon was recovered and the drilling equipment secured for transit back to Site 1100 by 0145 hr on 20 March. For a summary of drilling at Site 1101, see Table T1, p. 54, in the "Leg 178 Summary" chapter.

T1. Site 1101 coring summary, p. 64.

LITHOSTRATIGRAPHY

At Site 1101, 217.7 m of predominantly hemipelagic clayey silts were drilled at a distal site within Drift 4 on the Antarctic Peninsula continental rise (Rebesco et al., 1996, 1997). The sediments of Site 1101 contain a nearly continuous distal glacial record of the past 3.1 m.y. and can be divided into three lithostratigraphic units (Fig. F4). Unit I (0–53.3 mbsf) and Unit II (53.3–142.7 mbsf) are composed of alternating

F4. Lithostratigraphic column for Site 1101 including percent biogenic component, p. 29.

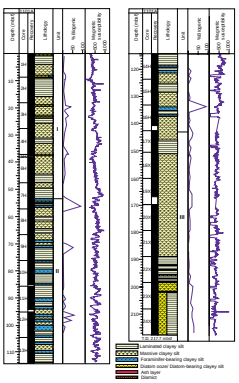

biogenic-bearing massive clayey silts and laminated clayey silts that are interpreted to have been deposited during interglacial and glacial periods, respectively. Within Unit I, diatom-bearing layers are correlated to warm oxygen isotope stages. Unit II has at least 19 discrete foraminifer-bearing layers that alternate cyclically with barren laminated or massive intervals. These biogenic intervals are interpreted to represent interglacials, during which varying controls on marine productivity and oceanographic conditions resulted in calcareous instead of siliceous biogenic sedimentation in Unit II. Unit III (142.7–217.7 mbsf) lacks the regular alternation of biogenic and terrigenous intervals observed in the overlying units. Above 198 mbsf in Unit III, the biogenic component is low, and massive clayey silt and diamict occur. The diamict facies was deposited directly under glacial influence by iceberg rafting, and the associated massive barren facies could have been rapidly deposited by turbid plumes or sediment gravity flows from glaciers near the edge of the continental shelf. The lower part of Unit III may represent a warmer interval with deposition of diatom-bearing massive and laminated facies.

Unit I

Interval: Core 178-1101A-1H through Section 7H-4, 110 cm
Age: Holocene–late Pleistocene (0.0–0.76 Ma)
Depth: 0.0–53.3 mbsf

Description

Unit I consists of 53.3 m of fine-grained sediments, primarily clayey silt (83% of Unit I) and silty clay (17% of Unit I; Figs. F4, F5). Silt laminae, 1–2 mm thick, occur throughout Unit I but form only a minor part of the total thickness. Three normally graded silt beds (as much as 3 cm thick) occur within Cores 178-1101A-2H and 4H. A 3-cm-thick graded bed of volcanic ash with a sharp basal contact occurs at 9.82 mbsf (interval 178-1101A-2H-1, 112–115 cm; Fig. F6). Two facies alternate with gradational contacts within Unit I: a massive facies with a variable biogenic component, and a laminated facies. These are described in more detail below.

Massive Facies

Facies M (massive) ranges in color from dark grayish brown (2.5Y 4/2) to olive gray (5Y 4/2) and is characterized by bioturbation indicated by color mottling and burrows. For example, *Planolites* burrows occur in the interval 178-1101A-7H-2, 90–100 cm. Scattered pebbles, granules, and sand are abundant within the massive facies. The biogenic component is variable and includes both diatoms and foraminifers (Fig. F5). Muddy diatom ooze occurs in the upper 20 cm of Core 178-1101A-1H (Fig. F4). An 80-cm-thick bed of diatom-bearing foraminiferal clayey silt occurs in the massive facies at 8.7 mbsf (interval 178-1101A-2H-1, 0–80 cm). Two other thin, diatom-bearing massive beds occur at 19.7 mbsf (interval 178-1101A-3H-1, 0–50 cm) and 23 mbsf (interval 1101A-3H-4, 30–100 cm). A 1.4-m thick, diatom-bearing, massive bed occurs at 28.2 mbsf. Five intervals of massive facies occur in Unit I and range in thickness from 1.5 m to 11 m (Fig. F4).

F5. Sand-silt-clay ratio, percent biogenic and terrigenous, pebble occurrence, and linear sedimentation rate, Site 1101, p. 30.

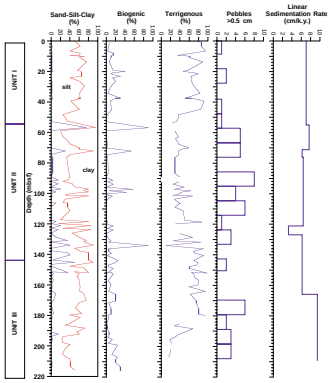

F6. Graded vitric ash bed, interval 178-1101A-2H-1, 103–122 cm, p. 31.

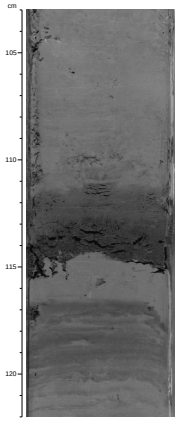

Laminated Facies

Laminated facies, commonly dark gray (5Y 4/1), occur in six intervals, ranging in thickness from 1.6 to 7 m in Unit I (Fig. F4). The facies descriptions used at Sites 1095 and 1096 can also be applied here (see Fig. F9, p. 45, in the "Explanatory Notes" chapter). Most commonly, the laminated facies is formed by faint discontinuous silt lamination, without any repetitive vertical organization, which appears as color banding with variable bioturbation (Facies C, as described at Site 1096) and 1- to 3-mm-thick graded silts with sharp bases (Facies L_2 and L_3). The graded silt laminae occur in groups of 3–7 (Fig. F7). Also within Unit I are three normally graded, thin beds (as much as 5 cm thick) of silt to fine sand (Facies L_1). These beds have sharp basal contacts and grade into the overlying mud.

F7. Laminated facies from interval 178-1101A-2H-3, 49–73 cm, Unit I, p. 32.

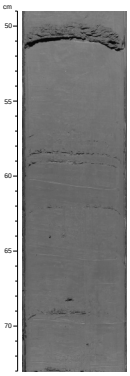

Interpretation

Unit I sediments are dominantly hemipelagic, deposited under a regime of weak bottom currents. Clayey silts with faint discontinuous lamination are interpreted as contourites (similar to Site 1096). The thin groups of silt laminae with sharp bases (L_2) are interpreted as distal muddy turbidites. Low-energy turbidity flows probably deposited the three thicker and more coarsely graded beds. The massive facies record periods of ice-free open water (allowing higher diatom productivity), intense bioturbation, and probably lower sedimentation rates. As at Site 1096, the massive facies with a higher biogenic component is thought to occur during oxygen isotope warm Stages 1 (seafloor sediment), 5e, 7 (occurrence of *Hemidiscus karstenii;* see "Biostratigraphy," p. 9), and 9. Stages 11–17 cannot presently be identified, but Stage 19 coincides with the Brunhes/Matuyama boundary, which is placed at 55.1 mbsf (see "Paleomagnetism," p. 11). A vitric ash layer occurs at the base of Stage 5 and appears very similar to an alkaline ash in an equivalent stratigraphic position in piston cores from near Site 1095 (Fig. F6; Pudsey and Camerlenghi, 1998). Pebbles and dispersed granules and sand were transported to Site 1101 by iceberg rafting (Fig. F5).

Unit II

Interval: Section 178-1101A-7H-4, 110 cm, through Core 16H
Age: late Pleistocene–late Pliocene (0.76–2.2 Ma)
Depth: 53.3–142.7 mbsf

Description

Unit II is 89.4 m thick and begins at the first occurrence downcore of foraminifer-bearing silty clay (Fig. F4). Massive and laminated facies alternate throughout the unit as discussed below. Within Unit II, 19 discrete layers of foraminifer-bearing, massive clayey silt or silty clay occur, ranging in thickness from 45 to 171 cm. Each of these layers corresponds to a trough in the magnetic susceptibility curve (Fig. F8), which is expected because the addition of carbonate to this primarily terrigenous sediment should produce lower magnetic susceptibility (see "Physical Properties," p. 15). The foraminifer-bearing intervals are also lighter in color, and each corresponds to a peak in the chromaticity parameter b* and in percent carbonate (Fig. F8; see "Organic Geochemistry," p. 12; Table T2). The magnetic susceptibility curve shows two more troughs,

F8. Magnetic susceptibility data, chromaticity parameter b*, and percent carbonate for Unit II, p. 33.

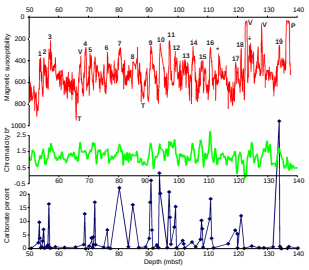

T2. Relative intensities of X-ray diffraction peaks and percent $CaCO_3$ from bulk mineral samples, p. 65.

which do not correspond to observed foraminifer-bearing intervals. These occur near core boundaries, which are disturbed and where sediment may have been lost. Therefore, it is likely that 21 foraminifer-bearing intervals are present within Unit II at Site 1101. However, we cannot verify that we have recovered the entire sediment record because only a single APC hole was drilled at this site.

Massive Facies

Massive facies can be subdivided into foraminifer-bearing (Mf) and barren (Mb). A massive foraminifer-bearing facies (Mf) with as much as 3% nannofossils is repeated at fairly regular intervals downcore in Unit II (Figs. **F4, F9**). This facies ranges from greenish gray (5Y 5/1) to dark greenish gray (5GY 4/1) and is composed of clayey silt with 10%–90% biogenic component (Fig. **F5**). The coarser grain size of the terrigenous silt fraction and the addition of larger foraminifer tests or fragments produce a rough appearance on the core surface that is visible in core images (Fig. **F9**). In some intervals, foraminifers are abundant enough for the sediment to be classified as an ooze, and the tests can be clearly seen on the core surface using a hand lens. Mf is from structureless to burrow mottled with scattered sand and granules. *Zoophycos* and *Planolites* burrows occur within Mf. Massive barren facies (Mb) has the same characteristics as Mf but lacks the foraminifer biogenic component.

Laminated Facies

The laminated facies within Unit II is dark greenish gray (5GY 4/1) to dark gray (N 4/0) and includes three different subfacies. The most common is Facies C (see **"Lithostratigraphy,"** p. 4, in the "Site 1096" chapter), which contains faint, bioturbated, silty lamination that sometimes appears as faint color banding (Fig. **F10**). The second, less common, facies is sharp-based, parallel-laminated, 1- to 3-mm graded silts (Facies L_2 above; Fig. **F10**). In some laminated intervals, such as in Core 178-1101A-10H, Facies C occurs between regularly spaced L_2 facies (Fig. **F10**). Thicker beds of coarse silt or fine sand grading into mud (Facies L_1) occur uncommonly in Unit II. These beds range in thickness from 0.5 to 4 cm and have irregular sharp (erosive?) basal contacts and fairly sharp upper contacts (Fig. **F11**). The thicker beds occur at 66 mbsf (Section 178-1101A-8H-5), 87.6 mbsf (Section 178-1101A-11H-2), 116.7 mbsf (Section 178-1101A-14H-2), and 136.8 mbsf (Section 178-1101A-16H-3). The 4-cm silt bed at 136.8 mbsf is cemented with carbonate and is the only lithified interval in Unit II.

Laminated intervals correspond to high-frequency peaks in the magnetic susceptibility curve (see **"Physical Properties,"** p. 15). The highest peaks corresponding to the thicker, coarser grained beds are especially noticeable (Fig. **F8**). The carbonate silt bed at the base of Unit II (Core 178-1101A-16H) produces a trough because of its higher carbonate content compared to the rest of the laminated intervals.

Interpretation

Massive foraminifer-bearing intervals from Unit II represent a significantly different paleoenvironment from that of the laminated facies (see **"Biostratigraphy,"** p. 9). Both Mf and Mb are deposited from hemipelagic settling of mud from low-density turbid flows, together with biogenic components. Lower sedimentation rates than in laminated intervals are inferred because of the presence of bottom-dwelling infauna that were able to bioturbate the seafloor sediments completely.

F9. Facies Mf, interval 178-1101A-7H-7, 2–20 cm, **p. 34.**

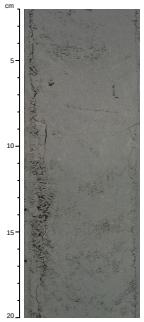

F10. Laminated Facies L_2 and C in interval 178-1101A-10H-6, 17–39 cm, **p. 35.**

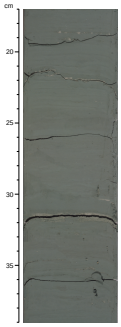

F11. Turbidite, Unit II, interval 178-1101A-14H-2, 97–112 cm, **p. 36.**

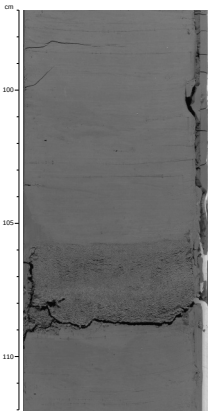

Large amounts of ice-rafted debris appear within massive facies because of the increased flux of coarse-grained sediment delivered by iceberg rafting, relative to fine sediment.

Laminated facies in Unit II include Facies C, which suggests a low-energy setting dominated by contour currents alternating with Facies L_2, indicating distal low-density turbidity currents. Intervals with laminated facies are most common toward the middle of Unit II (Cores 178-1101A-9H through 11H; Fig. F4). In the magnetic susceptibility data, this corresponds to a 20-m-thick interval from 65 to 85 m of regular short-wavelength L_2 peaks separated by troughs corresponding to Mf facies (Fig. F8). The same alternating facies occur above and below this interval, although the repetition is not as regular (Figs. F4, F8). The thicker silt and sand beds are probably distal turbidites deposited at this site by occasional more vigorous turbidity flows.

Unit III

Interval: Cores 178-1101A-17X through 24X
Age: late Pliocene (2.2–3.1 Ma)
Depth: 142.7–217.7 mbsf

Description

Unit III is 75 m thick, ranging from dark greenish gray (5GY 4/1) to brown (5GY 5/1), and composed primarily of massive facies with a low biogenic content (Mb; Fig. F5). Unit III has relatively low magnetic susceptibility and comprises three alternating lithofacies: massive and laminated clayey silt, and diamict (Fig. F4). Foraminifers are not present within this unit, and diatom-bearing silty clay occurs in both massive and laminated lithofacies below 198.5 mbsf (from Section 178-1101A-23X-1 to the bottom of the hole [Fig. F4]). The highest sedimentation rates occur within Unit III (see **"Paleomagnetism,"** p. 11) from 166 mbsf to the bottom of the hole (Fig. F5). Diamict is restricted to an interval between 193 and 202 mbsf (Cores 178-1101A-22X and 23X) interbedded with laminated facies. Pyrite is present in silt laminae and in burrow fills within Unit III. A 6-cm bed of aragonite-cemented silt occurs at 162.7 mbsf. The lithofacies in Unit III are described in detail below.

Massive Facies

The upper part of Unit III is structureless clayey silt (Mb) with minimal bioturbation. Ice-rafted debris increases downcore within the massive interval along with the biogenic component (Fig. F5). Massive diatom-bearing silty clay (Md) occurs near the bottom of the hole (Fig. F4).

Laminated Facies

Laminated Facies C and L_2, similar to those in Units I and II, occur within Unit III. Thin, faint lamination, without any repetitive vertical organization (Facies C), is most common (Fig. F12). This facies is burrowed and shows evidence of minor to moderate bioturbation. Below 198 mbsf, thin "green"-colored (5GY 4/1) parallel silt laminae (as much as 3 mm thick) that contain 15% glauconite occur in diatom-bearing silty clay (an example of Facies L_2). A 5-cm-thick fine sand bed with sharp upper and lower contacts occurs at 206.5 mbsf (Fig. F13). This bed is thicker and coarser grained than all the other beds, and it pro-

F12. Facies C within biscuits of interval 178-1101A-24X-1, 44–64 cm, p. 37.

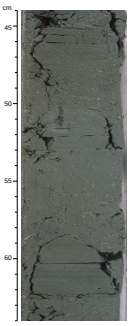

F13. L_1 facies within Unit III, interval 178-1101A-23X-6, 37–59 cm, p. 38.

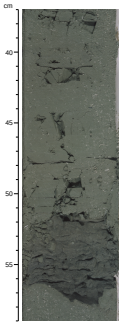

duces the highest magnetic susceptibility value for the entire hole (Fig. F4).

Diamict Facies

Clast-poor diamict (see "Lithostratigraphy," p. 3, in the "Explanatory Notes" chapter for definition) occurs in beds 15–60 cm thick within Cores 178-1101A-22X and 23X (Fig. F14). These dark greenish gray (5GY 4/1) to dark gray (5Y 4/1) clast-poor beds have gradational contacts with the surrounding laminated or massive facies. There is indication of a faint stratification produced by segregation of clasts into bands within the diamict. Each diamict bed appears to have a similar range of clast size, shape, and origin (mostly volcanic and plutonic). In Core 178-1101A-23X, diamict is interbedded with massive diatom-bearing silty clay containing scattered pebbles, granules, and sand.

F14. Diamict facies in Unit III, interval 178-1101A-22X-2, 130–150 cm, p. 39.

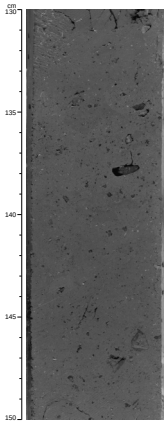

Interpretation

The facies in Unit III were deposited by processes that are similar to those within the other two units, but the sediment flux through the water column was much greater at the bottom of Unit III than higher in the hole. Based on the magnetostratigraphy for Site 1101 (see "Paleomagnetism," p. 11), the sedimentation rate below 166 mbsf is roughly one-third greater than in the top of Unit III (Fig. F6).

As much as 57 m of sediment in Unit III shows strong glacial influences on deposition. The gradational contacts of the diamict and its low clast content indicate that it was deposited by rainout through the water column of sediment transported by icebergs. Because the magnetostratigraphy at Site 1101 indicates that deposition was the most rapid at this time, the presence of the coarse-grained diamict intervals within otherwise fine-grained sediment must represent an intense period of iceberg rafting, not merely a reduction in the flux of fine-grained sediment. The massive barren facies overlying the diamict beds was also deposited rapidly. It is described as structureless, with thin intervals that are thinly laminated (Facies L_2), with generally low magnetic susceptibility values, little evidence of bioturbation, and low biogenic content. For these reasons, Mb facies may have been deposited by different processes from those operating during deposition of the massive facies within Units I and II. One possibility is that Mb originates from deposition from turbid meltwater plumes originating at the grounded glacier terminus on the nearby continental shelf. Similar massive deposits containing ice-rafted debris have been described as plumites and occur on the Labrador Sea continental slope near the outflow of the Laurentide Ice Sheet (Hesse et al., 1997). At the base of the hole, in Core 178-1101A-23X, laminated facies (L_1, L_2, and C) occur, and diatoms are present. Bottom processes and hemipelagic settling were more important than rainout at this time.

Ice-Rafted Debris

Ice-rafted debris occurs throughout Units I, II, and III at Site 1101 (Fig. F6). It is present as scattered sand grains, granules, isolated pebbles (lonestones), and beds of weakly stratified diamict. Pebble abundance is lowest in Unit I, averaging 0–1 pebble per core (Fig. F6). In Unit II, pebbles increase in abundance downcore (to a maximum of 8 per core) until ~90 mbsf, then decrease in number to the base of Unit II. Although in Unit III the total number of pebbles between 0.5 and 6 cm

in diameter is relatively low, the presence of diamict indicates an episode of very high coarse-grained sediment flux to Site 1101 most probably delivered from icebergs during this period. Igneous pebbles with local sources on the Antarctic Peninsula occur most commonly, including volcanic (basalt), volcaniclastic, and intrusive (granite or granodiorite) igneous rocks. One basalt pebble recovered from Section 178-1101A-6H-5 shows striations and a faceted surface, characteristics of subglacial transport (Fig. F15).

F15. Dropstone from Section 178-1101A-6H-5, p. 40.

Depositional Setting of Site 1101

Site 1101 is located on the distal portion of Drift 4 described by Rebesco et al. (1996, 1997). This site was influenced by weak bottom currents and appears to have been an area of near-continuous deposition over the period sampled (see "Seismic Stratigraphy," p. 20). Site 1101 contains a record of glacial–interglacial climate history on the Antarctic Peninsula over the past 3.1 m.y. Available evidence suggests that the ice sheet on the Antarctic Peninsula is highly responsive to climatic variations (Larter and Barker, 1991b; Bart and Anderson, 1995). Within Units I and II, massive, biogenic-enriched facies and laminated facies appear to alternate in a regular pattern similar to the glacial–interglacial facies described in the Australian-Antarctic Basin during Leg 119 (Ehrmann and Grobe, 1991). By analogy with those sediments, the laminated facies at Site 1101 represents increased downslope sediment transport from the shelf (turbidites), a higher terrigenous sediment flux, and low biogenic productivity that accompany glacial periods. Massive facies, with a high biogenic component (both diatoms and foraminifers), bioturbation, and high amounts of ice-rafted debris represent deposition during interglacial periods when less sediment was transported from the continental shelf and sea ice extent was less, so that marine productivity was high. The extension of this facies interpretation to the Antarctic Peninsula is further supported by identification of warm oxygen isotope Stages 1 and 5 within massive biogenic-rich facies in piston cores from Drift 7 (Pudsey and Camerlenghi, 1998).

Another significant climate signal is the presence of foraminifers within the massive facies of Unit II. Today, calcareous biogenic sediment is deposited north of the Polar Front and siliceous tests dominate sediments south of the Polar Front; foraminifers are common in deep-water sediments only in a few areas such as the southeastern Weddell Sea (Mackensen et al., 1989). Although the factors that influence biogenic accumulation are complex, the record appears to indicate regular glacial–interglacial cycles during the deposition of Unit II that were of a different form from those recorded by Units I and III, above and below, which do not contain regular foraminifer-bearing layers (see "Biostratigraphy," p. 9).

Unit III does not have biogenic-enriched facies that alternate in a regular pattern downcore. The upper part of Unit III (142.7 to 198.5 mbsf) is mostly massive clayey silt with a low biogenic content, together with thin beds of diamict. This interval coincides with the highest sedimentation rates in the core (see "Paleomagnetism," p. 11) and appears to be strongly glacially influenced, with intense rainout from icebergs depositing the diamict facies. Multichannel seismic profiles show the thickness of Unit III increasing landward, which supports a continental shelf or slope source for these sediments (see "Seismic Stratigraphy," p. 20). The massive clayey silt in Unit III may have been rapidly deposited from turbid meltwater plumes (plumites). At the base

of Unit III, both massive and laminated facies are diatom-bearing, indicating a less direct glacial influence. Within the laminated facies at 206.5 mbsf, an 8-cm-thick sand bed occurs that is interpreted as a turbidite.

BIOSTRATIGRAPHY

At Site 1101, 217.7 m of Pleistocene and Pliocene hemipelagic silty clays was recovered. Four microfossil groups were present. Calcareous nannofossils and foraminifers were found in the uppermost core as well as in the more biocalcareous interval from 50 to 134 mbsf (approximately Unit II; **"Lithostratigraphy,"** p. 2). Siliceous microfossils, diatoms and radiolarians, were found throughout the hole and became more abundant in the lowest three cores.

Diatoms

Diatom preservation and abundance varied in Hole 1101A. Intervals of abundant to common, well-preserved diatoms alternated with barren ones. Fragmentation of valves is common in the upper 160 m of Hole 1101A. Diatoms were more abundant in samples below Core 178-1101A-19X than in the upper part of the hole. The lowest three cores (Cores 178-1101A-22X, 23X, and 24X) contained a diverse, open-marine assemblage. All zones from the Pleistocene to the late Pliocene were identified at Site 1101 (Fig. **F16**). Table **T3** lists the diatom datums noted at this site; datum intervals are listed with both their position within the cores and their depth (mbsf).

The Pleistocene species *Hemidiscus karstenii* was observed only in Core 178-1101A-3H, placing the first occurrence (FO) and last occurrence (LO) of this species within this core. The LO of *Actinocyclus ingens* was seen in Sample 178-1101A-3H-4, 110 cm (79.5 mbsf), defining the upper boundary of the *A. ingens* Zone. The LO of *Fragilariopsis barronii* is well defined in Sample 178-1101A-7H-1, 75 cm (48.6 mbsf). The next older zone is the *Thalassiosira kolbei* Zone. The species datum that defines the upper boundary of this zone (LO *T. kolbei*) was not observed within this hole. *Thalassiosira torokina,* with an LO datum of approximately the same age, was noted in Sample 178-1101A-14H-4, 44 cm (119.14 mbsf), and was used as a proxy for drawing a tentative upper zonal boundary.

The boundary between the *T. kolbei* and *Thalassiosira vulnifica* Zones is defined by the LO of *T. vulnifica,* which was seen in Sample 178-1101A-18X-CC (160.12 mbsf). The LO of *Thalassiosira insigna,* marking the top of the *T. insigna/T. vulnifica* Zone, was observed in Sample 178-1101A-20X-3, 70 cm (173.4 mbsf). Occurring slightly higher than the published age would place it, the LO of *Fragilariopsis interfrigidaria* was noted in Sample 178-1101A-19X-2, 70 cm (162.3 mbsf). The sample interval 178-1101A-21X-3, 58 cm (182.88 mbsf), through 21X-4, 40 cm (184.2 mbsf), contained two datums: the LO of *Thalassiosira striata* and the FO of *T. vulnifica*. These datums placed the top of the *F. interfrigidaria* Zone in Sample 178-1101A-21X-4, 40 cm (184.2 mbsf). One more datum was observed above the base of the core, the FO of *T. insigna* in Sample 178-1101A-23X-1, 29 cm (198.79 mbsf).

F16. Zonal assignments of Site 1101 for calcareous nannofossils, diatoms, radiolarians, and foraminifers, **p. 41.**

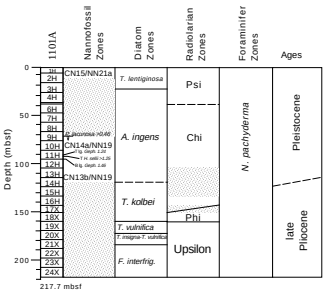

T3. Diatom datums observed at Site 1101, **p. 66.**

Radiolarians

Radiolarian assemblages from core-catcher samples at Site 1101 contained both robust- and thin-shelled specimens. The sharp difference in shell thickness can be used to distinguish reworked and in situ assemblages, improving confidence in the identification of zonal boundaries. Reworked late Pliocene assemblages are present in the Pleistocene part of the section. In general, radiolarians are abundant and moderately preserved, with only two barren intervals (Fig. **F16**).

The youngest zone observed was the Psi Zone, indicated by the presence of *Stylatractus universus* and *Antarctissa cylindrica*. These specimens are lightly silicified and co-occur with robust tests of *Triceraspyris antarctica,* which are considered reworked. The bottom marker of the Psi Zone, *Pterocanium charybdeum trilobum,* is frequently rare and difficult to locate (Hays and Opdyke, 1967; Lazarus, 1990). It was not observed at Site 1101. However, Chen (1975) suggested using the top occurrence of *Saturnalis circularis* as the zonal marker between the Psi and Chi Zones. Although it is found rarely in Antarctic sediments (Lazarus, 1990), this species does occur at Site 1101 and is used to locate the bottom of the Psi Zone at 38 mbsf. The youngest observed occurrence of *Cycladophora pliocenica* coincides with this depth, supporting this conclusion.

The top occurrence of *Eucyrtidium calvertense* at 143 mbsf (Sample 178-1101A-16H-CC) marks the boundary between the Chi and Phi Zones. The base of the Phi Zone is placed at the first observed occurrence of *Helotholus vema* at 160 mbsf (Sample 178-1101A-18X-CC). The top occurrences of *Desmospyris spongiosa* and *Prunopyle titan,* two robust species, are difficult to locate because of reworking at this site and their resistance to breakage. The base of the hole is within the Upsilon Zone.

Calcareous Nannofossils

Calcareous nannofossils were recovered in some cores from Site 1101. Intervals of good preservation were confined to the uppermost two cores and Cores 178-1101A-9H through 14H. Nannofossils were also seen in samples from within the dominantly siliceous intervals but in low numbers and usually partly dissolved. Several samples (178-1101A-9H-4, 87 cm [69.1 mbsf]; 11H-4, 70 cm [90.9 mbsf]; and 12H-3, 63 cm [98.9 mbsf]) contained abundant *Coccolithus pelagicus*.

Three zones were recovered, and three datums were observed. The FO of *Emiliania huxleyi* was noted in Sample 178-1101A-2H-5, 90 cm (15.6 mbsf), defining the base of the CN15/NN21a Zone. From Cores 178-1101A-2H through 9H, only a few, rare specimens were observed, and they provided no age constraints. *Pseudoemiliania lacunosa* appeared in Sample 178-1101A-9H-4, 87 cm (69.1 mbsf), indicating a transition to the CN14b/NN19 Zone. This "event" was not the LO datum of *P. lacunosa* because of the presence of the barren interval confining it above. Within the CN14b/NN19 Zone, two datums and one time marker were noted. The LO of the large *Gephyrocapsa* spp. was seen in Sample 178-1101A-11H-4, 70 cm (90.9 mbsf), and the FO of this same form was observed at the base of Core 178-1101A-11H in the core-catcher sample (95.2 mbsf). Within Core 178-1101A-11H, *Helicosphaera selli* was noted but in such low numbers that the LO cannot be placed. What it does establish is that Core 178-1101A-11H is older than 1.25 Ma. Below Sample 178-1101A-14H-5, 90 cm (121.1 mbsf), calcareous nannofossils are rarely observed, as noted above.

Foraminifers

At Site 1101, core catchers and many additional core samples were examined for foraminifers. Planktonic and both calcareous and agglutinated benthic foraminifers are present. Planktonic foraminifers are abundant to rare in the upper 134 mbsf of Site 1101. Foraminifer-rich sediments are most common from Sample 178-1101A-7H-5, 130–132 cm (55 mbsf), through Sample 178-1101A-16H-1, 80–83 cm (34 mbsf). There is only one carbonate-rich layer above this depth in Sample 178-1101A-1H-CC (8.6 mbsf) (see "Lithostratigraphy," p. 2). In these samples, more than 90% of the assemblage consists of *Neogloboquadrina pachyderma* sinistral, with rare *N. pachyderma* dextral and *Globigerina bulloides,* which is consistent with a Pleistocene to late Pliocene age for this interval (Pujol and Bourrouilh, 1991). Reworked planktonic foraminiferal faunas were not observed at Site 1101.

Benthic foraminifers are common within the foraminifer-rich sediments and rare in other samples from Site 1101. Deep-water species are more common than the reworked shallow-water species observed at Site 1096. Calcareous benthic foraminifers include *Nuttallides umbonifer, Oridorsalis umbonatus, Cibicidoides mundulus, Pyrgo murrhina, Fontbotia wuellerstorfi,* and *Epistominella exigua.* Agglutinated foraminifers, including *Martinottiella antarcticus* and *Karreriella* spp., occur rarely in the biosiliceous intervals.

PALEOMAGNETISM

Split-Core Measurements

Archive halves of APC (to 140 mbsf) and XCB (to 218 mbsf) cores recovered at Site 1101 were measured at 5-cm intervals. Measurement of the natural remanent magnetization (NRM) of all cores was done at the 0- (NRM), 10-, 20-, and 30-mT alternating field (AF) demagnetization steps (Tables T4, T5, T6, T7, T8, all also in ASCII format in the TABLES directory). The distribution of inclination values obtained after demagnetization at 30 mT confirms the very good quality of the magnetic record, as the two lobes of the log-normal distribution are centered at –75° and +78°, in agreement with the value of ±76° expected at this latitude (Fig. F17). The four discrete samples that were progressively demagnetized (0–80 mT) gave linear demagnetization paths, and their inclinations agree well with the split-core inclinations (Tables T9, T10, both also in ASCII format in the TABLES directory).

Magnetostratigraphy

Results obtained from Hole 1101A provide a near-continuous paleomagnetic data set down to 218 mbsf. The magnetostratigraphy has been constructed from records of the inclination and intensity of remanence (Fig. F18; Table T11). Declination was not used in the magnetostratigraphic record, as the cores were not azimuthally oriented. The Brunhes/Matuyama (0.78 Ma) boundary is recorded at ~55 mbsf. The Jaramillo (0.99–1.07 Ma) Subchron is seen between 71.2 and 76 mbsf and the Olduvai (1.77–1.95 Ma) between 121.2 and 127 mbsf. The oldest full polarity zone that is unambiguously recorded in the sediments is Chron C2An.1n (2.581–3.04 Ma), between 166 and 209.4 mbsf. Assuming constant sedimentation rates between geomagnetic polari-

T4. Split-core paleomagnetic measurements for Hole 1101A before demagnetization, p. 67.

T5. Split-core paleomagnetic measurements for Hole 1101A after 10-mT demagnetization, p. 68.

T6. Split-core paleomagnetic measurements for Hole 1101A after 20-mT demagnetization, p. 69.

T7. Split-core paleomagnetic measurements for Hole 1101A after 30-mT demagnetization, p. 70.

T8. Split-core paleomagnetic measurements for Hole 1101A, results from 30-mT demagnetization, p. 71.

F17. Histogram of inclinations at Site 1101 after AF demagnetization at 30 mT, p. 42.

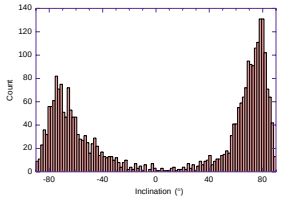

T9. Discrete sample NRM and AF demagnetization results for Hole 1101A, p. 72.

T10. Results from the PCA of discrete paleomagnetic samples, p. 73.

ties, the two short intervals of normal polarity observed at 81.4 and 136.4 mbsf seem to correspond to the Cobb Mountain and Reunion Events, respectively.

From 209.4 mbsf to near the base of the hole, the sediments are reversely magnetized. At the very base of the hole, the inclination is shallow, possibly indicating a polarity transition zone (Fig. F18). If this is the Chron C2An.1r-C2An.2n reversal boundary, the age of the sediments at the bottom of the hole becomes 3.11 Ma. Alternatively, an age of 3.13 Ma is obtained by assuming a constant sedimentation rate from the Chron C2An.1n interval to the base of the hole.

ORGANIC GEOCHEMISTRY

Routine monitoring of hydrocarbon gases was performed on one sample of every core recovered at Site 1101 (Table T12). Inorganic carbon analyses were performed on one sample of every other section, and elemental analyses were performed on a subset of these samples (Table T13). Additional samples were collected specifically to examine suspected carbonate-rich intervals between 50 and 140 mbsf. This constitutes a strong bias in the sampling pattern.

Volatile Hydrocarbons

Methane concentrations remain low (<100 ppm) in the upper 120 mbsf. At greater depths, methane increases to ~20,000 ppm (Table T12; Fig. F19). Small amounts of ethane were detected below 150 mbsf (Table T12).

Inorganic Carbon and Elemental Analysis

The inorganic carbon record at Site 1101 (Fig. F20) distinguishes clearly the lithostratigraphic Units I, II, and III (see "Lithostratigraphy," p. 2). Calcium carbonate concentrations range from 0.3 to 3.1 wt% in Unit I (0–53 mbsf), from 0.2 to 46.7 wt% in Unit II (53–143 mbsf), and from 0.0 to 0.8 wt% in Unit III (143–215 mbsf). Most notably, Unit II includes a series of centimeter- to decimeter-scale layers of carbonate-rich (3–28 wt%) silt and mud that contain well-preserved foraminifers and calcareous nannofossils (see "Biostratigraphy," p. 9). These layers occur exclusively, but not consistently, within bioturbated intervals of inferred interglacial-age sediment, separated by intervals of laminated silt and clay deposited presumably during glacial periods. A similar pattern of carbonate variability characterizes Unit I; however, the peak carbonate concentrations remain low (<4 wt%) compared to those observed in Unit II.

The Brunhes/Matuyama boundary, identified at 55.1 mbsf using paleomagnetic data (see "Paleomagnetism," p. 11) and coeval with oxygen isotope Stage 19, coincides with a carbonate-rich layer near the top of Unit II (Fig. F20). This supports the idea that these layers represent interglacial periods. Other factors that may have influenced the variability of carbonate accumulation include changes in productivity, preservation, sedimentation rate, and dilution by terrigenous sediment. Also, a carbonate-cemented (>45 wt%) silt layer occurs near the base of Unit II (see "Lithostratigraphy," p. 2), where methane concentrations begin to increase and possibly play a role in precipitating calcium carbonate (see "Inorganic Geochemistry," p. 13).

F18. Inclination and intensity of the magnetization for Hole 1101A after AF demagnetization at 30 mT, p. 43.

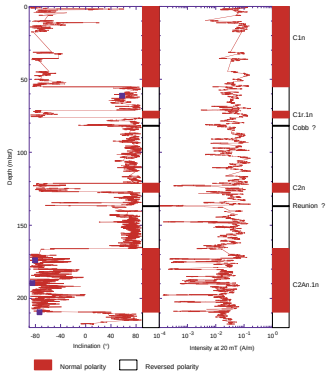

T11. Depths of geomagnetic reversals in Hole 1101A, p. 74.

T12. Headspace gas concentrations for Hole 1101A, p. 75.

T13. Carbonate, inorganic carbon, and total organic carbon analyses for Hole 1101A, p. 76.

F19. Variation in headspace methane concentration with depth, Hole 1101A, p. 44.

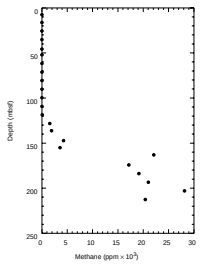

F20. Calcium carbonate content in samples from Site 1101, p. 45.

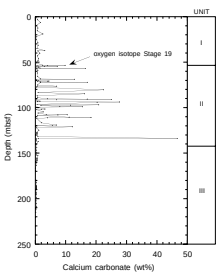

Total organic carbon concentrations (Fig. F21) remain low (<0.4 wt%) throughout Unit I and the upper part of Unit II and decrease essentially to zero in the lower part of Unit II, perhaps as a result of greater terrigenous input. Total organic carbon returns to low (<0.4 wt%) but slightly increasing values with depth in Unit III.

F21. Total organic carbon in samples from Site 1101, p. 46.

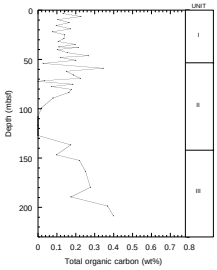

INORGANIC GEOCHEMISTRY

Interstitial Water Chemistry

We squeezed 20 whole-round core samples for interstitial water from Site 1101 (Table T14). Two samples were taken from each of the first six cores in Hole 1101A, except Core 178-1101A-5H, for which recovery was low. One sample was taken from each of the next six cores and from every third core thereafter. Chloride concentrations increase slightly (1.8%) in the upper 50 mbsf and decrease gradually by a similar amount at greater depths (Fig. F22) but show no obvious signs of mixing between waters of different origin; therefore, any stronger trends seen in profiles of other dissolved constituents should reflect chemical reaction processes.

T14. Interstitial water analyses for Hole 1101A, p. 78.

F22. Profiles of interstitial water chemistry from Hole 1101A, p. 47.

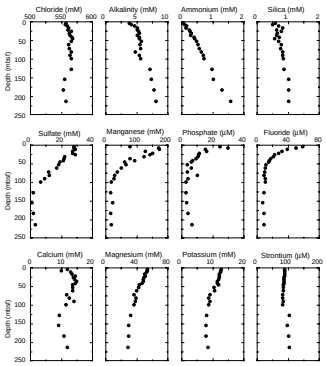

Organic Matter Degradation

The interstitial water chemistry profiles at Site 1101 (Fig. F22) closely resemble those of the upper 250 mbsf at Sites 1095 and 1096. This probably reflects the strong similarity in sedimentation rates (5–10 cm/k.y.) and organic carbon contents (<0.4 wt%) among the three rise sites (see "Sedimentation Rates," p. 19, and "Organic Geochemistry," p. 12; "Sedimentation Rates," p. 32, and "Organic Geochemistry," p. 20, both in the "Site 1095" chapter; and "Sedimentation Rates," p. 30, and "Organic Geochemistry," p. 16, both in the "Site 1096" chapter). At Site 1101, dissolved manganese increases sharply with depth to a maximum concentration (172 µM) at 12 mbsf. This gradient defines the zone of Mn oxide reduction and suboxic diagenesis. Directly below this zone, beginning at 25 mbsf, dissolved sulfate and manganese decrease steadily with depth as a result of sulfate reduction and accompanying precipitation of sulfide minerals. Sulfate decreases to zero and manganese reaches a minimum concentration (15 µM) at 130 mbsf, where measurable concentrations of methane and ethane first arise (see "Organic Geochemistry," p. 12; Fig. F20).

Other indicators of organic matter decay, such as alkalinity, ammonium, and phosphate, all increase with depth in the upper sediment column (Fig. F22). Alkalinity and ammonium both reach maximum values (8.0 mM and 1.6 mM, respectively) at the bottom of the hole and probably continue to increase at greater depths, as seen at Sites 1095 and 1096. Unlike alkalinity and ammonium, dissolved phosphate increases to a maximum (>30 µM) at only 10 mbsf, then decreases sharply between 10 and 50 mbsf and remains relatively constant (2–6 µM) at greater depths. Dissolved fluoride also decreases sharply in the upper 50 mbsf and remains relatively constant (8–10 µM) at greater depths (Fig. F22). We again infer, as at Sites 1095 and 1096, that authigenic apatite begins to precipitate in the sulfate reduction zone and continues with depth until the interstitial water chemistry reaches equilibrium with respect to this mineral phase (Jahnke et al., 1983; Schuffert et al., 1994).

Silica, Carbonate, and Silicate Diagenesis

Other inorganic processes, such as dissolution of biogenic silica and carbonate, reprecipitation of authigenic carbonate phases, and diagenesis of clay and feldspar minerals, probably influence the chemical composition of interstitial water at Site 1101 (Fig. F22). Dissolved silica concentrations remain high (≥0.5 mM) throughout the hole and reach the solubility limit of opal-A (~1.0 mM; Kastner et al., 1977) at 150 mbsf, near the top of lithostratigraphic Unit III (see "Lithostratigraphy," p. 2). We infer that biogenic opal dissolves principally between 0 and 150 mbsf and the interstitial water becomes saturated with respect to silica in Unit III.

Overall, dissolved calcium increases significantly to a maximum value (15 mM) in the upper 50 mbsf, then decreases to a minimum (9 mM) at 130 mbsf, near the base of the sulfate reduction zone. Below this zone, calcium increases again toward a maximum (12 mM) at the bottom of the hole. Magnesium and potassium decrease steadily with depth by a total of 40%–50% of their initial seawater values, whereas strontium concentrations remain essentially unchanged from that of seawater (≈90 µM) through the upper 50 mbsf, then decrease slightly between 50 and 100 mbsf before increasing to a constant, maximum value (100 µM) below the sulfate reduction zone. The increase in dissolved calcium above 50 mbsf could result from either dissolution of carbonate minerals or diagenetic reactions among clay and silicate minerals, and the decrease in calcium at the base of the sulfate reduction zone probably reflects carbonate precipitation. Narrow intervals of carbonate-rich and carbonate-cemented sediment occur in this depth range, but not above (see "Lithostratigraphy," p. 2). The slight increase in calcium and strontium in the lower portions of the hole, below the base of lithostratigraphic Unit II (see "Lithostratigraphy," p. 2), could result from increased dissolution of carbonate or, more likely, from further diagenetic reactions among clay and silicate minerals. Uptake of magnesium and potassium also probably results from clay mineral diagenesis (cf. Gieskes and Lawrence, 1976; Perry et al., 1976).

X-Ray Diffraction Mineralogy

Sixteen samples from Site 1101 were analyzed by X-ray diffraction for bulk and clay mineralogy. Twelve of these samples were taken from Core 178-1101A-10H, spanning a 415-cm interval from 77.84 to 81.99 mbsf. This interval contains one of the 19 carbonate-bearing sediment layers in Unit II (see "Lithostratigraphy," p. 2). Because of the high carbonate content of some of these 12 samples, all were treated with a buffered acetic acid–sodium acetate solution (see "Inorganic Geochemistry," p. 17, in the "Explanatory Notes" chapter). The other four samples were from Cores 178-1101A-17X and 24X in lithostratigraphic Unit III. In each of these cores, a pair of samples was taken to represent alternating sedimentary facies, one of which contained high concentrations of ice-rafted debris (Samples 178-1101A-17X-4, 60–62 cm, and 20X-6, 138–140 cm). All 16 samples were also analyzed for inorganic carbon (see "Organic Geochemistry," p. 16, in the "Explanatory Notes" chapter).

Bulk and clay mineralogy of sediments at Site 1101 was similar to that found at Sites 1095 and 1096, except that calcite was also identified in several samples. Site 1101 sediments consist primarily of quartz,

feldspar, calcite, and a mixture of clay minerals, including chlorite, illite, and a mixed-layer clay, most likely mixed smectite-illite of varying proportions. Traces of amphibole were also detected in most samples, but at considerably lower abundances than those observed in most samples from Sites 1095 and 1096.

Subtle, but possibly significant, trends in bulk mineralogy occur across the carbonate-bearing layer in Core 178-1101A-10H. Calcite peak intensities show a broad maximum from 80 to 81 mbsf (Table T2), consistent with peak carbonate concentrations of 23% measured in this interval. Samples in this interval also have the highest abundances of chlorite and plagioclase relative to quartz, and distinct trends in clay mineralogy (Table T15) occur across this layer. Chlorite abundances, as illustrated by ratios of chlorite/illite and chlorite/mixed-layer clay peak intensities (Fig. F23), are lower by about a factor of two within the carbonate-bearing interval. Sediment within this interval also has the highest chlorite/quartz ratios and thus a relatively high abundance of all clay minerals, relative to other detrital phases.

The greatest variability among clay mineral assemblages in sediment samples from the rise sites (1095, 1096, and 1101) occurs between alternating sedimentary facies, rather than as a function of age or burial depth. For example, in the aforementioned carbonate-rich interglacial interval of Core 178-1101A-10H (Fig. F23) and other rise sediments of inferred interglacial origin, a clear trend exists toward lower chlorite and higher illite and mixed-layer clay abundances, as illustrated in a ternary plot of the relative abundances of these three clays among all samples analyzed (Fig. F24). Rise sediments from glacial intervals cluster strongly near the chlorite end of this diagram and most closely resemble the tills and glacial marine deposits from Site 1097, on the shelf.

Clearly, sediments from the local shelf area represent the probable source of clays deposited on the rise during glacial intervals. Clays deposited during interglacials must have a more complex origin that reflects either a different source area or some sort of physical or chemical sorting during transport. We suggest that depositional mechanisms similar to those described for Quaternary deposition on the slope in the eastern Weddell Sea (Grobe and Makensen, 1992) may play an important role here. During glacial intervals, lower sea level causes ice shelves to remain grounded almost to the continental shelf edge and enables them to deliver sediment more directly to the slope; from there, it can more easily reach the rise as turbidites or contourites. During interglacials, higher sea level moves the grounding line well shoreward of the shelf break, ice sheets deposit much of their sediment load on the shelf, and ice rafting plays an increased role in sedimentation on the continental rise.

T15. Relative intensities of X-ray diffraction peaks from clay mineral samples, p. 79.

F23. Ratios between X-ray diffraction intensities of selected peaks for chlorite, illite, and mixed-layer clays, p. 48.

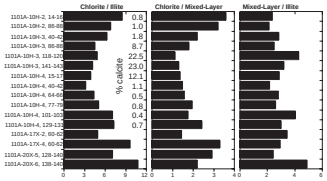

F24. Relative abundances of chlorite, illite, and mixed-layer clays in sediments from the continental shelf and rise sites, p. 49.

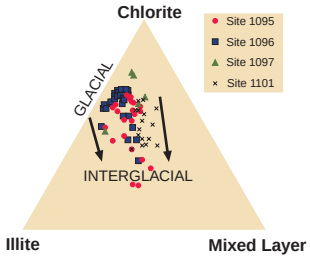

PHYSICAL PROPERTIES

Whole-Core Measurements

Multisensor Track (MST)

Natural gamma-ray activity (NGR), magnetic susceptibility, gamma-ray attenuation porosity evaluator (GRAPE) density, and *P*-wave velocity were measured on whole-round samples (see "Physical Properties," p. 20, in the "Explanatory Notes" chapter). All measurements were

made to the base of the XCB cores in Hole 1101A, to a depth of 217.7 mbsf (Core 178-1101A-24X).

Magnetic Susceptibility

Whole-core magnetic susceptibility was measured at 2-cm intervals (averaged over 2 s). The raw data are provided **on CD-ROM and the World Wide Web** and are shown in Figure **F25**. The spurious data associated with the ends of sections (see **"Physical Properties,"** p. 24, in the "Site 1095" chapter) were minimized at Site 1101 by not measuring the upper and lower 6 cm of each section. After low-pass filtering (Fig. **F26**), depth-scaled susceptibility shows a positive correlation with the GRAPE density data (see **"GRAPE Bulk Density,"** p. 16). Paleomagnetic events were used to convert the data to the age scale shown in Figure **F27** (filtered after conversion to age scale).

The susceptibility of the sediments increases from ~250 × 10^{-5} to ~700 × 10^{-5} SI between 0 and ~67 mbsf (~0.93 Ma). Superimposed on this trend is a quasiperiodic variation in the amplitude of susceptibility with a wavelength of ~12 m. Susceptibility then remains at ~470 × 10^{-5} SI, although with a higher amplitude quasicyclic variability with a wavelength of ~2.5 m. This character extends down to ~122 mbsf (~1.80 Ma), where the susceptibility drops again, with less consistent variability, to ~300 × 10^{-5} SI. The above changes match variations in the sedimentology at the site and the broad lithostratigraphic division into three units (see **"Lithostratigraphy,"** p. 2). In particular, the susceptibility lows throughout the sequence match higher levels of biogenic material in the sediments. A strong visible match between peaks in magnetic susceptibility and GRAPE density (see **"GRAPE Bulk Density,"** p. 16) is apparent, although there is no significant statistical correlation between the data sets (correlation coefficient of 0.56 using the program of Paillard et al., 1996).

GRAPE Bulk Density

Density was measured by gamma-ray attenuation (referred to as GRAPE density) at 2-cm intervals (averaged over 2 s at each point). The raw data are provided **on CD-ROM and the World Wide Web** and are shown before (Fig. **F25**) and after (Figs. **F26, F27**) low-pass filtering.

GRAPE density increases from 1.5 g/cm³ to ~1.85 g/cm³ at 67 mbsf and shows some of the amplitude alternation of ~12-m wavelength seen within the susceptibility record to this depth. The density then varies at 1.85 g/cm³ until 140 mbsf. There is no change in variability of the signal across 67 mbsf, in contrast with the susceptibility signal, in which the amplitude of variation increases below 67 mbsf. Below 140 mbsf, the density varies around a value of 1.65 g/cm³.

The 15 troughs in the GRAPE density signal within lithostratigraphic Unit II (Fig. **F26**) all correlate with biogenic horizons in the sediments (see **"Lithostratigraphy,"** p. 2). Lithostratigraphic Unit I also contains 15 troughs in which the amplitude of variation exceeds 0.05 g/cm³ after the data have been filtered. However, smaller variations are also present, and the troughs are more difficult to determine than in Unit II (Fig. **F26**).

F25. Raw data for NGR, GRAPE density, magnetic susceptibility, and *P*-wave velocity, **p. 50.**

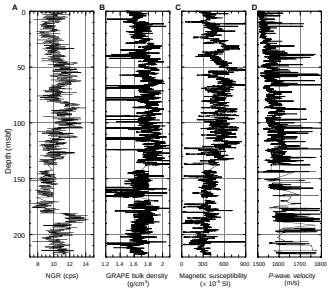

F26. NGR, GRAPE density, magnetic susceptibility, and *P*-wave velocity vs. depth, **p. 51.**

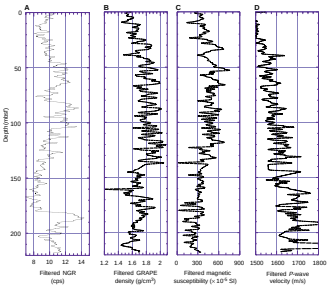

F27. NGR, GRAPE density, magnetic susceptibility, and *P*-wave velocity vs. age, **p. 52.**

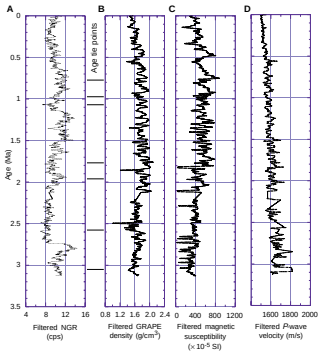

P-wave Velocities

Whole-core *P*-wave measurements were made at 2-cm intervals (averaged over 2 s at each point). The raw data are provided **on CD-ROM and the World Wide Web** and are shown before (Fig. **F25**) and after (Figs. **F26, F27**) low-pass filtering. The data quality is reasonably good to down to 136 mbsf. Below 136 mbsf, biscuiting caused by XCB coring led to data gaps.

P-wave variation is high compared with that at Sites 1095 and 1096, and, for the record down to 136 mbsf, peaks in the data match peaks in the GRAPE density and magnetic susceptibility, although there is no significant correlation between the data sets (correlation coefficient of 0.61 with GRAPE density using the program of Paillard et al., 1996).

Natural Gamma Radiation

Whole-core natural gamma-ray emissions (averaged over 15 s) were counted at 15-cm intervals. The raw data are provided **on CD-ROM and the World Wide Web** and are shown before (Fig. **F25**) and after (Figs. **F26, F27**) low-pass filtering.

The NGR signal drops from 11 cps at 0 mbsf to ~9 cps at 10 mbsf before rising again to 13.5 cps at 85 mbsf, falling to 8 cps at 170 mbsf, and rising again to 11 cps in the deepest core. This broad trend is interrupted between 63 and 85 mbsf by a drop to 8.5 cps, and between 130 and 200 mbsf by a rise to 14.5 cps.

The broad low-high-low profile of the NGR signal matches similar trends in the magnetic susceptibility and GRAPE density, which suggests that this trend reflects a variation in the content or origin of the nonbiogenic material in the sediments, rather than in any particular size fraction (which might show as a difference between NGR and the other records). Given that grain density (below) does not change in the upper 50 m of the hole, the initial rise in the MST measurements may reflect consolidation in the upper sediment column. There is no consistent relationship between smaller scale NGR variations and the other signals.

Split-Core Measurements

Index Properties

Gravimetric and volumetric determinations of index properties were made for 67 samples from Hole 1101A. One sample was taken every first, third, and fifth section of each core, where possible. Samples were not taken from reconstituted sediment surrounding biscuits or in regions of remolded core. Wet mass, dry mass, and dry volume were measured, and from these measurements, percentage water weight, porosity, dry density, bulk density, and grain density were calculated (see **"Physical Properties,"** p. 20, in the "Explanatory Notes" chapter; data are also provided **on CD-ROM and the World Wide Web**).

Bulk density follows GRAPE density closely (Fig. **F28A**). Porosity initially decreases downhole (Fig. **F28C**), as might be expected under consolidation, but rises again below 140 mbsf. Grain density (Fig. **F28B**) is constant downhole to ~140 mbsf, where it begins to decrease, which suggests a lithologic change that is probably also responsible for the increased porosity. There is a weak positive correlation between total biogenic content and porosity (Fig. **F29**), which was seen previously at

F28. Filtered GRAPE and bulk density, grain density, and porosity vs. depth, **p. 53.**

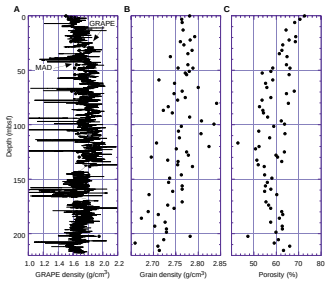

F29. Total biogenic content and porosity vs. depth, **p. 54.**

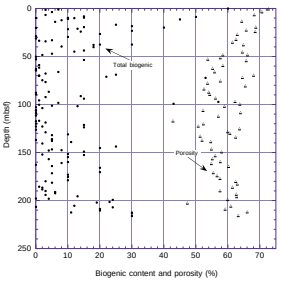

Sites 1096, 1098, and 1099 (see "Physical Properties," p. 21, in the "Site 1096" chapter, and "Physical Properties," p. 17, in the "Palmer Deep [Sites 1098 and 1099]" chapter for further explanation).

Discrete *P*-wave Velocities

Discrete *P*-wave velocity measurements using all three sensors (PWS1, PWS2, and PWS3) of the velocity-strength system were made on cores from Site 1101. The upper 50 m of Hole 1101A (Cores 178-1101A-1H through 6H) were soft enough to use the orthogonal penetrative transducer pairs of PWS1 and PWS2. Additionally, Hamilton Frame measurements (PWS3) were performed at the center of the cross formed by the PWS1 and PWS2 transducer imprints to compare results from all three transducers. Results of all three measurements (PWS1, PWS2, and PWS3) for the upper 50 mbsf are shown in Figure F30. The average spatial resolution of the measurements is ~1 m. The measurements made using transducer pairs PWS1 and PWS2 show very good agreement. No obvious velocity anisotropy is evident in the upper 50 m. The Hamilton Frame measurements (PWS3) taken subsequently at the same locations show higher velocities with a constant offset of ~40 m/s, which we cannot explain.

The velocity at Site 1101 increases linearly with depth (Fig. F31). Local excursions to much higher velocities occur when measurements are taken on small sand and silt layers (at 50.5, 81.0, 93.8, and 206.5 mbsf) or diamictite layers (at 202.3 mbsf). These layers also show the highest signal attenuation. The raw data are provided on CD-ROM and the World Wide Web.

Thermal Conductivity

Thermal conductivity was measured once per core, on average, down to ~137 mbsf at Site 1101, usually in the middle of Section 3. Thermal conductivity was used in combination with downhole temperature measurements to estimate heat flow and hence the temperature at the bottom of the hole and the depth to the base of a theoretical methane hydrate stability zone and associated bottom-simulating reflector (BSR), for comparison with Site 1096. Since Site 1101 was drilled only to 217.7 mbsf, such comparison is limited.

All measurements were made by needle probe on the unsplit core, assuming that the core was undisturbed before insertion of the needle and would remain so afterward. For APC cores (i.e., down to 142 mbsf), this assumption is probably correct. No measurements were made in XCB cores (see "Physical Properties," p. 21, in the "Site 1096" chapter). Thermal conductivity values are low above 22 mbsf and uniformly higher below 31 mbsf. The low values are lower than were measured in the uppermost section at Site 1096. This change does not reflect a lithologic change but may be related to porosity. In the absence of a certain explanation, and because values are mutually consistent, all are accepted as valid. A simple straight-line fit to the data below 31 mbsf (Fig. F32) provides an average thermal conductivity of 1.05 W/(m·K).

Downhole Temperature Measurements and Geothermal Heat Flow

The first Adara temperature tool deployment at Site 1101, intended to determine mudline temperature, failed because the APC triggered

F30. Raw PWS1, PWS2, and PWS3 data plotted vs. depth, p. 55.

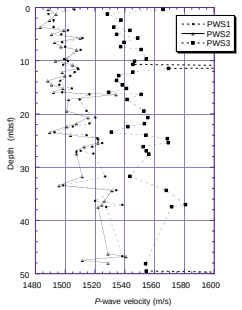

F31. Raw PWS3 data plotted vs. depth, Hole 1101A, p. 56.

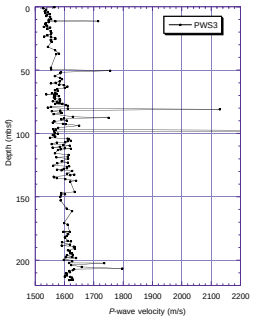

F32. Thermal conductivity measurements at Site 1101, p. 57.

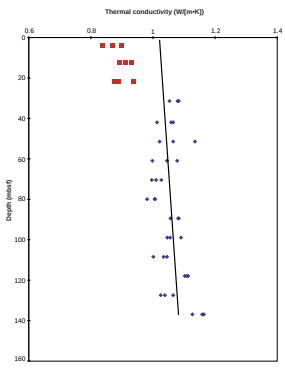

early. Mudline temperature was measured before firing Core 178-1101A-2H. Additional Adara temperature measurements were made within the sediments after firing Cores 178-1101A-4H, 7H, 10H, and 13H. Temperatures are plotted vs. depth in Figure **F33**. A straight-line fit to all points except the seafloor measurement (to avoid the effect of the shallow, low-conductivity layer) provides a geothermal gradient of 89.4 °C/km. With the thermal conductivity calculated above, this gives an average heat flow determination of 93.9 mW/m², and the lower conductivity at shallow depth brings the temperature-depth curve into good agreement with the measured seafloor temperature. The corresponding depth to a methane hydrate BSR, calculated using Pollution Prevention and Safety Panel (PPSP) (1992) criteria (see **"Physical Properties,"** p. 21, in the "Site 1096" chapter), is 270 mbsf, well below the base of the hole.

Oceanic basement age at this site, determined from oceanic magnetic anomalies (Larter and Barker, 1991a), is 20.6 Ma, using the time scale of Cande and Kent (1995), although the site is very close to the Biscoe fracture zone, with ocean floor ~2 m.y. older on the other side (see Fig. **F4,** p. 32, in Barker and Camerlenghi, Chap. 2, this volume). Allowing for time scale changes from the original work of Parsons and Sclater (1977), the theoretical heat flow for ocean floor of age 20.6 Ma is ~101 mW/m², ~7% higher than observed. No allowance has been made at this site for the thermal blanketing effect of rapid sedimentation (e.g., Hutchison, 1985).

SEDIMENTATION RATES

A sedimentary section, 218 m thick, extending from the Holocene to the upper Pliocene (~3.1 Ma), was recovered at Site 1101. Sedimentation rates were determined using magnetostratigraphy, diatom datums, and calcareous nannofossil datums. Sedimentation rates are assumed to be constant between datums and are calculated by taking the slope of the depth-age curve (Fig. **F34**) between successive points.

The depth of a geomagnetic polarity transition is defined as the depth at which the inclination changes sign. Geomagnetic reversals at this site are very well defined and occur over relatively thin intervals (see Table **T11**). For consistency with other Leg 178 sites, the center of the uncertainty interval was used in calculating sedimentation rates. Biostratigraphic datums were assigned when a clear FO or LO could be determined through examination of sediment samples. No FO or LO was resolved when the occurrence bordered an interval barren of biogenic material.

Sedimentation rates determined from magnetostratigraphy and diatom and calcareous nannofossil datums are given in Tables **T16, T17,** and **T18** and illustrated in Figure **F35**. For the upper 70 m of the hole, the average sedimentation rate is 6.9 cm/k.y. There is excellent agreement between sedimentation rates derived from all data sets; rates from paleomagnetic data and diatom and calcareous nannofossil datums average 6.8, 7.1, and 6.8 cm/k.y., respectively.

Both the paleomagnetic and the biostratigraphic data show a low in the sedimentation rate at ~ 120 mbsf. At this depth, the sedimentation rate drops downhole from an average of 6.9 cm/k.y. to an average of 4.1 cm/k.y. The decrease is especially pronounced in the paleomagnetic data and is manifested as a very thin Olduvai Event (C2n) between 121 and 127 mbsf (see **"Paleomagnetism,"** p. 11). The lithology of this

F33. Downhole temperature measurements at Site 1101, **p. 58.**

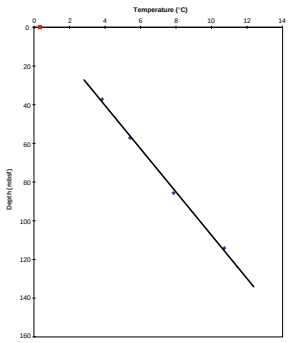

F34. Depth-age profile determined from geomagnetic reversals and diatom and calcareous nannofossil datums, **p. 59.**

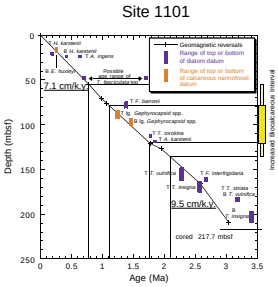

T16. Sedimentation rates calculated from geomagnetic polarity transition data, **p. 80.**

T17. Sedimentation rates calculated from diatom datums, **p. 81.**

T18. Sedimentation rates calculated from calcareous nannofossil datums, **p. 82.**

F35. Sedimentation rate vs. depth and age, **p. 60.**

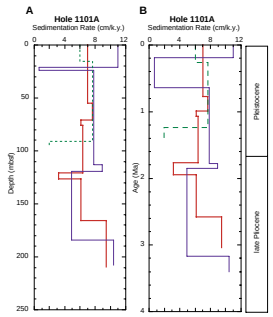

interval is a sequence of massive clayey silts and laminated clayey silts. This sequence occurs within lithostratigraphic Unit II (see "Lithostratigraphy," p. 2), which is characterized by foraminifer-bearing clayey silt. The interval from 122 to 133 mbsf does not contain foraminifer layers, and the percent biogenic sediment is very low, although there is no evidence of erosion. No clear unconformities or erosion surfaces occur within this interval. This interval is acoustically semitransparent and is characterized by parallel and subparallel, continuous and disrupted reflectors (see "Seismic Stratigraphy," p. 20). The onset of the Olduvai Event occurs in Core 178-1101A-15H, and the termination occurs in Core 14H. It is possible that some material was not recovered between Cores 178-1101A-14H and 15H, but it is unlikely that this alone would cause an apparent drop in the sedimentation rate by a factor of 1.7. The available data suggest that this interval is characterized by genuinely low deposition rates.

From 130 to 165 mbsf, polarity transitions and diatom datums give an average sedimentation rate of 5.6 cm/k.y., slightly lower than the rate at the top of the hole. Near the base of the hole, both data sets show a high in the sedimentation rate, but it spans 18 m (0.59 m.y.) more in the paleomagnetic data. The downhole increase in average sedimentation rate (5.6 to 10.0 cm/k.y.) occurs within lithostratigraphic Unit III (see "Lithostratigraphy," p. 2). This unit is a massive clayey silt with extremely low biogenic content, no bioturbation, and thin diamict layers. The lithologic observations are consistent with a period of rapid deposition.

SEISMIC STRATIGRAPHY

Site 1101 is located on the proximal part of sediment Drift 4 on the Antarctic Peninsula continental rise. The drift has an asymmetric profile in directions parallel and perpendicular to the margin, similar to Drift 7, which was drilled at Sites 1095 and 1096 (see "Background and Scientific Objectives," p. 1). Site 1101 lies on the gentler side of the drift, ~5.5 km northwest of the drift crest (Fig. F36). Previous seismic stratigraphic interpretations of this sedimentary body can be found in Rebesco et al. (1996, 1997).

Only one MCS profile, collected by the Osservatorio Geofisico Sperimentale of Trieste (Line IT92AW-114; Fig. F36; "Appendix," p. 24, and Fig. AF1, p. 59, both in the "Leg 178 Summary" chapter), crosses Site 1101. Regional cover does exist, however, and was made available during Leg 178 (Fig. F1; "Seismic Stratigraphy," p. 29, in the "Explanatory Notes" chapter). This data set has been used to establish the seismic stratigraphy described below. Individual laboratory (Hamilton Frame) measurements of *P*-wave velocity on cores recovered at Site 1101 (Fig. F31) have been used to estimate velocities and thus to assign depths to reflectors (Fig. F37).

Seismic Units

Drilling at Site 1101 reached a depth of 217.7 mbsf. We identify three seismic units (Fig. F36; Table T19).

F36. Uninterpreted and interpreted MCS profile IT92AW-114 across Drift 4, p. 61.

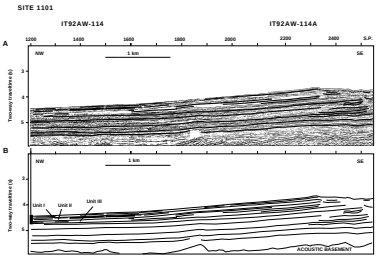

F37. Time-depth model for Site 1101, p. 62.

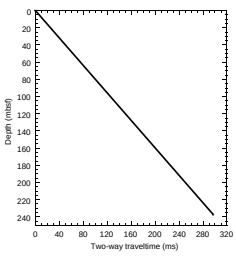

T19. TWT and depth to base of seismic units, Site 1101, p. 83.

Seismic Unit I

Seismic Unit I (0–79 mbsf) consists of parallel and subparallel high-amplitude and continuous reflectors that alternate with lower amplitude disrupted reflectors (Fig. F38). The sub-bottom 3.5-kHz profile, obtained by the *JOIDES Resolution* on approach to the site, penetrated approximately the upper 50 m of seismic Unit I (see Fig. F3). This profile shows higher and lower amplitude reflector packages in a cyclic pattern. The base of Unit I at Site 1101 is marked by a high-amplitude reflector that, southwestward, has lateral variations in amplitude and continuity. Although the overall external geometry of seismic Unit I at Site 1101 is of a sheet drape, it is 25-30 m thicker at the crest of the drift than at Site 1101 (Fig. F36).

F38. Seismic section over Site 1101, p. 63.

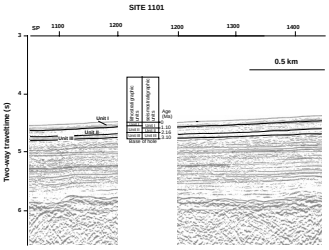

Seismic Unit II

Seismic Unit II (79–141 mbsf) is characterized by low-amplitude reflectors and is acoustically semitransparent (Fig. F38). Toward the crest of the drift, 0.4 km southwest of Site 1101, this unit is marked by parallel and subparallel continuous and disrupted reflectors with lateral variation in amplitude (Fig. F36). The base of Unit II at Site 1101 corresponds to a low-amplitude disrupted reflector that grades southwestward to a high-amplitude reflector that can be traced to the crest of the drift. Seismic Unit II is characterized by a sheet drape external geometry (Fig. F36).

Seismic Unit III

Seismic Unit III (143–216 mbsf) extends to the base of the hole and is bounded there by a high-amplitude reflector. Internally, seismic Unit III is semitransparent with only one low-amplitude discontinuous reflector apparent in the MCS profile (Fig. F38). The thickness of seismic Unit III increases from 76 m at Site 1101 to ~200 m at the crest of the drift. The external regional geometry of Unit III is that of a wedge. Internally, the wedge is semitransparent with some higher amplitude reflectors that thin or pinch out or downlap the base of the unit in a seaward direction before reaching the location of Site 1101 (Fig. F36).

Interpretation

Drilling of Site 1101 placed some constraints on the nature and age of the seismic units defined above (Fig. F38). Several general observations can be made from the seismic profile across the drift site.

The overall sheet drape geometry of seismic Units I and II compares well with lithostratigraphic Units I (0–53.3 mbsf) and II (53.3–142.7 mbsf) (see "Lithostratigraphy," p. 2). Lithostratigraphic Unit I is a well-defined alternation of massive biogenic-rich and laminated terrigenous sediments. The cyclic pattern can be recognized in the sub-bottom 3.5-kHz profile (Fig. F3). Lithostratigraphic Unit II is a repetitive succession of laminated and foraminifer-bearing massive facies. Sediments from lithostratigraphic Units I and II are dominantly hemipelagic, deposited under a regime of low-density turbidity current flow and weak bottom currents (see "Lithostratigraphy," p. 2).

The transition from seismic Unit II to Unit III corresponds to a marked change in lithologic character. Lithostratigraphic Unit III (142–216 mbsf) contains a 50-m-thick, massive clayey silt with low biogenic

content and beds of diamict (see "Lithostratigraphy," p. 2). This unit has been interpreted to have formed by meltwater plumes and sediment gravity flows or turbidity currents during times of ice-sheet expansion (see "Lithostratigraphy," p. 2). The greater regional thickness of Unit III away from the site, compared to seismic Units I and II, suggests greater sedimentation rates during its deposition. The change in external geometry from a well-developed wedge in seismic Unit III to sheet drape in seismic Units I and II may represent a shift from a higher to a lower energy sedimentation environment.

The ages assigned to the seismic units recognized at Site 1101 (Fig. F38) are based on preliminary paleomagnetic data from drilled cores (see "Paleomagnetism," p. 11). Seismic Unit I is Holocene to late Pleistocene in age (0–1.1 Ma), seismic Unit II is late Pleistocene to late Pliocene (1.1–2.16 Ma), and seismic Unit III is late Pliocene (2.16–3.1 Ma).

REFERENCES

Bart, P.J., and Anderson, J.B., 1995. Seismic record of glacial events affecting the Pacific margin of the northwestern Antarctic Peninsula. *In* Cooper, A.K., Barker, P.F., and Brancolini, G. (Eds.), *Geology and Seismic Stratigraphy of the Antarctic Margin.* Antarct. Res. Ser., 68:75–96.

Berggren, W.A., Kent, D.V., Swisher, C.C., III, and Aubry, M.-P., 1995. A revised Cenozoic geochronology and chronostratigraphy. *In* Berggren, W.A., Kent, D.V., Aubry, M.-P., and Hardenbol, J. (Eds.), *Geochronology, Time Scales and Global Stratigraphic Correlation*. Spec. Publ.—Soc. Econ. Paleontol. Mineral. (Soc. Sediment. Geol.), 54:129–212.

Cande, S.C., and Kent, D.V., 1995. Revised calibration of the geomagnetic polarity timescale for the Late Cretaceous and Cenozoic. *J. Geophys. Res.,* 100:6093–6095.

Chen, P.-H., 1975. Antarctic radiolaria. *In* Hayes, D.E., Frakes, L.A., et al., *Init. Repts. DSDP,* 28: Washington (U.S. Govt. Printing Office), 437–513.

Ehrmann, W.U. and Grobe, H., 1991. Cyclic sedimentation at Sites 745 and 746, Leg 119. *In* Barron, J., Larsen, B., et al., *Proc. ODP, Sci. Results,* 119: College Station, TX (Ocean Drilling Program), 225–238.

Gersonde, R., and Bárcena, M.A., 1998. Revision of the late Pliocene–Pleistocene diatom biostratigraphy for the northern belt of the Southern Ocean. *Micropaleontology*, 44:84–98.

Gersonde, R., Hodell, D.A., Blum, P., et al., 1999. *Proc. ODP, Init. Repts.,* 177 [CD-ROM]. Available from: Ocean Drilling Program, Texas A&M University, College Station, TX 77845-9547, U.S.A.

Gersonde, R., Kyte, F.T., Bleil, U., Diekmann, B., Flores, J.A., Gohl, K., Grahl, G., Hagen, R., Kuhn, G., Sierro, F.J., Voelker, D., Abelmann, A., and Bostwick, J.A., 1997. Geological record and reconstruction of the late Pliocene impact of the Eltanin asteroid in the Southern Ocean. *Nature*, 390:357–363.

Gieskes, J.M., and Lawrence, J.R., 1976. Interstitial water studies, Leg 35. *In* Hollister, C.D., Craddock, C., et al., *Init. Repts. DSDP,* 35: Washington (U.S. Govt. Printing Office), 407–426.

Grobe, H., and Mackensen, A., 1992. Late Quaternary climatic cycles as recorded in sediments from the Antarctic continental margin. *In* Kennett, J.P., and Warnke, D.A. (Eds.), *The Antarctic Paleoenvironment: A Perspective on Global Change* (Pt. 1). Antarct. Res. Ser., 56:349–376.

Harwood, D.M., and Maruyama, T., 1992. Middle Eocene to Pleistocene diatom biostratigraphy of Southern Ocean sediments from the Kerguelen Plateau, Leg 120. *In* Wise, S.W., Jr., Schlich, R., et al., *Proc. ODP, Sci. Results,* 120: College Station, TX (Ocean Drilling Program), 683–733.

Hays, J.D., and Opdyke, N.D., 1967. Antarctic radiolaria, magnetic reversals, and climate change. *Science,* 158:1001–1011.

Hesse, R., Khodabakhsh, S., Klaucke, I., and Ryan, W.B.F., 1997. Asymmetrical turbid surface plume deposition near ice-outlets of the Pleistocene Laurentide Ice Sheet in the Labrador Sea. *Geo-Mar. Lett.* 17:179–187.

Hutchison, I., 1985. The effects of sedimentation and compaction on oceanic heat flow. *Geophys. J. R. Astron. Soc.,* 82:439–459.

Jahnke, R.A., Emerson, S.R., Roe, K.K., and Burnett, W.C., 1983. The present day formation of apatite in Mexican continental margin sediments. *Geochim. Cosmochim. Acta,* 47:259–266.

Kastner, M., Keene, J.B., and Gieskes, J.M., 1977. Diagenesis of siliceous oozes, I. Chemical controls on the rate of opal-A to opal-CT transformation—an experimental study. *Geochim. Cosmochim. Acta,* 41:1041–1059.

Larter, R.D., and Barker, P.F., 1991a. Effects of ridge-crest trench interaction on Antarctic-Phoenix spreading: forces on a young subducting plate. *J. Geophys. Res.,* 96:19583–19607.

Larter, R.D., and Barker, P.F., 1991b. Neogene interaction of tectonic and glacial processes at the Pacific margin of the Antarctic Peninsula. *In* Macdonald, D.I.M. (Ed.), *Sedimentation, Tectonics and Eustasy: Sea-level Changes at Active Margins*. Spec. Publ. Int. Assoc. Sedimentol., 12:165–186.

Lazarus, D., 1990. Middle Miocene to Recent radiolarians from the Weddell Sea, Antarctica, ODP Leg 113. *In* Barker, P.F., Kennett, J.P., et al., *Proc. ODP, Sci. Results,* 113: College Station, TX (Ocean Drilling Program), 709–727.

Mackensen, A., Grobe, H., Hubberten, H.-W., Spiess, V., and Fütterer, D.K., 1989. Stable isotope stratigraphy from the Antarctic continental margin during the last one million years. *Mar. Geol.,* 87:315–321.

Paillard, D., Labeyrie, L., and. Yiou, P., 1996. Macintosh program performs time-series analysis. *Eos,* 77:379.

Parsons, B., and Sclater, J.G., 1977. An analysis of the variation of ocean floor bathymetry and heat flow with age. *J. Geophys. Res.,* 82:803–827.

Perry, E.A., Jr., Gieskes, J.M., and Lawrence, J.R., 1976. Mg, Ca and O^{18}/O^{16} exchange in the sediment-pore water system, Hole 149, DSDP. *Geochim. Cosmochim. Acta,* 40:413–423.

PPSP, 1992. Ocean drilling program guidelines for pollution prevention and safety. *JOIDES J.,* 18:1–24.

Pudsey, C.J., and Camerlenghi, A., 1998. Glacial-interglacial deposition on a sediment drift on the Pacific margin of the Antarctic Peninsula. *Antarct. Sci.,* 10:286–308.

Pujol, C., and Bourrouilh, R., 1991. Late Miocene to Holocene planktonic foraminifers from the subantarctic South Atlantic. *In* Ciesielski, P.F., Kristoffersen, Y., et al., *Proc. ODP, Sci. Results,* 114: College Station, TX (Ocean Drilling Program), 217–232.

Rebesco, M., Camerlenghi, A., and Zanolla, C., in press. Bathymetry and morphogenesis of the continental margin west of the Antarctic Peninsula. *Terra Antarct.*

Rebesco, M., Larter, R.D., Barker, P.F., Camerlenghi, A., and Vanneste, L.E., 1997. The history of sedimentation on the continental rise west of the Antarctic Peninsula. *In* Barker, P.F., and Cooper, A.K. (Eds.), *Geology and Seismic Stratigraphy of the Antarctic Margin* (Pt. 2). Antarctic Res. Ser., 71:29–49.

Rebesco, M., Larter, R.D., Camerlenghi, A., and Barker, P.F., 1996. Giant sediment drifts on the continental rise of the Antarctic Peninsula. *Geo-Mar. Lett.,* 16:65–75.

Schuffert, J.D., Jahnke, R.A., Kastner, M., Leather, J., Sturz, A., and Wing, M.R., 1994. Rates of formation of modern phosphorite off western Mexico. *Geochim. Cosmochim. Acta,* 58:5001–5010.

Tomlinson, J.S., Pudsey, C.J., Livermore, R.A., Larter, R.D., and Barker, P.F., 1992. Long-range side scan sonar (GLORIA) survey of the Antarctic Peninsula Pacific Margin. *In* Yoshida, Y., Kaminuma, K., and Shiraishi, K. (Eds.), *Recent Progresses in Antarctic Earth Sciences,* Proceedings, Sixth International Symposium on Antarctic Earth Sciences, Tokyo, 423–429.

Figure F1. A. Location of Site 1101 and the two original sites, APRIS-05A and 06A, proposed on Drift 4 (see Leg 178 scientific prospectus). Bathymetry is from Rebesco et al. (in press). (Continued on next page.)

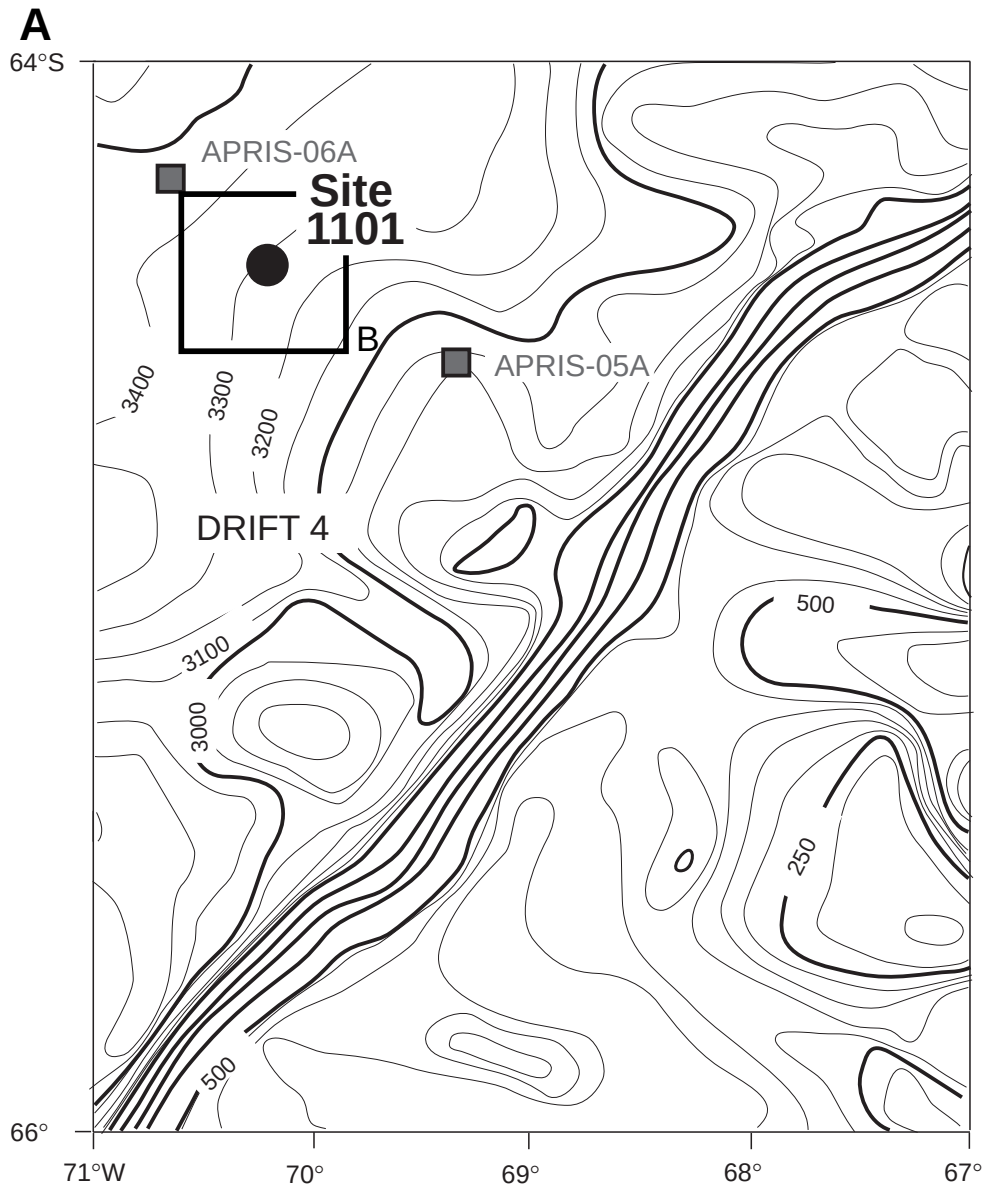

Figure F1 (continued). B. Location of Site 1101 on multichannel seismic (MCS) reflection profile IT92-114 and the 3.5-kHz profile collected during approach and departure from site (bold line).

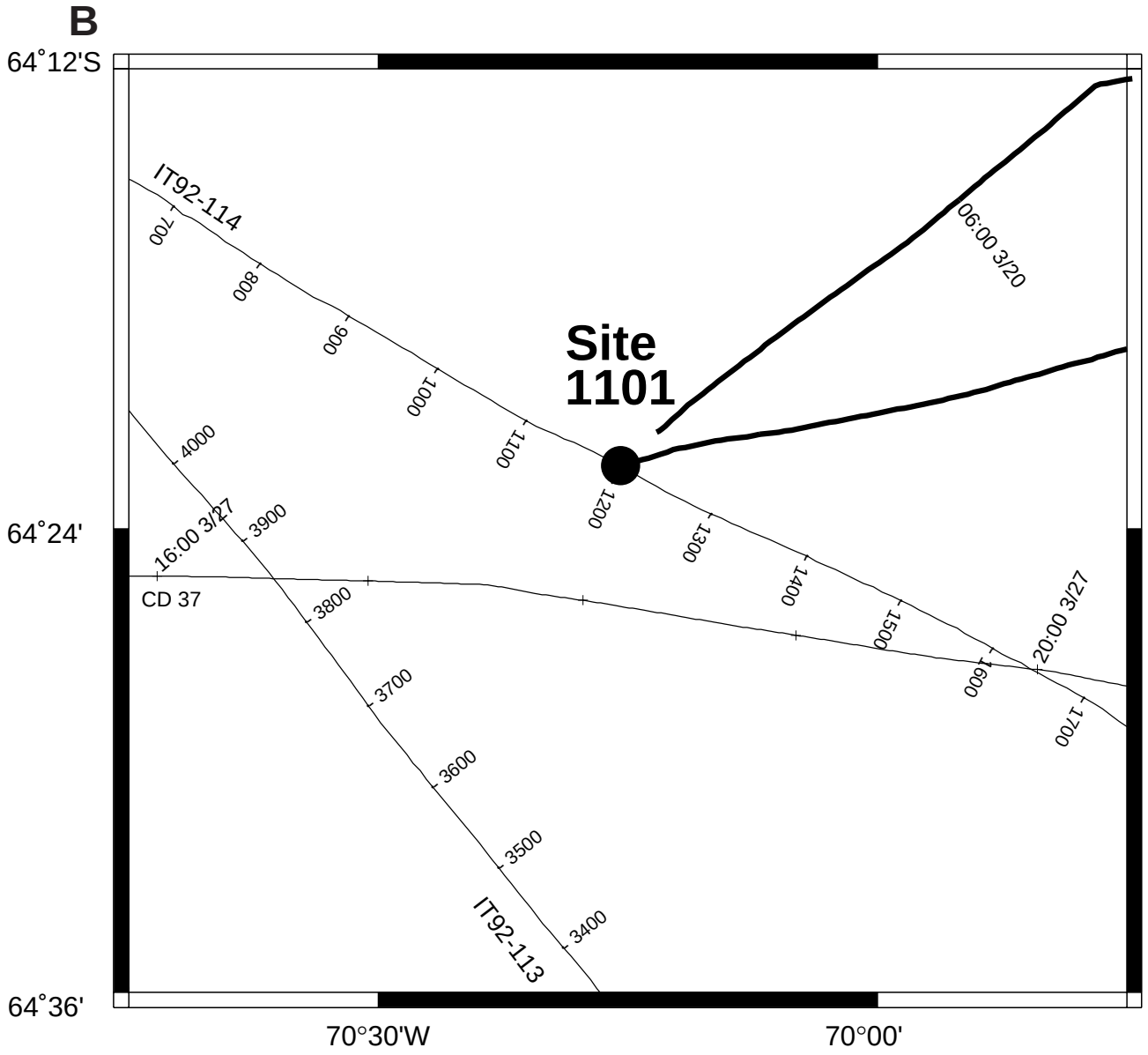

Figure F2. Left: Seismic window at proposed site APRIS-06A (distal site on Drift 4). **Middle:** Part of MCS reflection profile IT92-114 across Site 1101 (see location in Fig. **F1B,** p. 26). **Right:** Seismic window at proposed site APRIS-05A (proximal site on Drift 4).

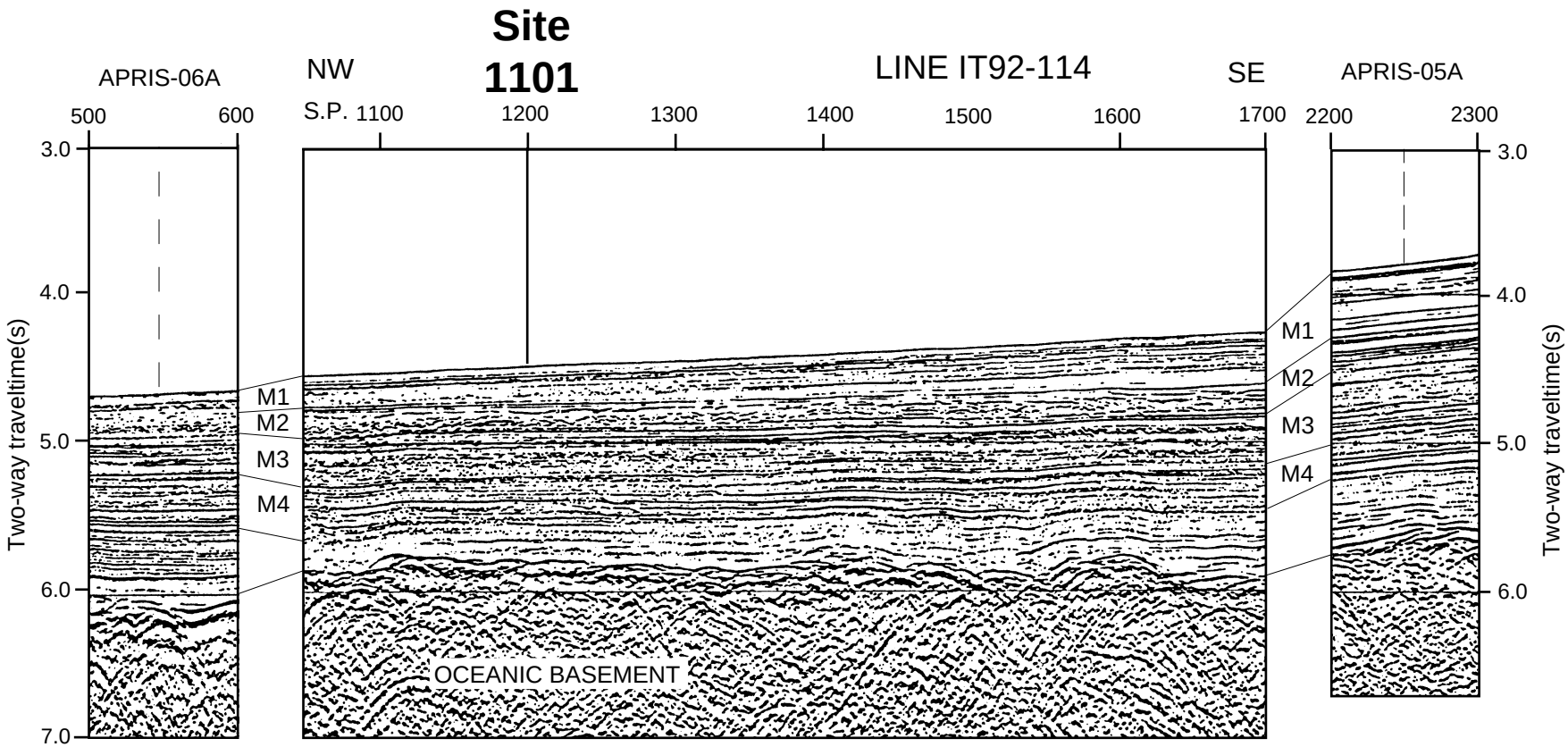

Figure F3. The 3.5-kHz sub-bottom profile across Site 1101, acquired during site approach. The site is located on the gentle northwest flank of Drift 4 (note the high vertical exaggeration of the profile). Bedding in the upper 40 m is parallel to the seafloor.

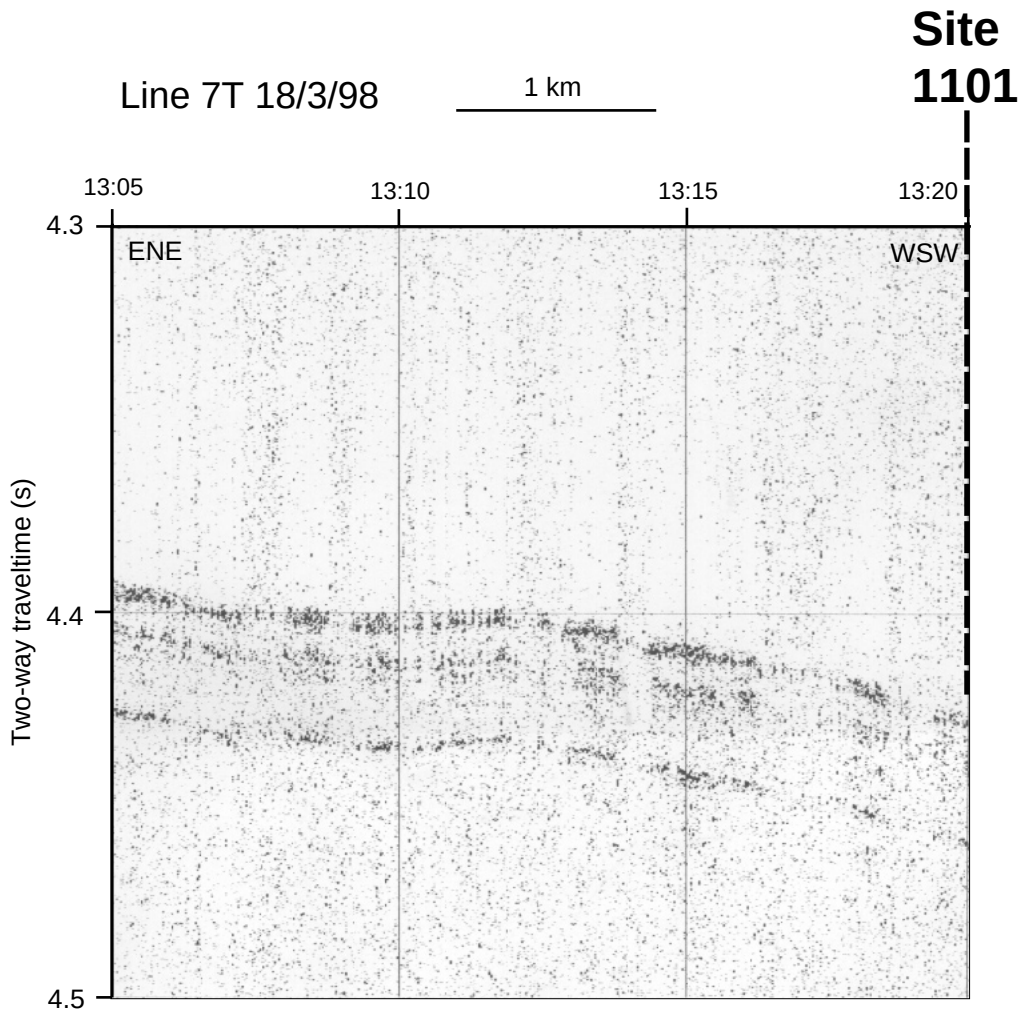

Figure F4. Lithostratigraphic column for Site 1101 including percent biogenic component compiled from smear-slide data and magnetic susceptibility. Unit I consists of alternating packets of massive and laminated clayey silt. Unit II has 19 foraminifer-bearing beds that occur cyclically and coincide with lows in the magnetic susceptibility curve (see Fig. F8, p. 33). Unit III is characterized by low biogenic content in its upper part and relatively low magnetic susceptibility. A sharp peak in magnetic susceptibility coincides with a turbidite near the base of the hole.

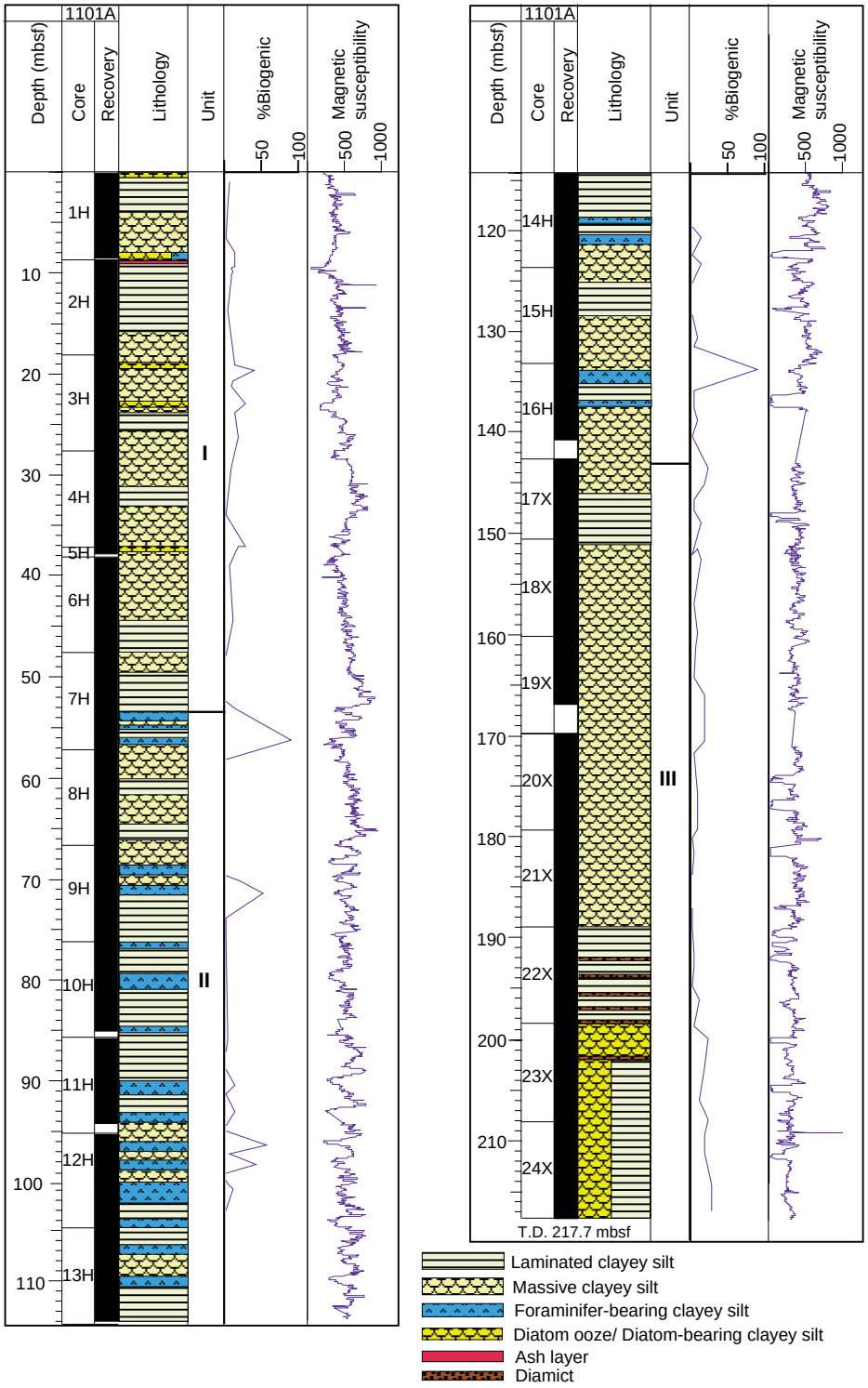

Figure F5. Sand-silt-clay ratio, percent biogenic and terrigenous, pebble occurrence, and linear sedimentation rate (see "Paleomagnetism," p. 11) for Site 1101. Data points in three compositional (%) columns are joined by straight lines.

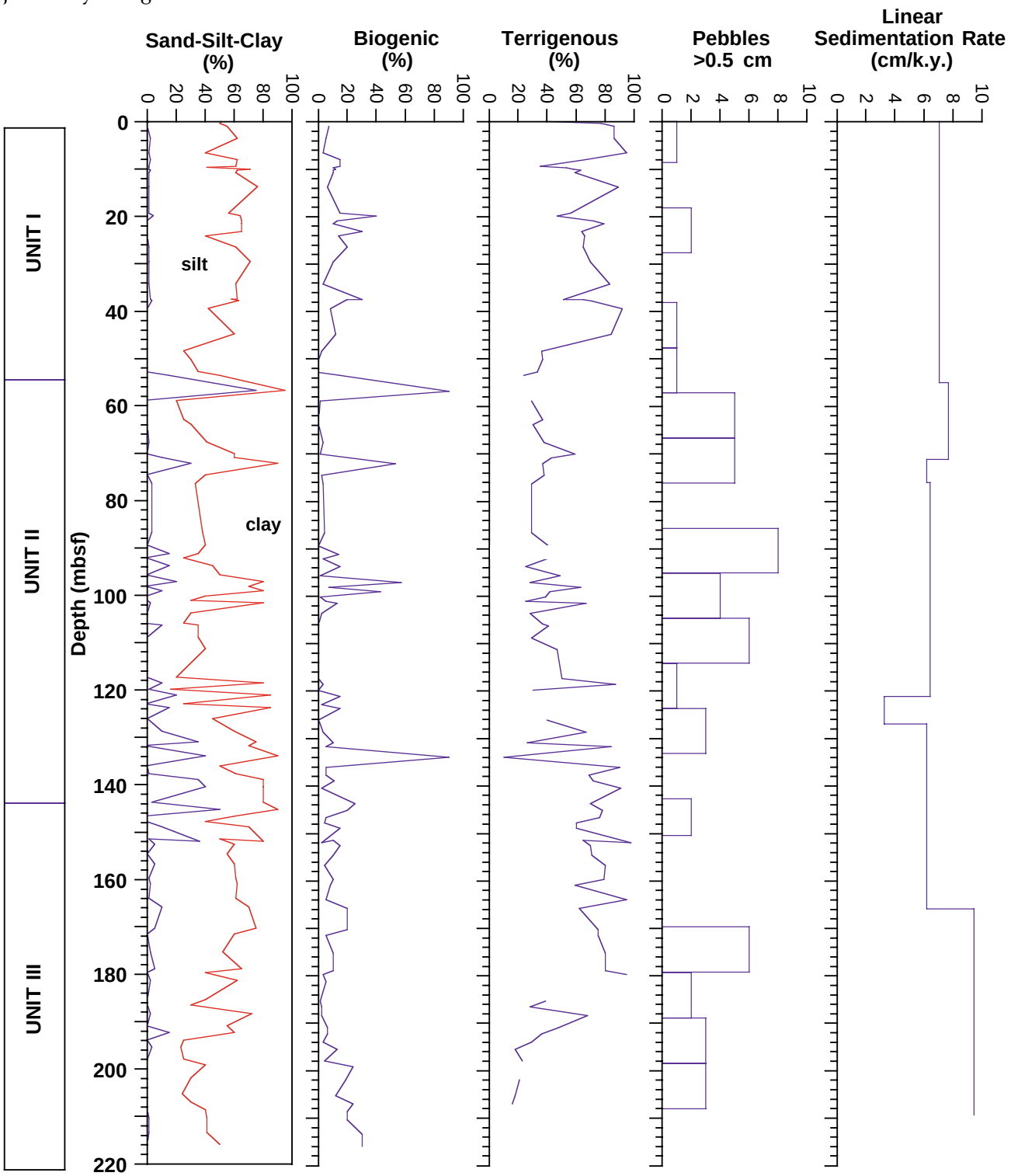

Figure F6. Graded vitric ash bed. Thin laminae of dark brown silty clay with manganese micronodules occur below (interval 178-1101A-2H-1, 103–122 cm).

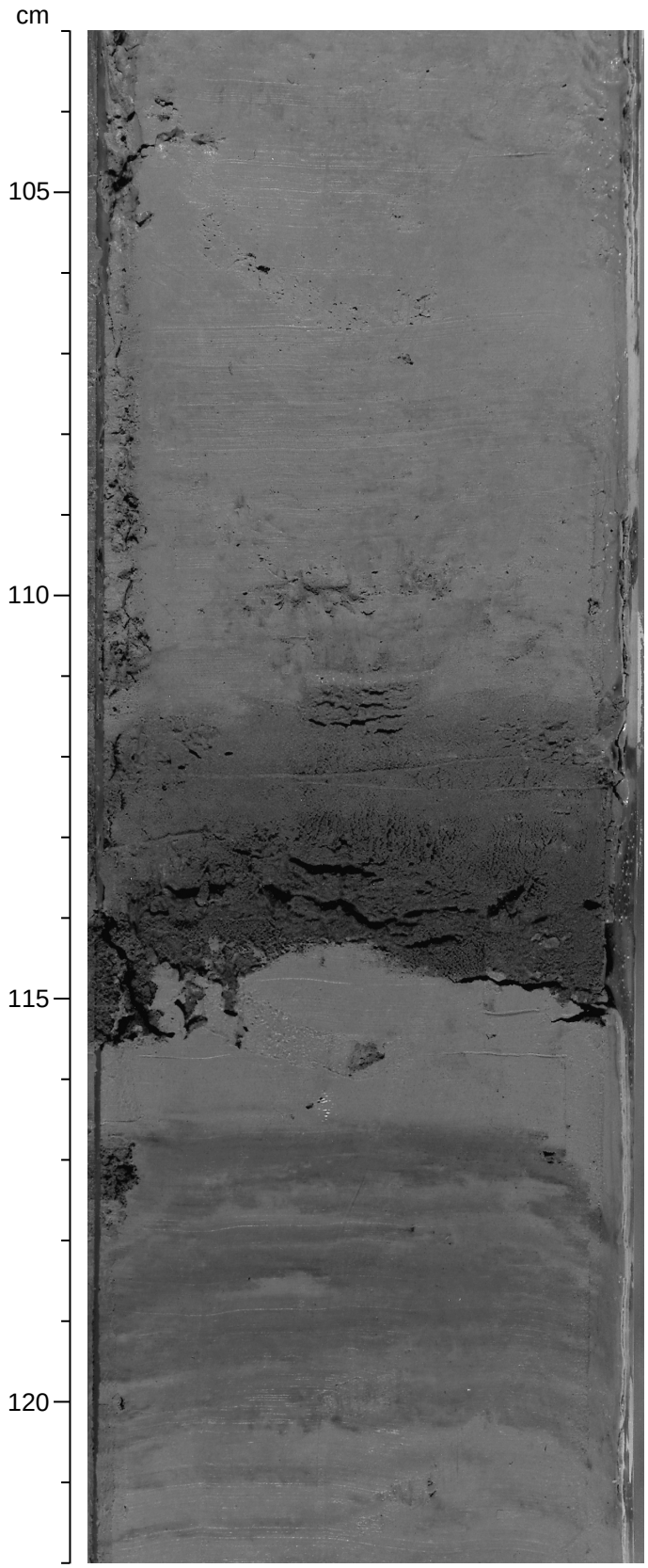

Figure F7. Laminated facies from interval 178-1101A-2H-3, 49–73 cm, within Unit I. The thicker graded silt bed at 51 cm is Facies L_1, deposited by turbidity currents. Groups of thin silt laminae between 58 and 62 cm represent Facies L_2. Facies C are the thinnest silts that appear very faintly between 51 and 58 cm. This facies is interpreted to be formed by contourites.

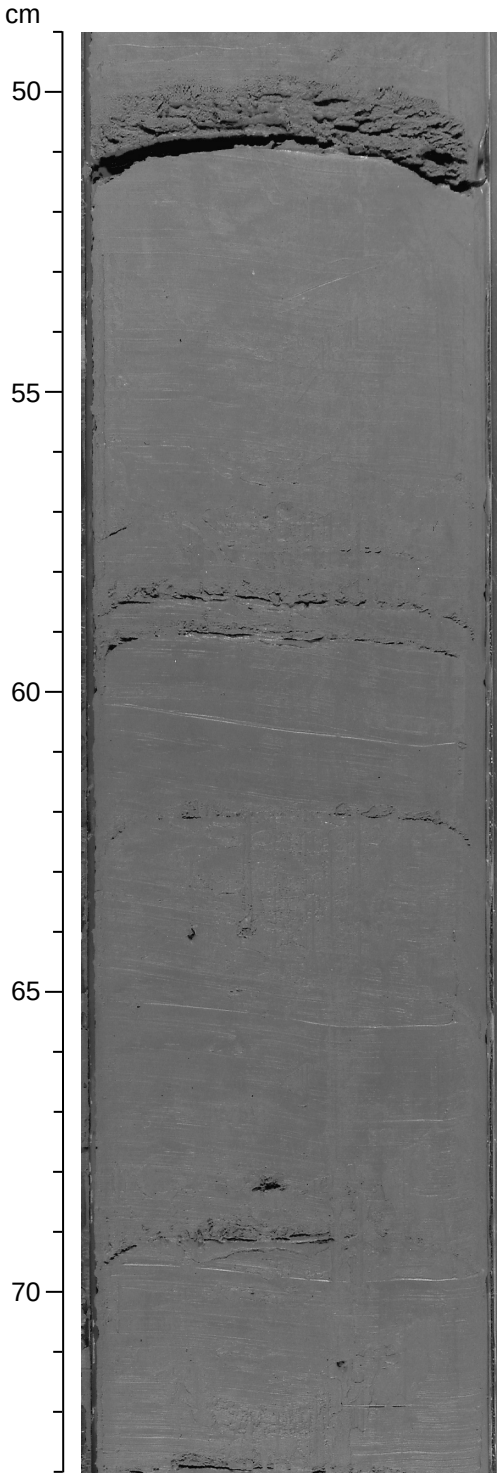

Figure F8. Magnetic susceptibility data, chromaticity parameter b*, and percent carbonate for Unit II. Chromaticity parameter b* is smoothed (nine-point moving average). Low values of magnetic susceptibility (here, magnetic susceptibility is plotted inverted) and peaks in b* correspond to the foraminifer-bearing beds that show a high percentage of carbonate. The alternating, laminated facies within Unit II has higher and variable magnetic susceptibility, and lower and variable values of b*. Each magnetic susceptibility low associated with a foraminifer-bearing bed is numbered (numbers are not oxygen isotope stages), and two lows where foraminifer-bearing clayey silt could not be identified in the core are marked "*." Low magnetic susceptibility is also associated with voids in the core (marked "V") and the occurrence of pyrite in burrows (marked "P"). High susceptibility associated with Facies L_1 is marked "T" for turbidite. The carbonate peak of 46.7% at 133.9 mbsf occurs within a carbonate-cemented silt bed.

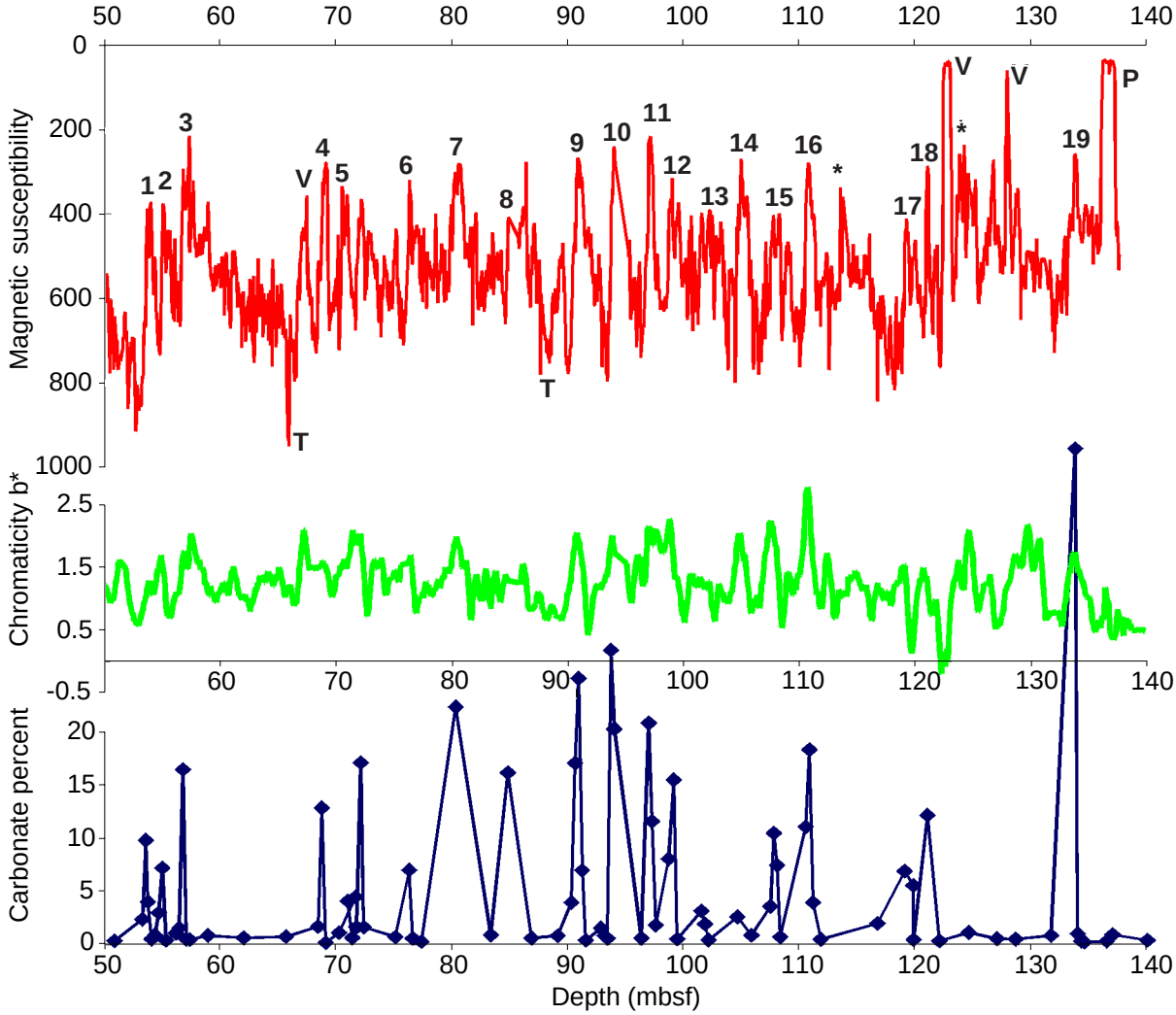

Figure F9. Facies Mf: foraminifers can be seen on the split-core surface within the foraminifer-bearing clayey silts. The rough appearance is produced by the slightly coarser grain size within these massive intervals because of the presence of foraminifers (interval 178-1101A-7H-7, 2–20 cm).

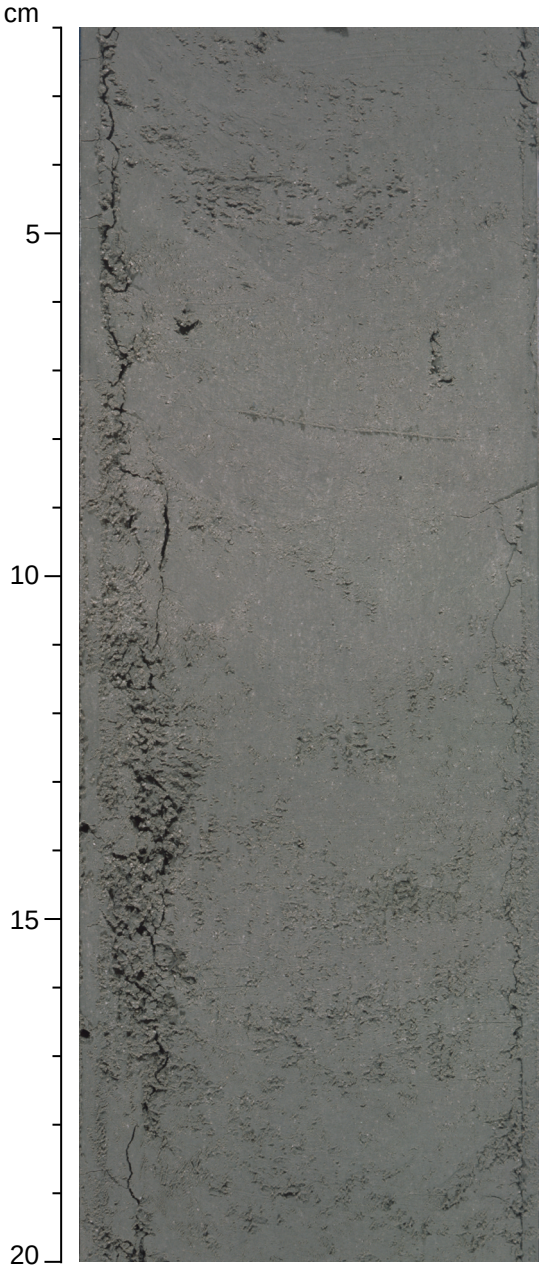

Figure F10. Laminated Facies L_2 and C in interval 178-1101A-10H-6, 17–39 cm. The spacing between Facies L_2 decreases upcore in this interval, and Facies C occurs between. Evidence of ice rafting within the laminated facies can been seen by granules floating in mud at 37 cm.

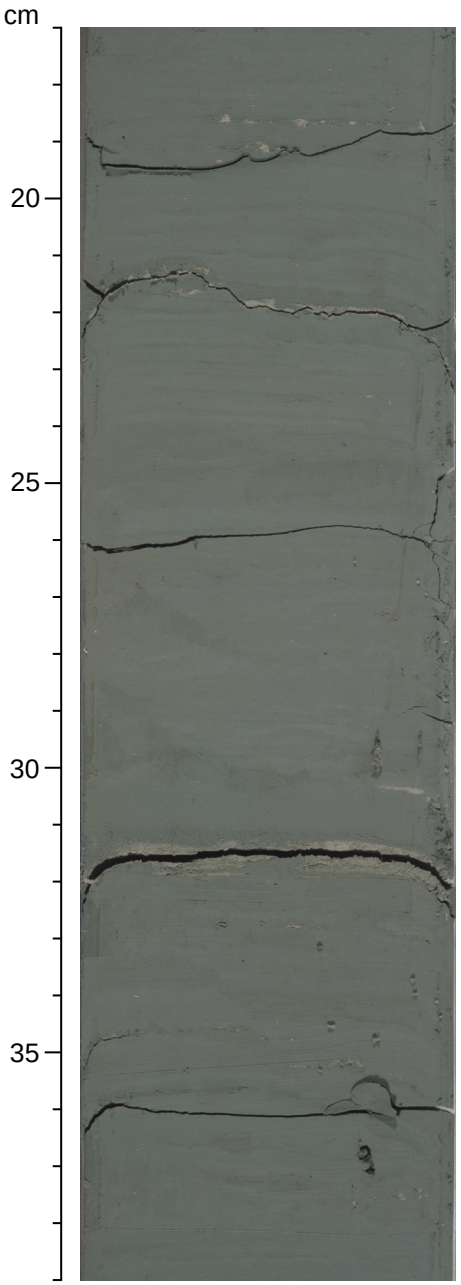

Figure F11. Facies L_1 occurs uncommonly within Unit II. A good example of a turbidite is shown in interval 178-1101A-14H-2, 97–112 cm. This 3-cm-thick silt bed is ripple cross-laminated and has an erosive base.

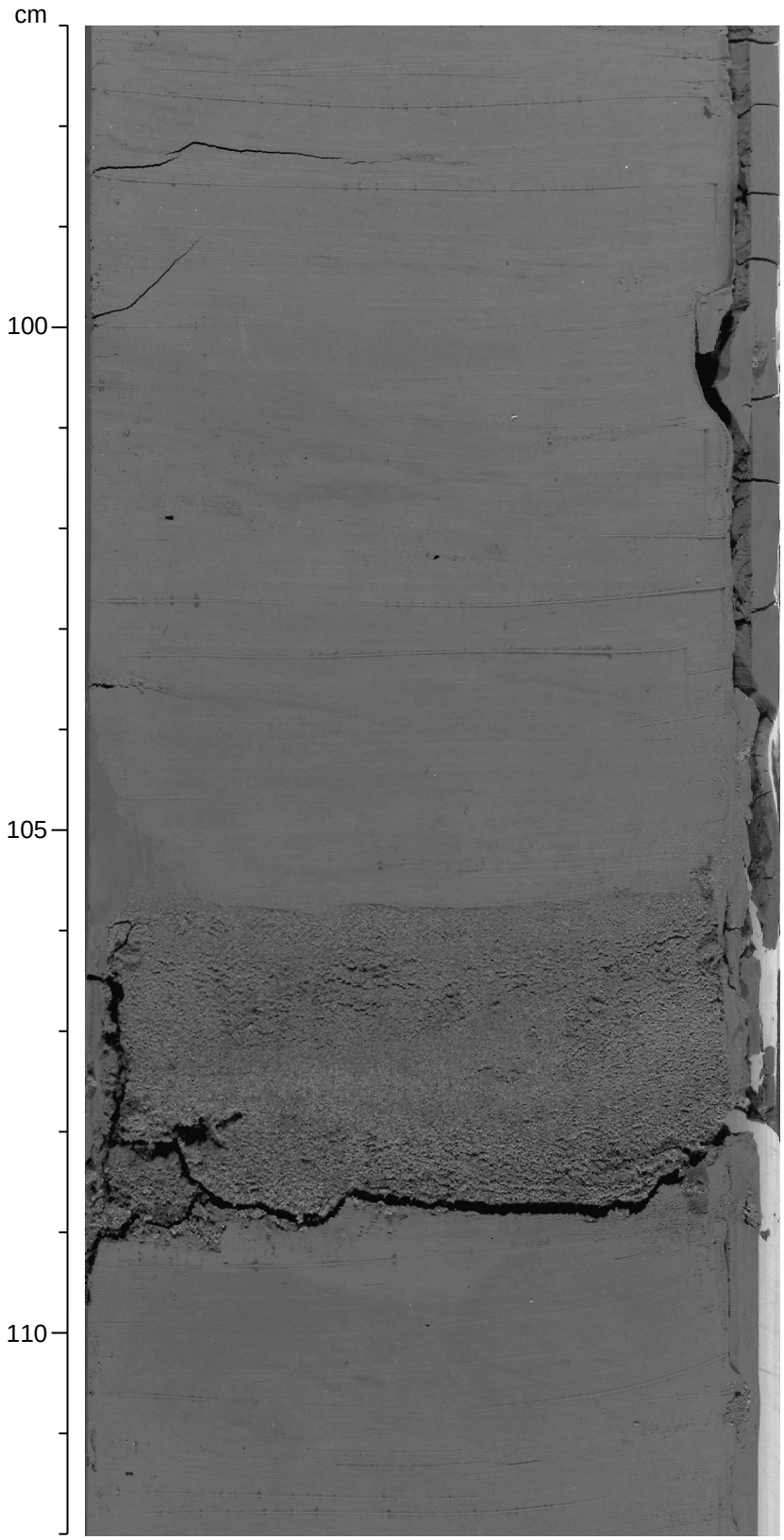

Figure F12. Facies C can be seen within the biscuits of interval 178-1101A-24X-1, 44–64 cm. A vertical pyrite-filled burrow occurs at 51 cm.

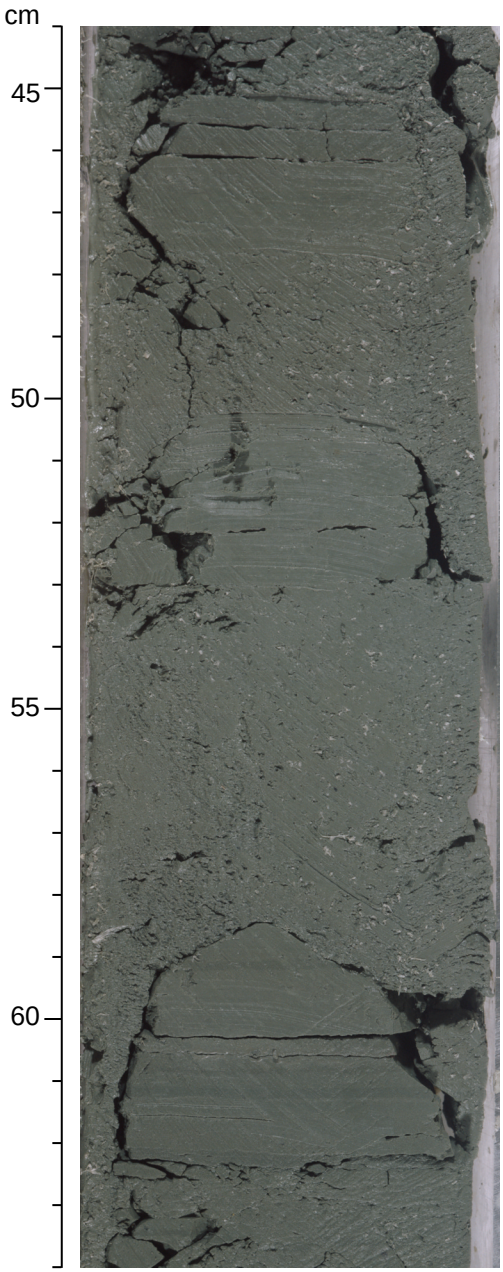

Figure F13. The thickest and coarsest-grained example of L_1 facies occurs within Unit III in interval 178-1101A-23X-6, 37–59 cm. It coincides with a peak in magnetic susceptibility.

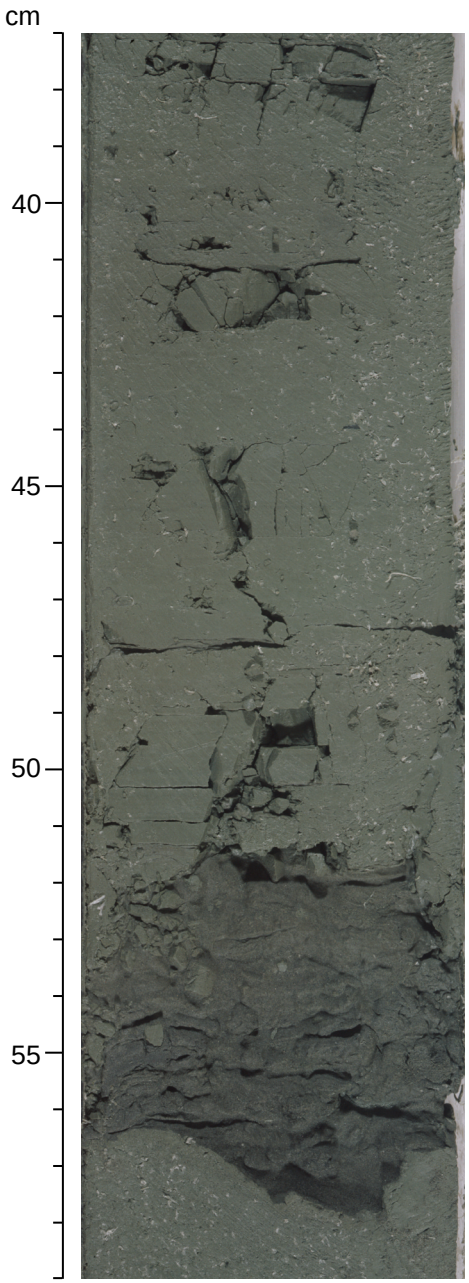

Figure F14. Diamict facies in Unit III. The clasts are of volcanic and plutonic rocks and range up to 1 cm diameter (interval 178-1101A-22X-2, 130–150 cm).

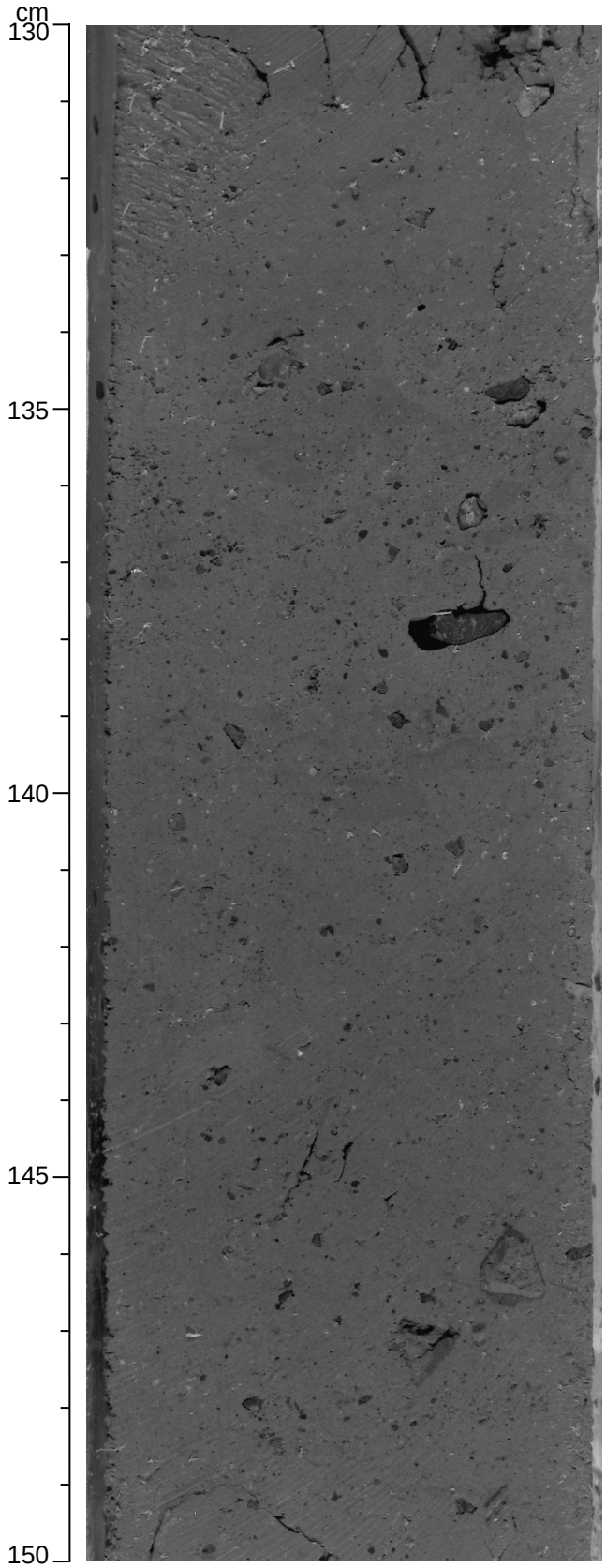

Figure F15. Dropstone from Section 178-1101A-6H-5. This basalt pebble has striations and facets that indicate subglacial transport.

Figure F16. Zonal assignments of Site 1101 for calcareous nannofossils, diatoms, radiolarians, and foraminifers. Stippled areas = intervals barren (or nearly barren) of the particular fossil group. Age division provided by comparative assessment of diatoms and paleomagnetic data. B = base (first occurrence), T = top (last occurrence).

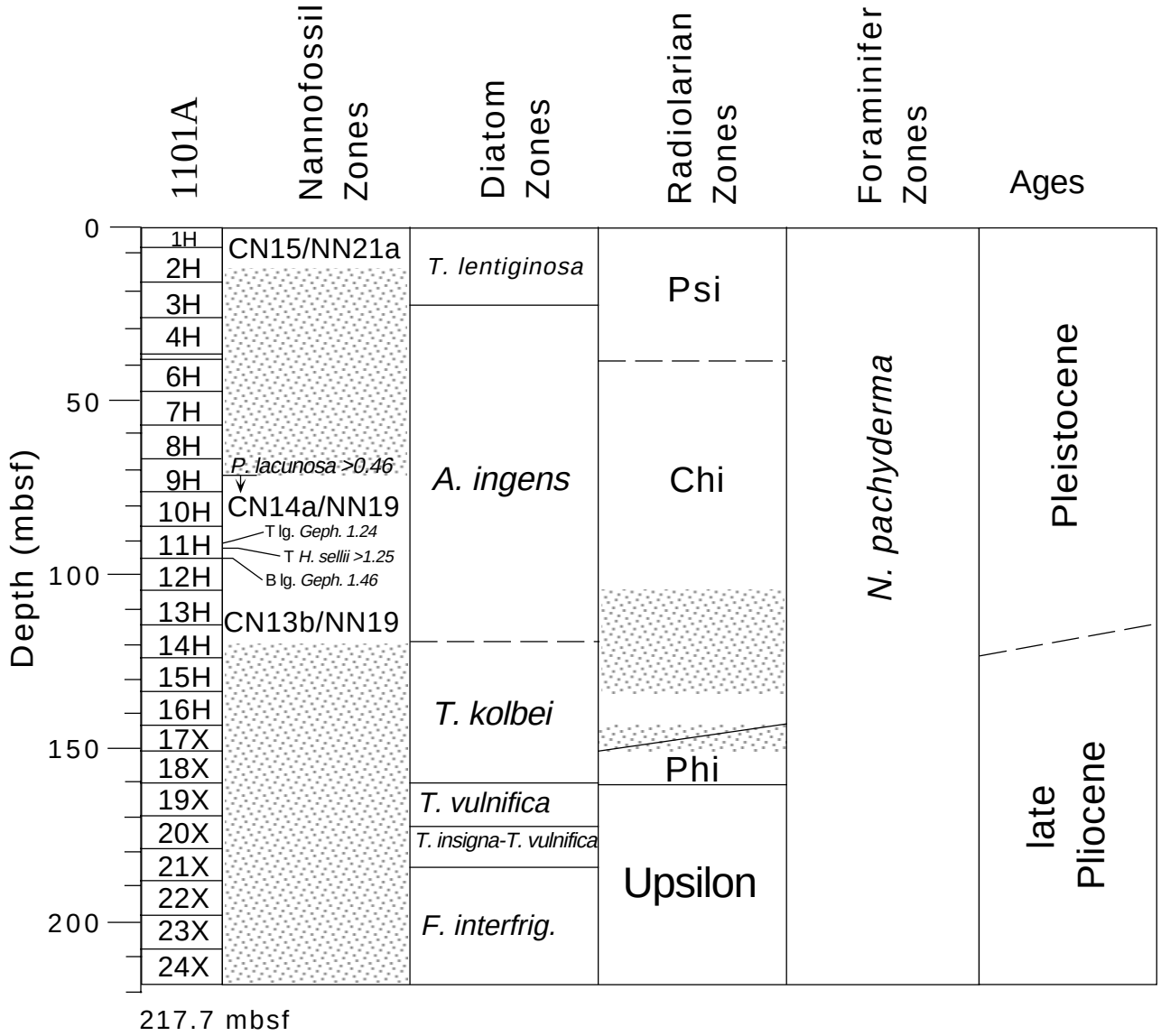

Figure F17. Histogram of inclinations at Site 1101 after AF demagnetization of the NRM at 30 mT.

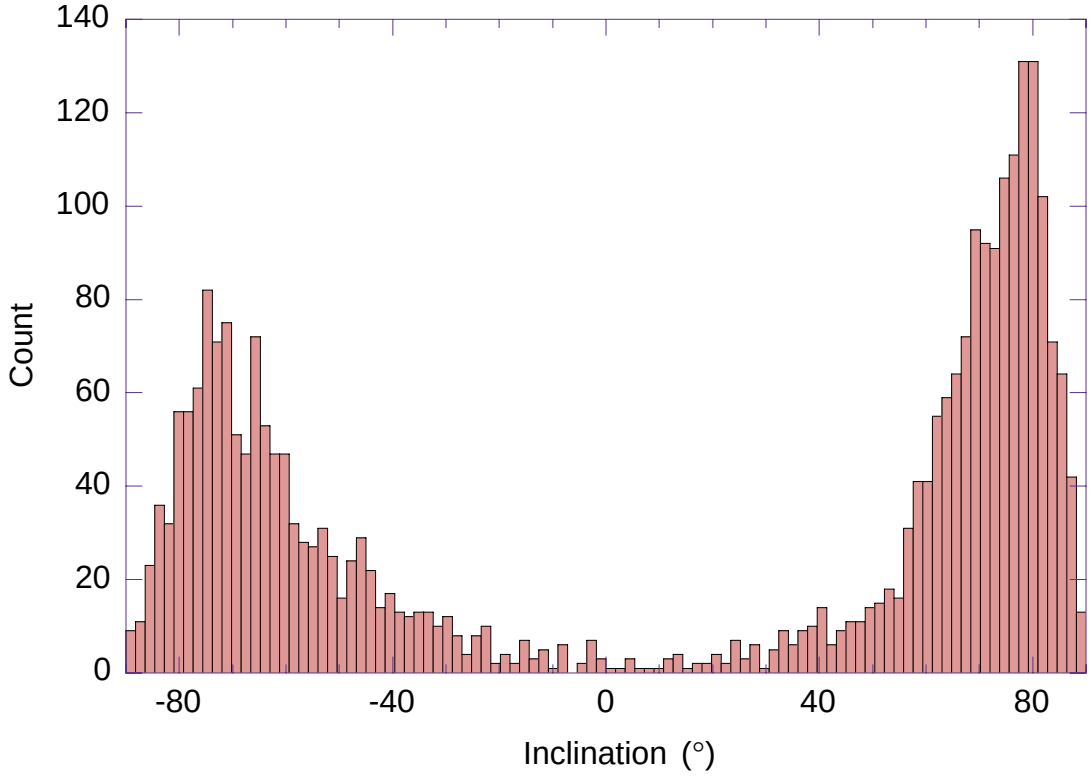

Figure F18. Inclination and intensity of magnetization for Hole 1101A after AF demagnetization at 30 mT, with the interpreted magnetostratigraphy. Inclinations obtained from principal component analysis of discrete samples are shown by solid squares.

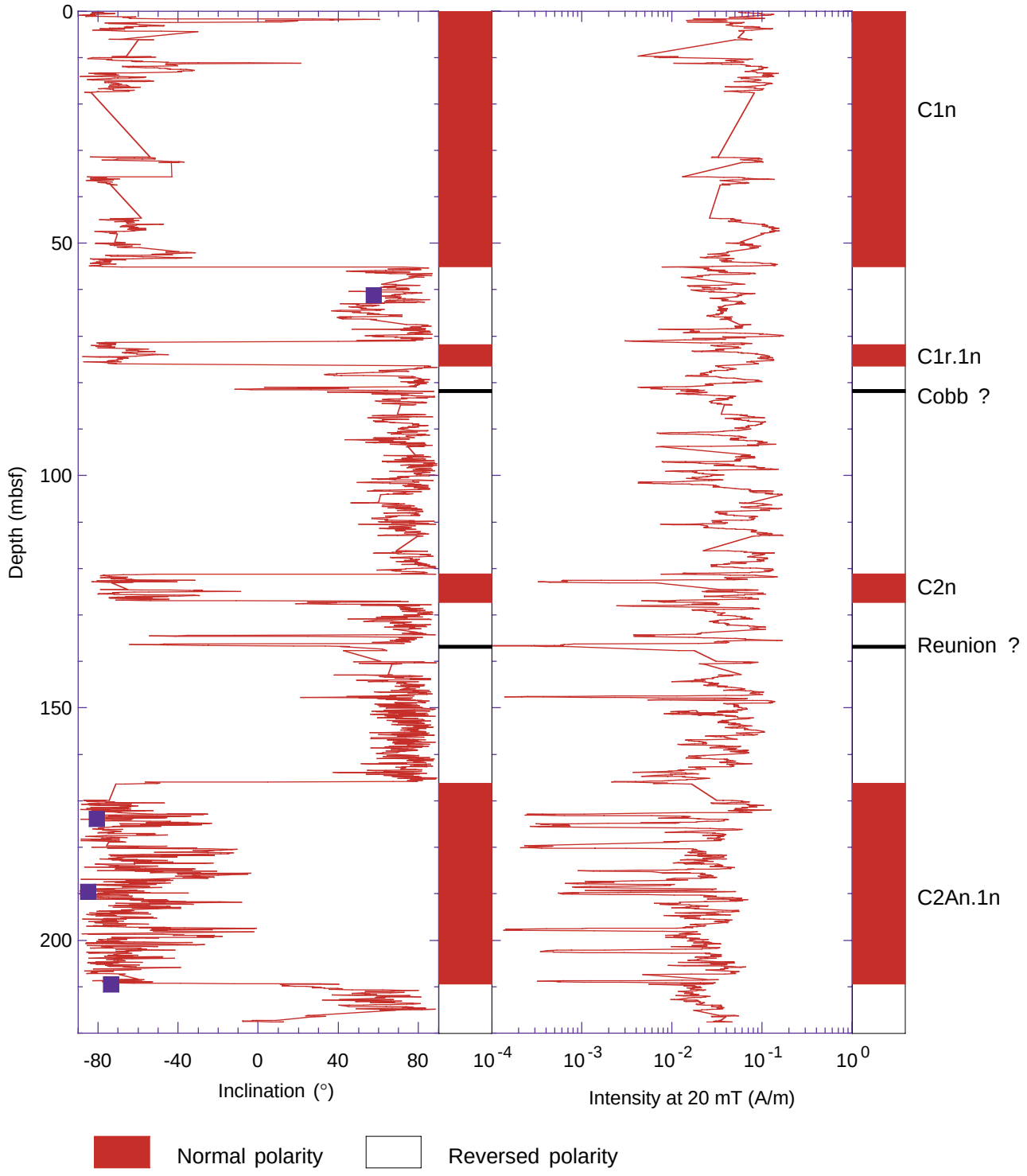

Figure F19. Variation in headspace methane concentration with depth for Hole 1101A.

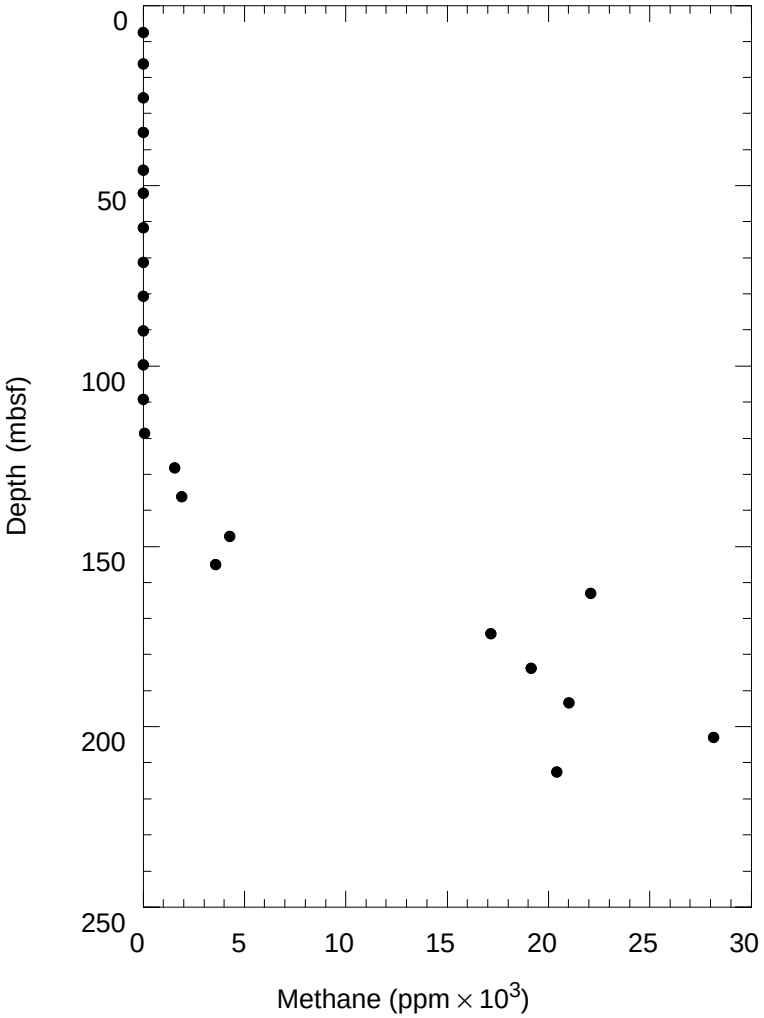

Figure F20. Calcium carbonate content in samples from Site 1101. Lithostratigraphic Units I–III are shown for reference.

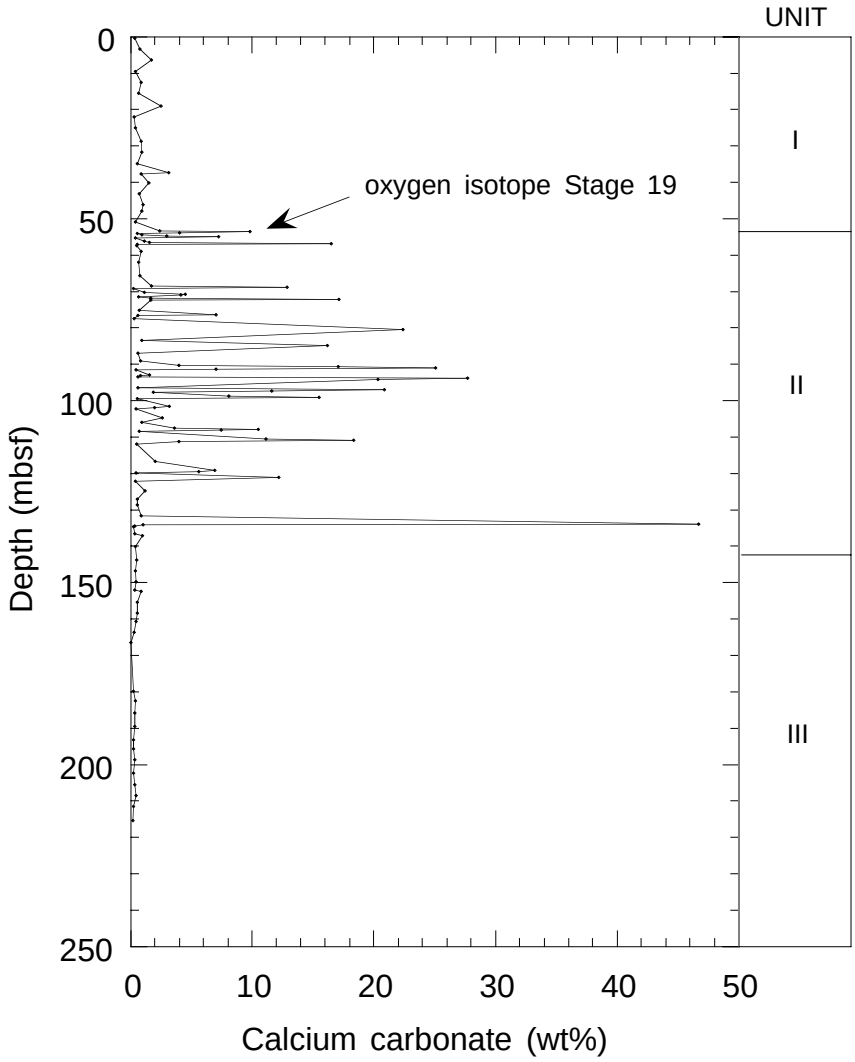

Figure F21. Total organic carbon in samples from Site 1101. Lithostratigraphic Units I–III are shown for reference.

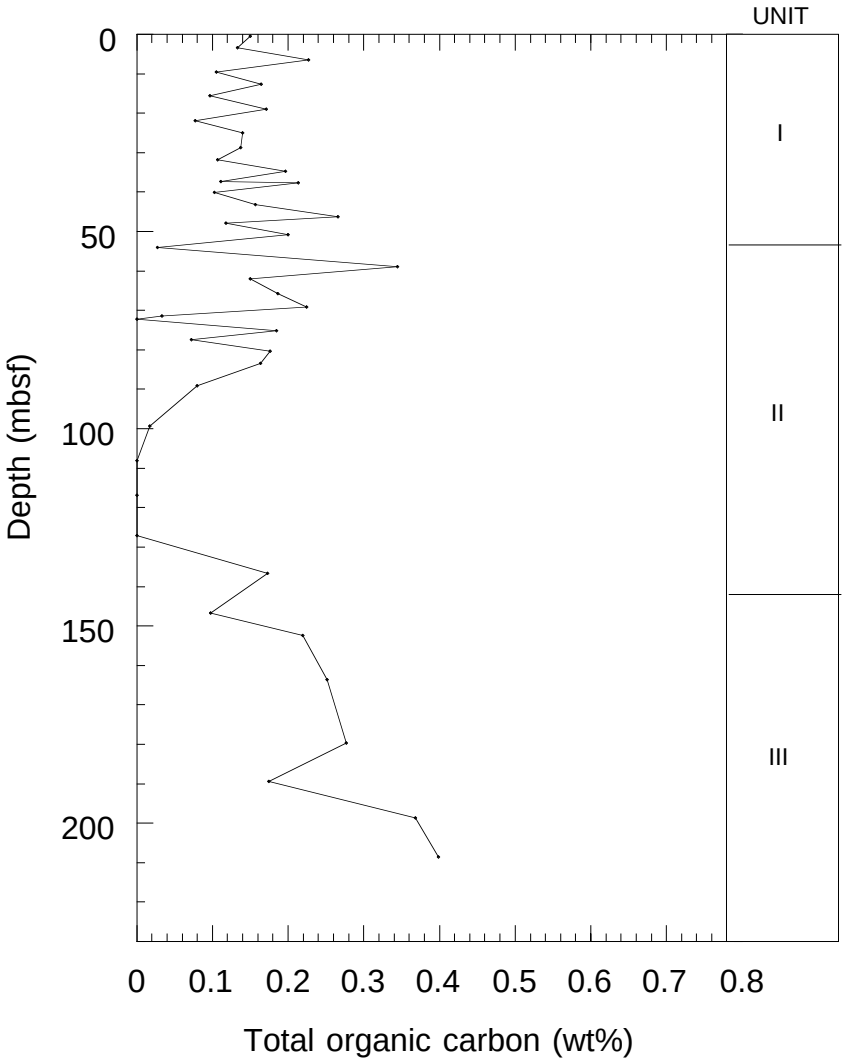

Figure F22. Profiles of interstitial water chemistry from Hole 1101A.

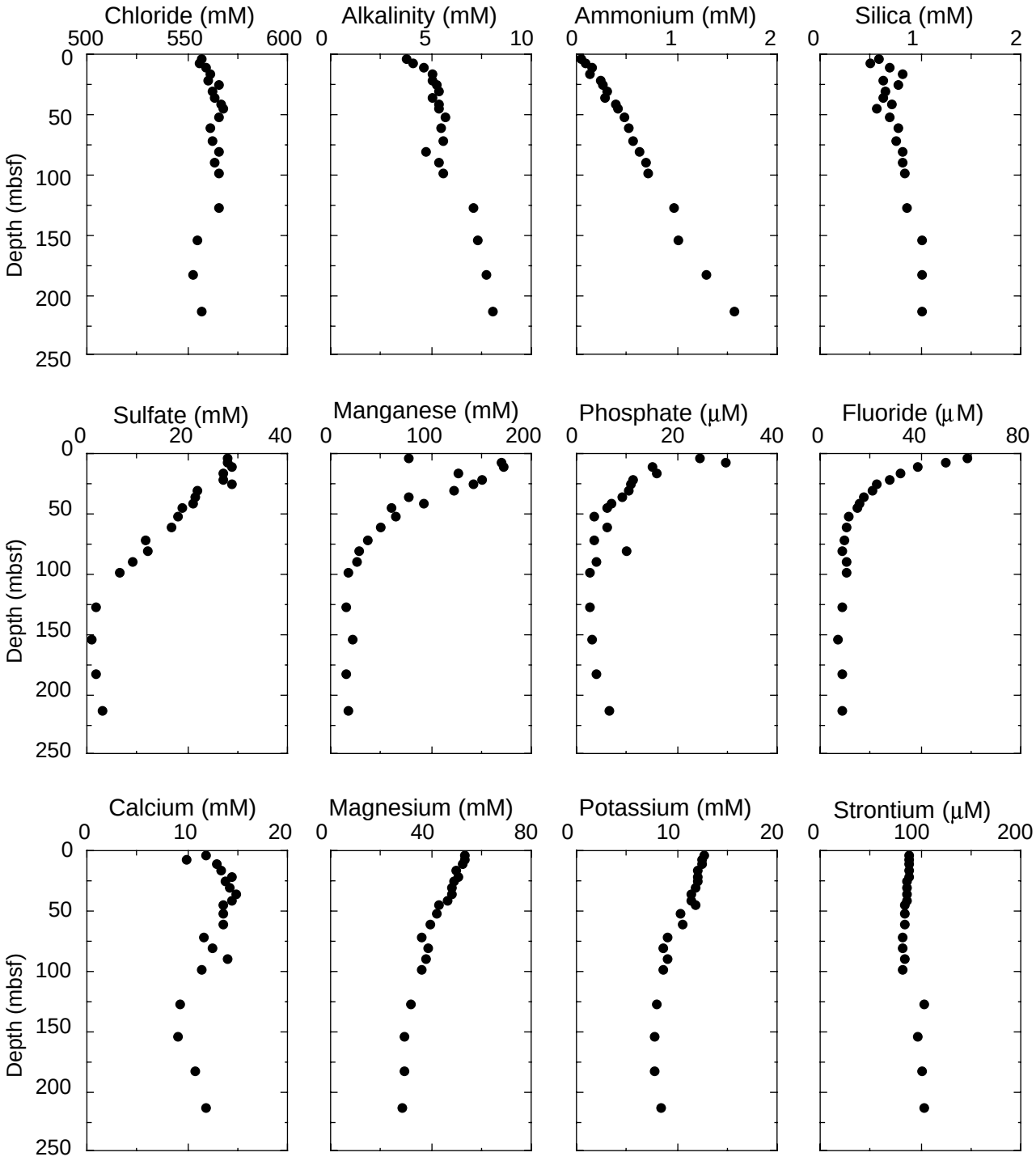

Figure F23. Ratios between X-ray diffraction intensities of selected peaks for chlorite (7 Å), illite (5 Å), and mixed-layer (~12 Å) clays in clay-sized sediment fractions from Site 1101. Peak height ratios do not reflect absolute concentrations. For comparison, concentrations of calcite (wt%) are included for samples from Core 178-1101A-10H.

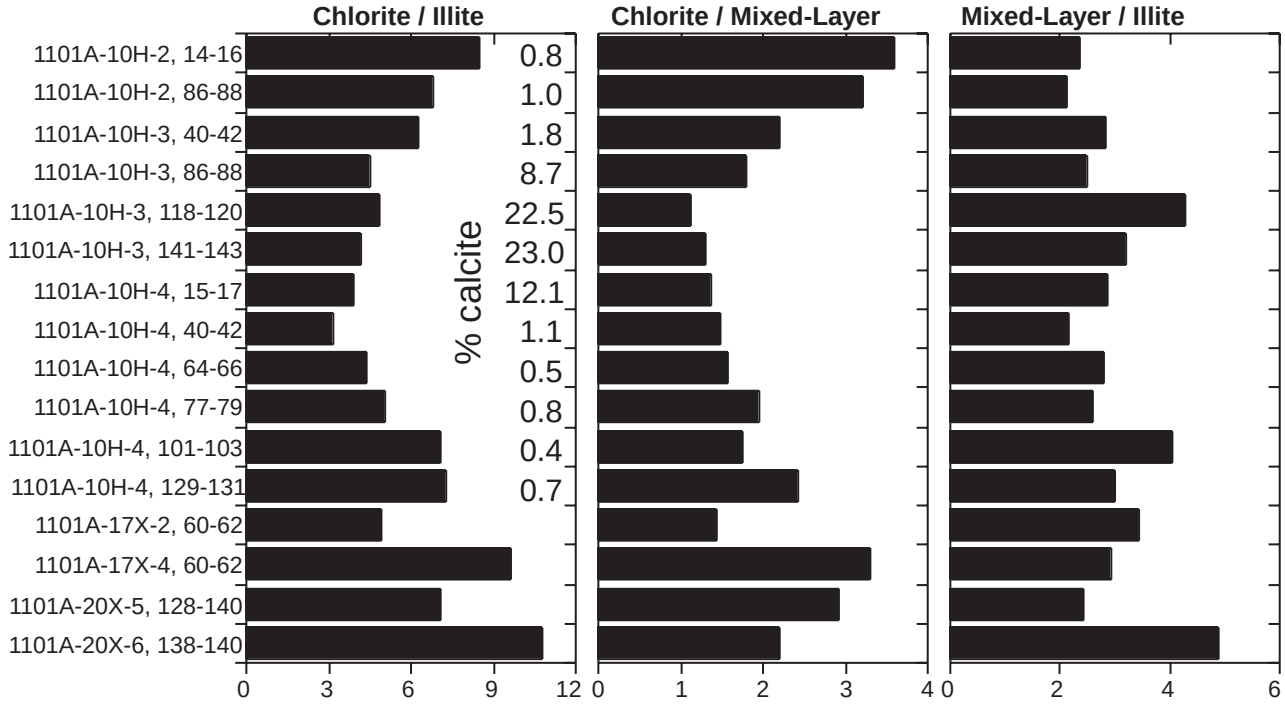

Figure F24. Relative abundances of chlorite, illite, and mixed-layer clays in sediments from the continental shelf (Site 1097) and rise (Sites 1095, 1096, and 1101) analyzed on Leg 178. Axes are in arbitrary units based on diffraction intensities and do not imply absolute concentrations.

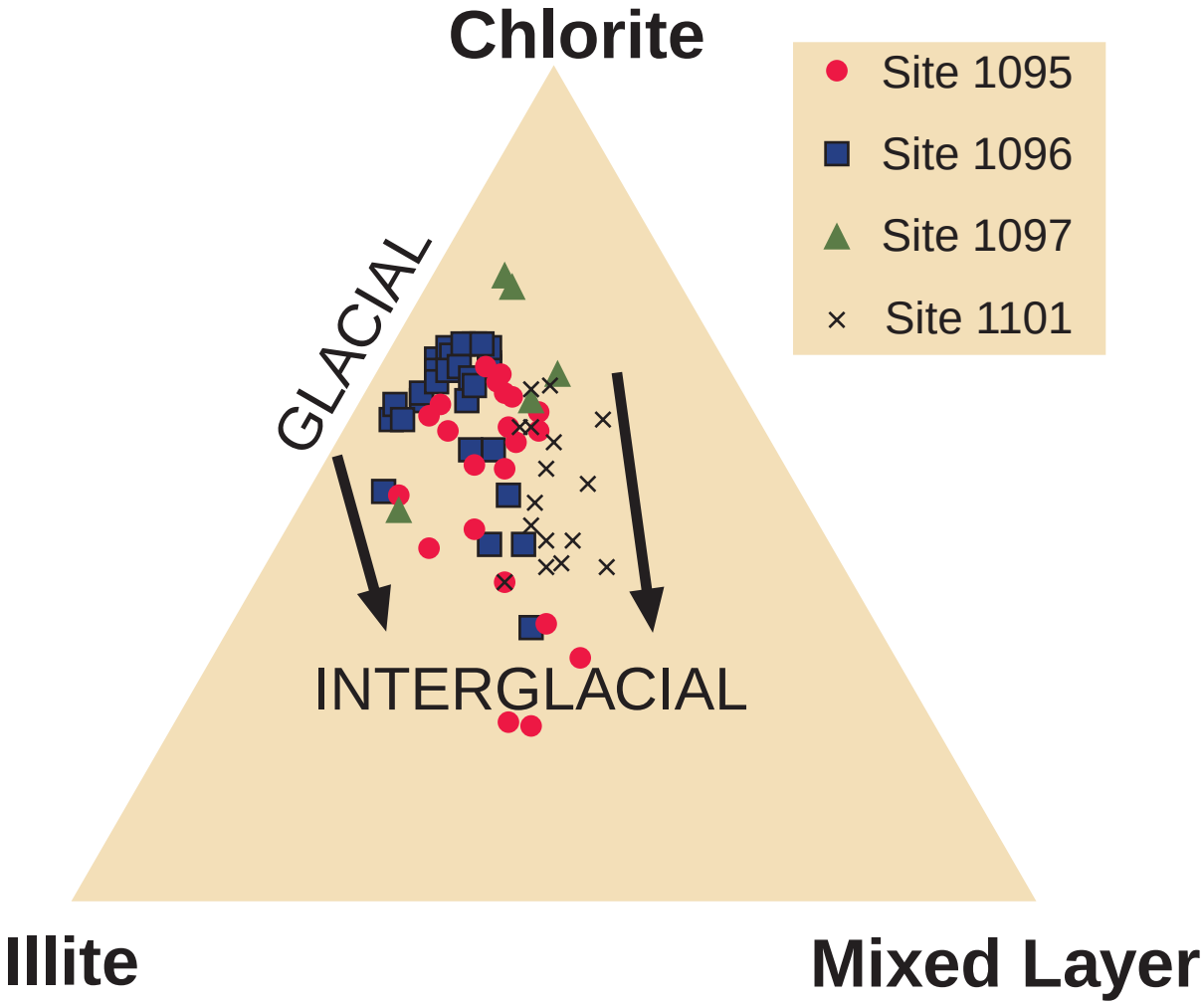

Figure F25. Raw data for **(A)** NGR, **(B)** GRAPE density, **(C)** magnetic susceptibility, and **(D)** *P*-wave velocity. GRAPE data were truncated at 1.2 g/cm³, susceptibility data were truncated at 0, and *P*-wave velocity data were truncated at 1800 and 1450 m/s to remove equipment noise.

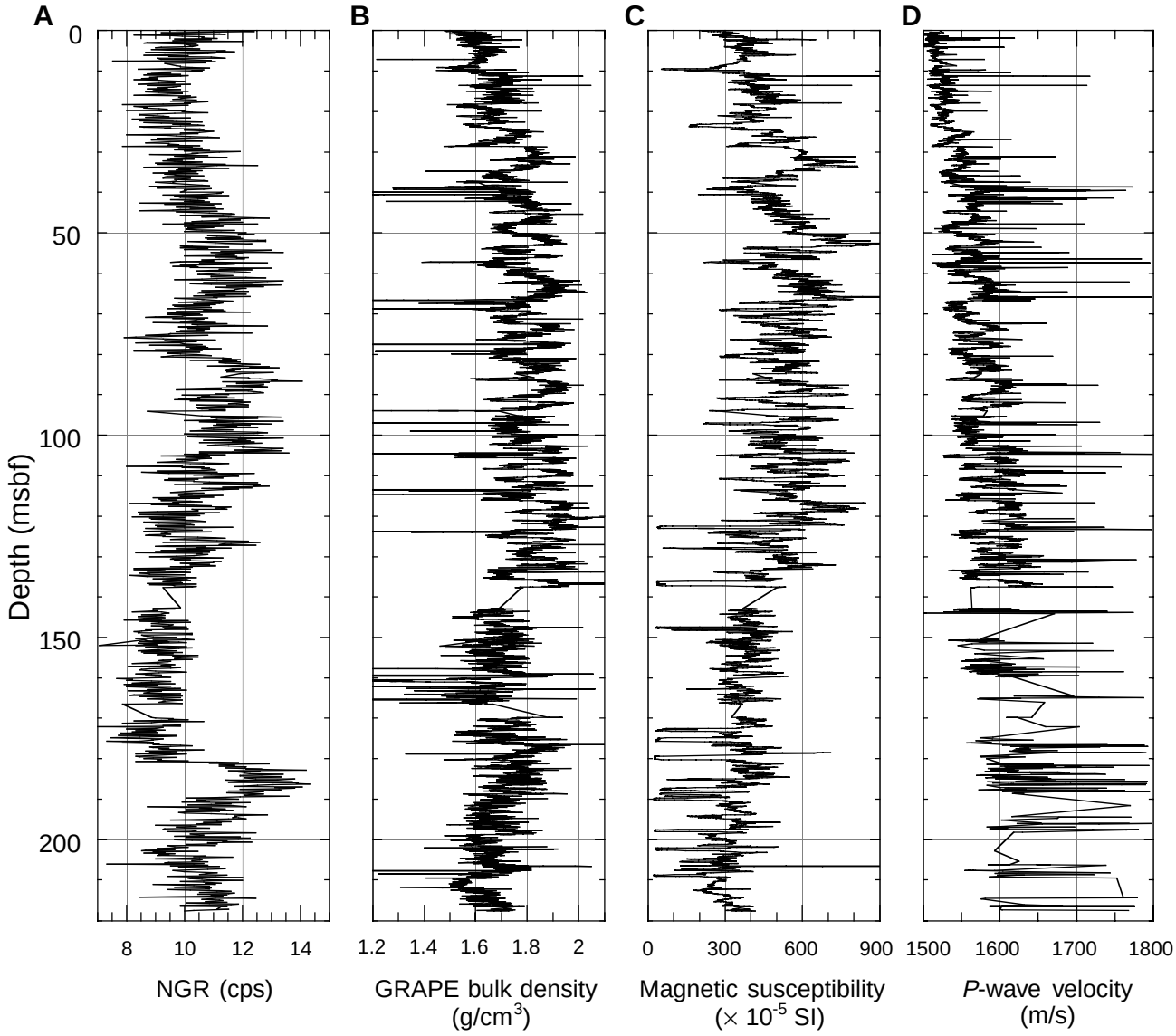

Figure F26. **(A)** NGR, **(B)** GRAPE density, **(C)** magnetic susceptibility, and **(D)** *P*-wave velocity vs. depth. A Gaussian filter was applied to the data to attenuate high-frequency variability. The filter was centered around 4 m, with a high-frequency truncation length at ~1.3 m and a low-frequency truncation approaching infinity.

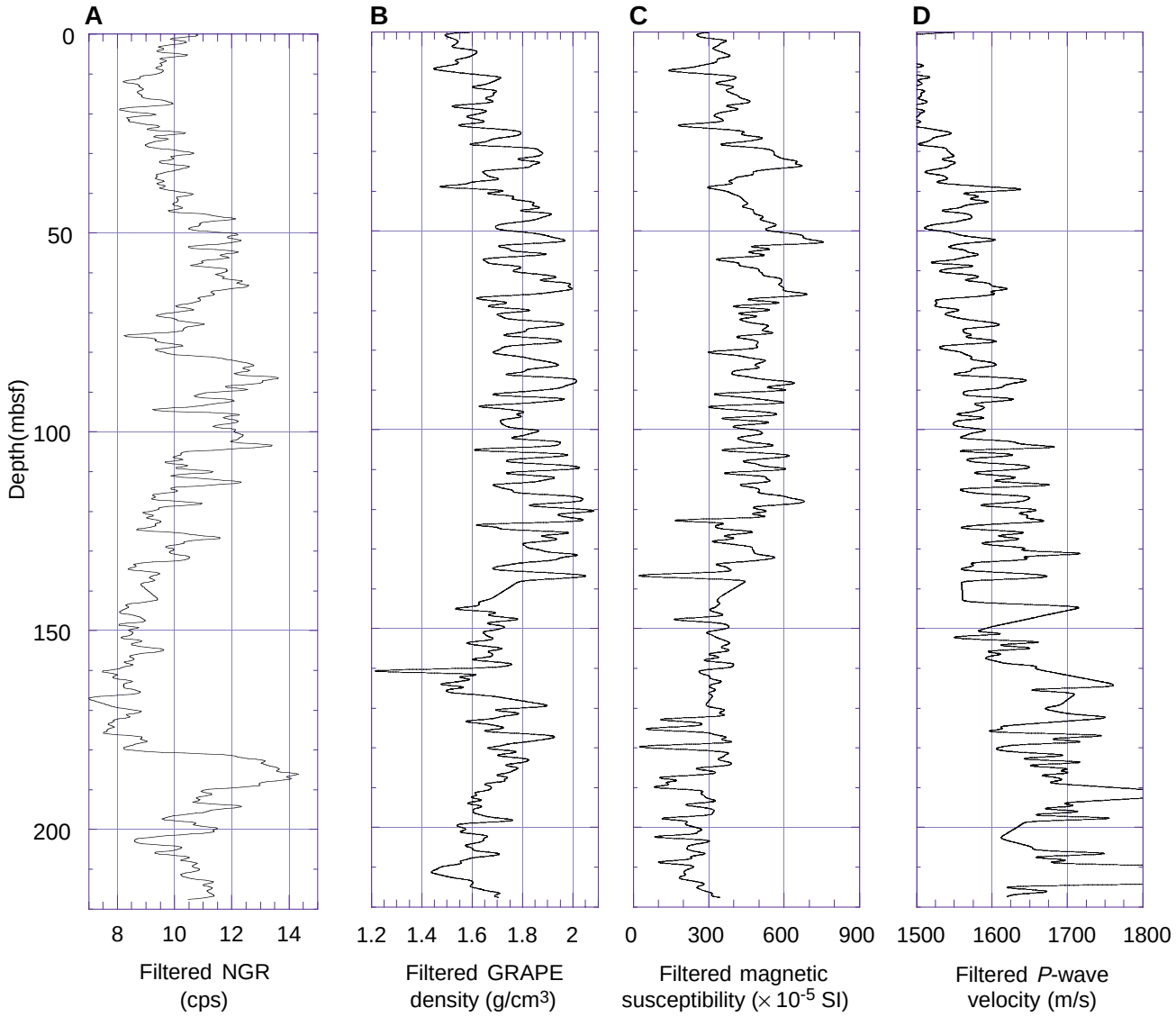

Figure F27. **(A)** NGR, **(B)** GRAPE density, **(C)** magnetic susceptibility, and **(D)** *P*-wave velocity vs. age. After age scaling, the data were filtered as in Figure F26, p. 51 (Gaussian filter, centered at 25 k.y., with a high-frequency cut-off at ~8 k.y. and a low-frequency truncation approaching infinity).

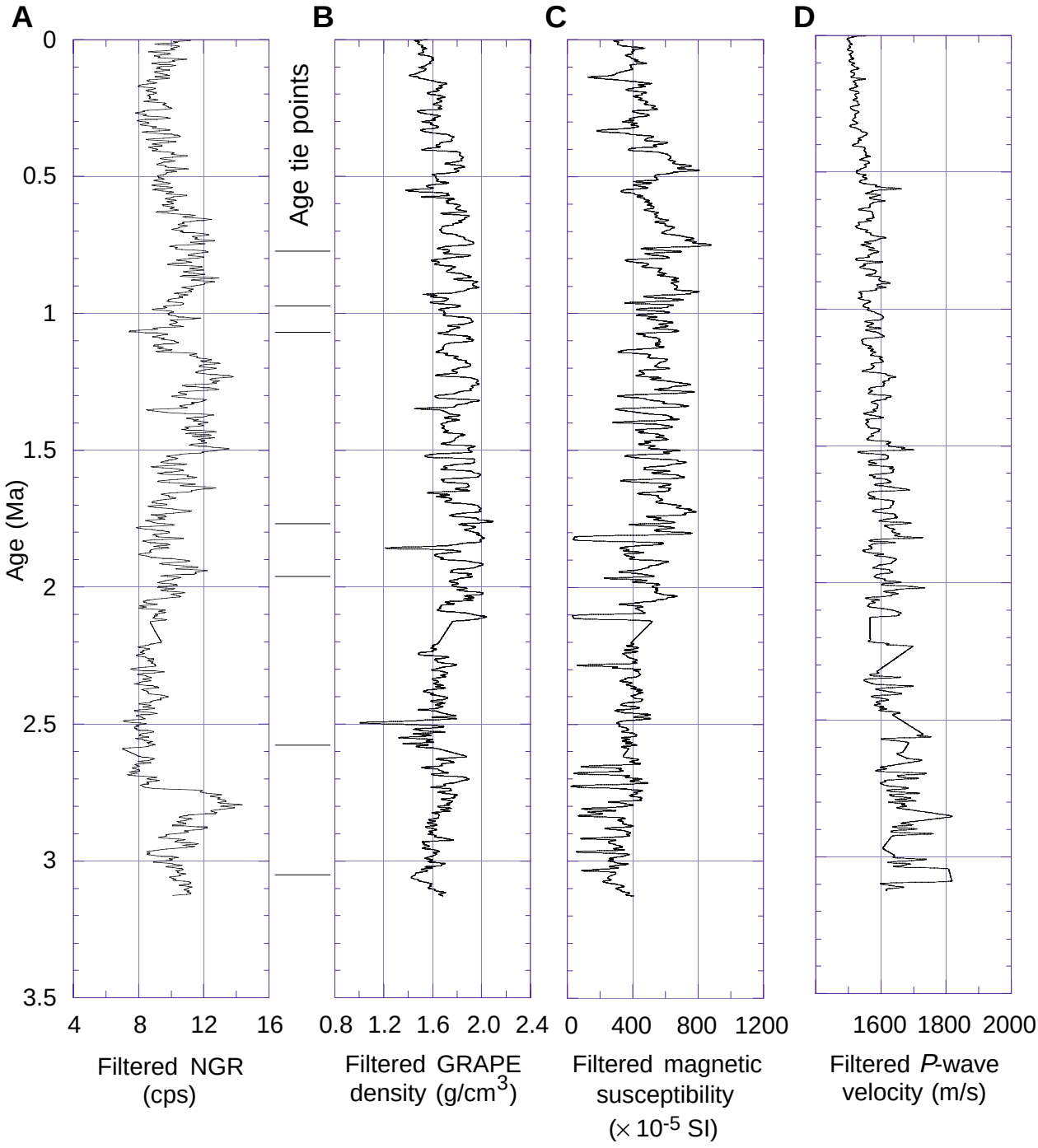

Figure F28. Plots of **(A)** filtered GRAPE and bulk density (MAD) from raw index properties, **(B)** grain density, and **(C)** porosity vs. depth. MAD = moisture and density measurements.

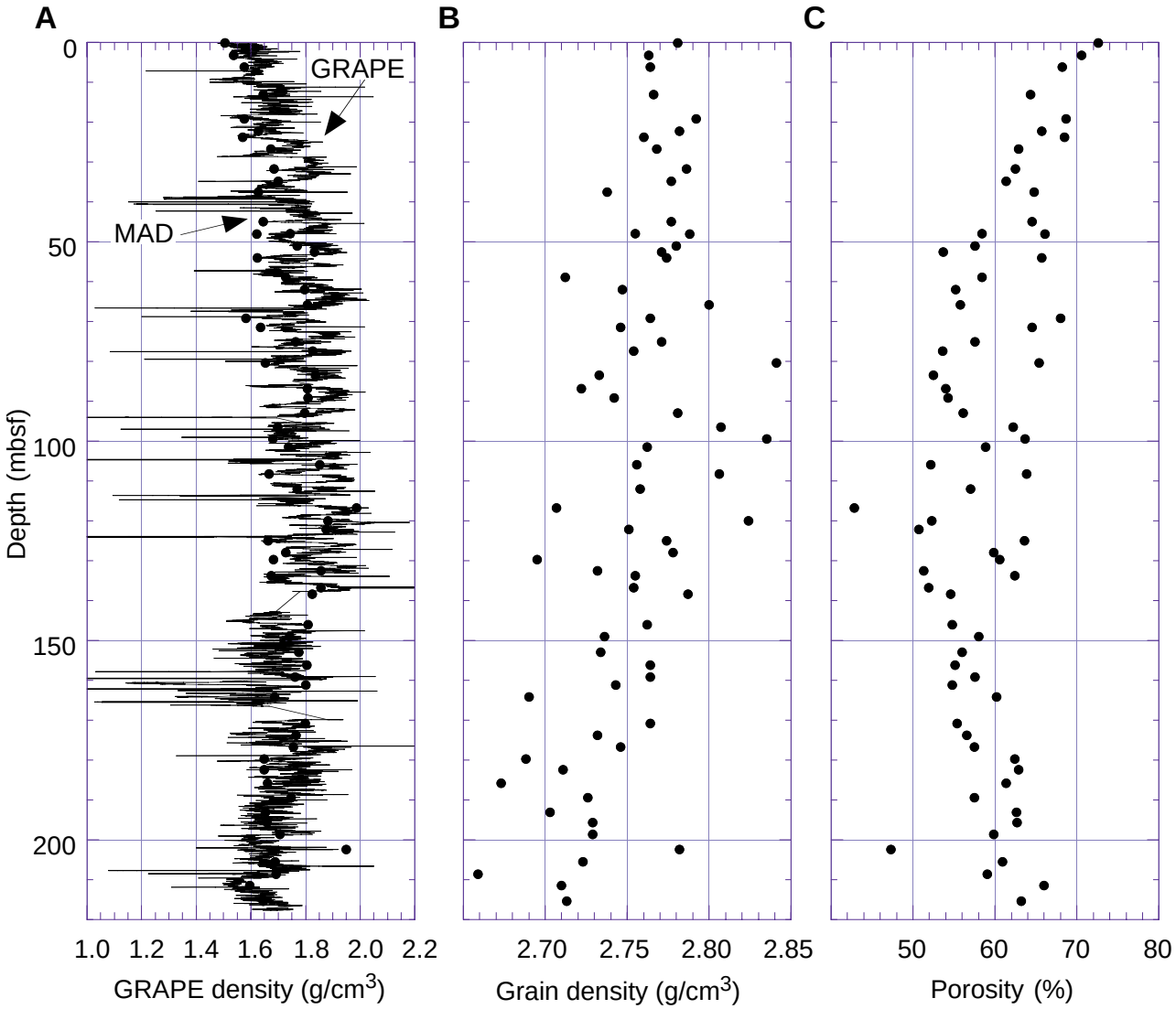

Figure F29. Total biogenic content and porosity vs. depth.

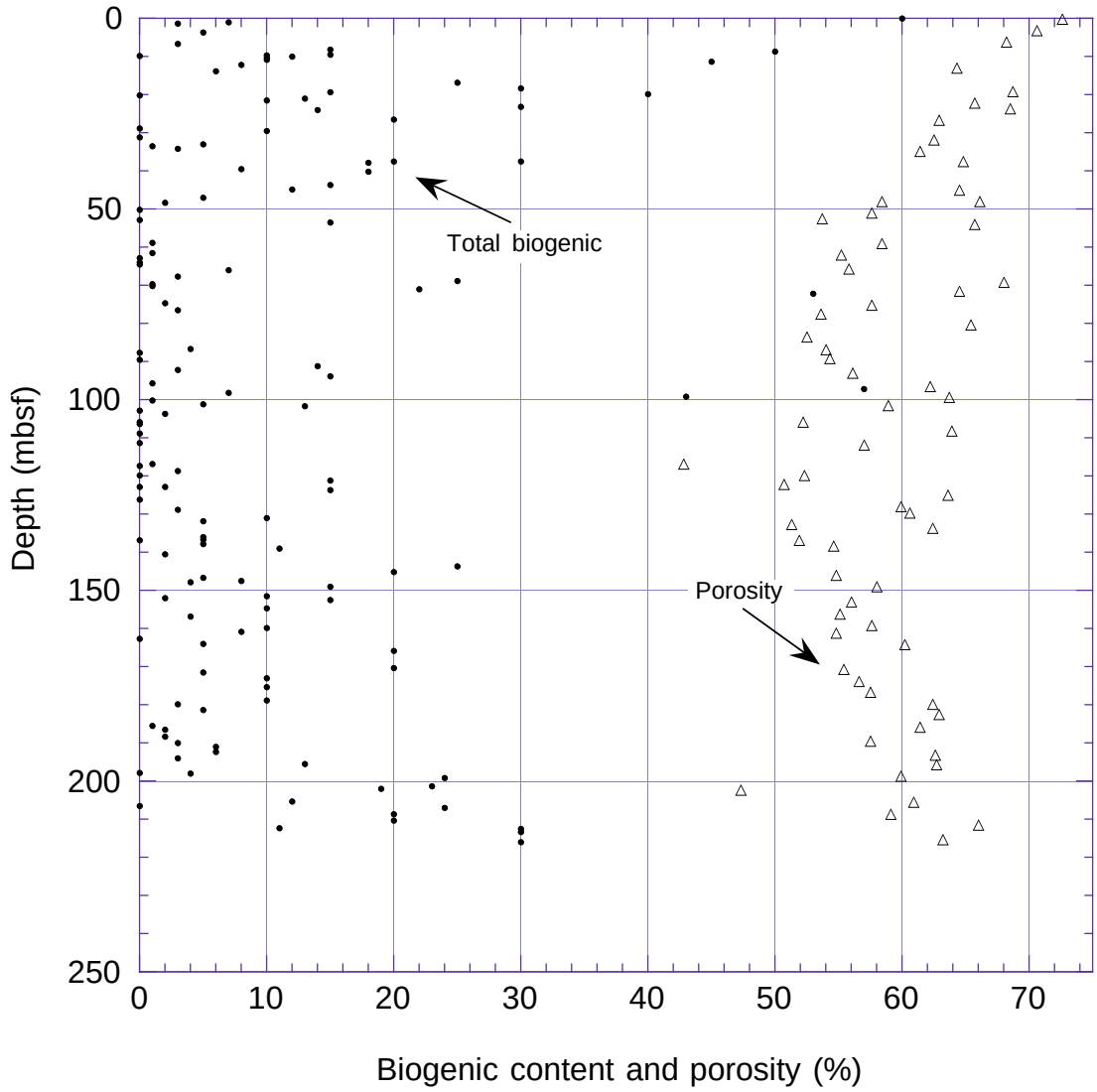

Figure F30. Raw PWS1, PWS2, and PWS3 data plotted vs. depth for the upper 50 mbsf of Hole 1101A.

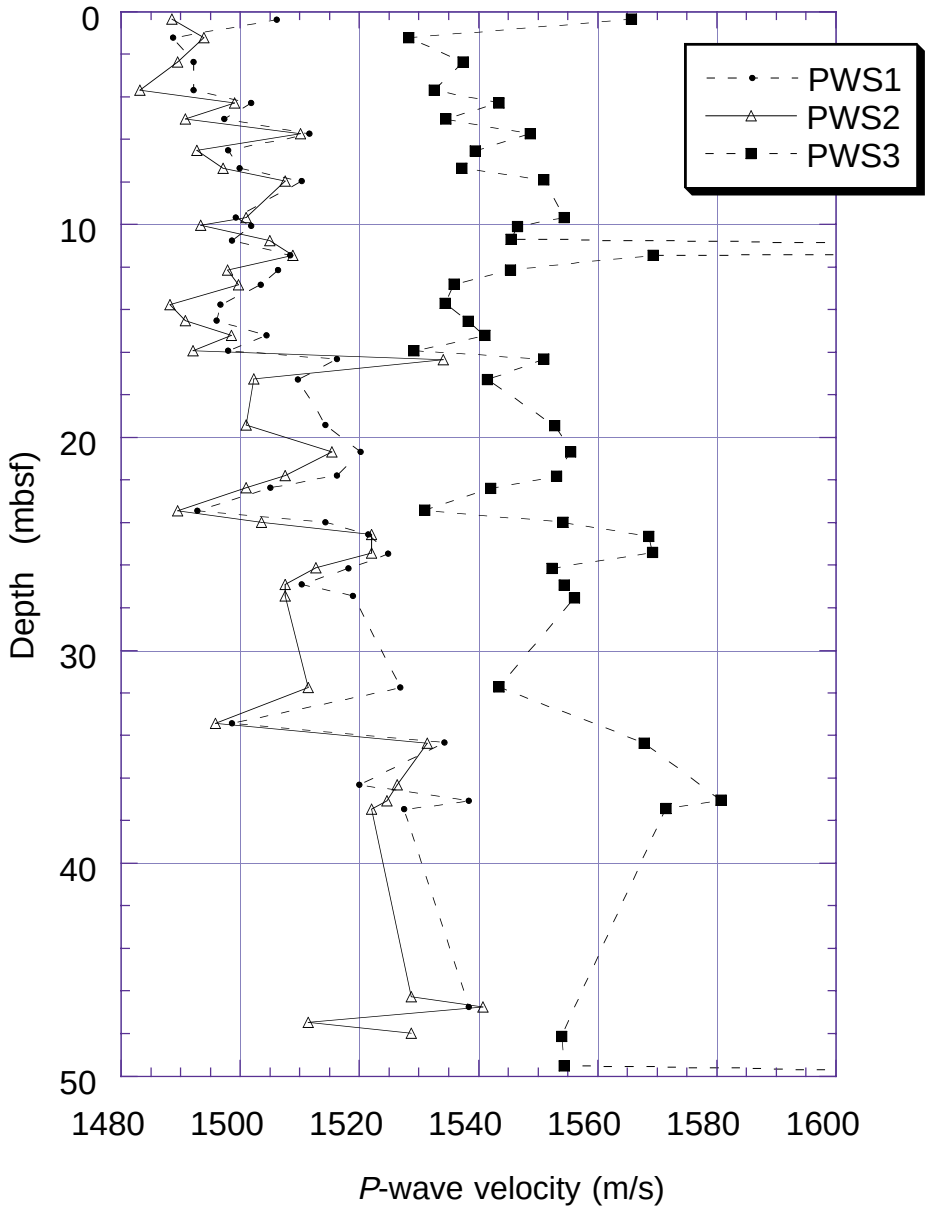

Figure F31. Raw PWS3 data plotted vs. depth for Hole 1101A.

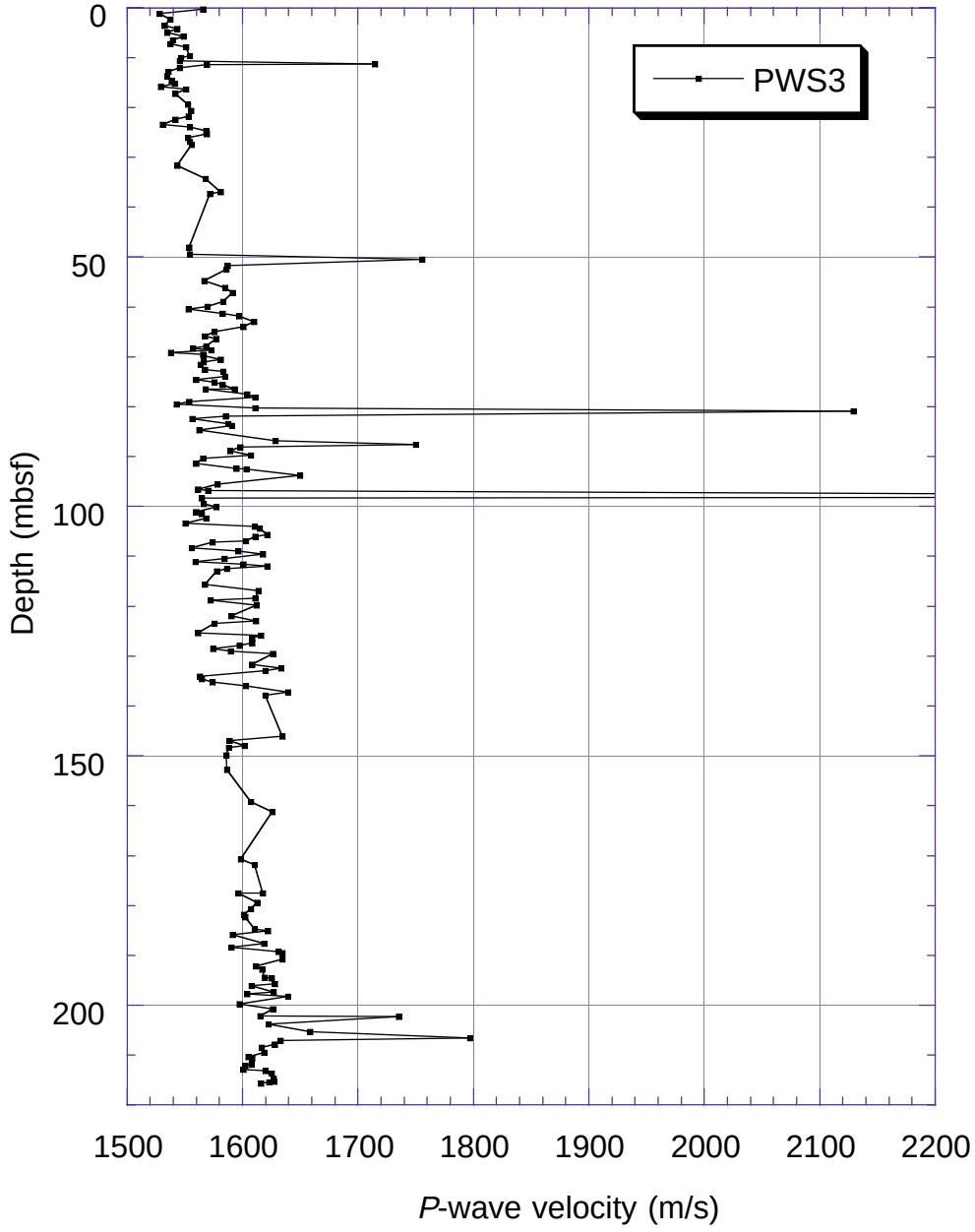

Figure F32. Thermal conductivity measurements at Site 1101. The straight line is the best fit to values below 31 mbsf (diamonds). Values above 22 mbsf (squares) are significantly lower because of high porosity.

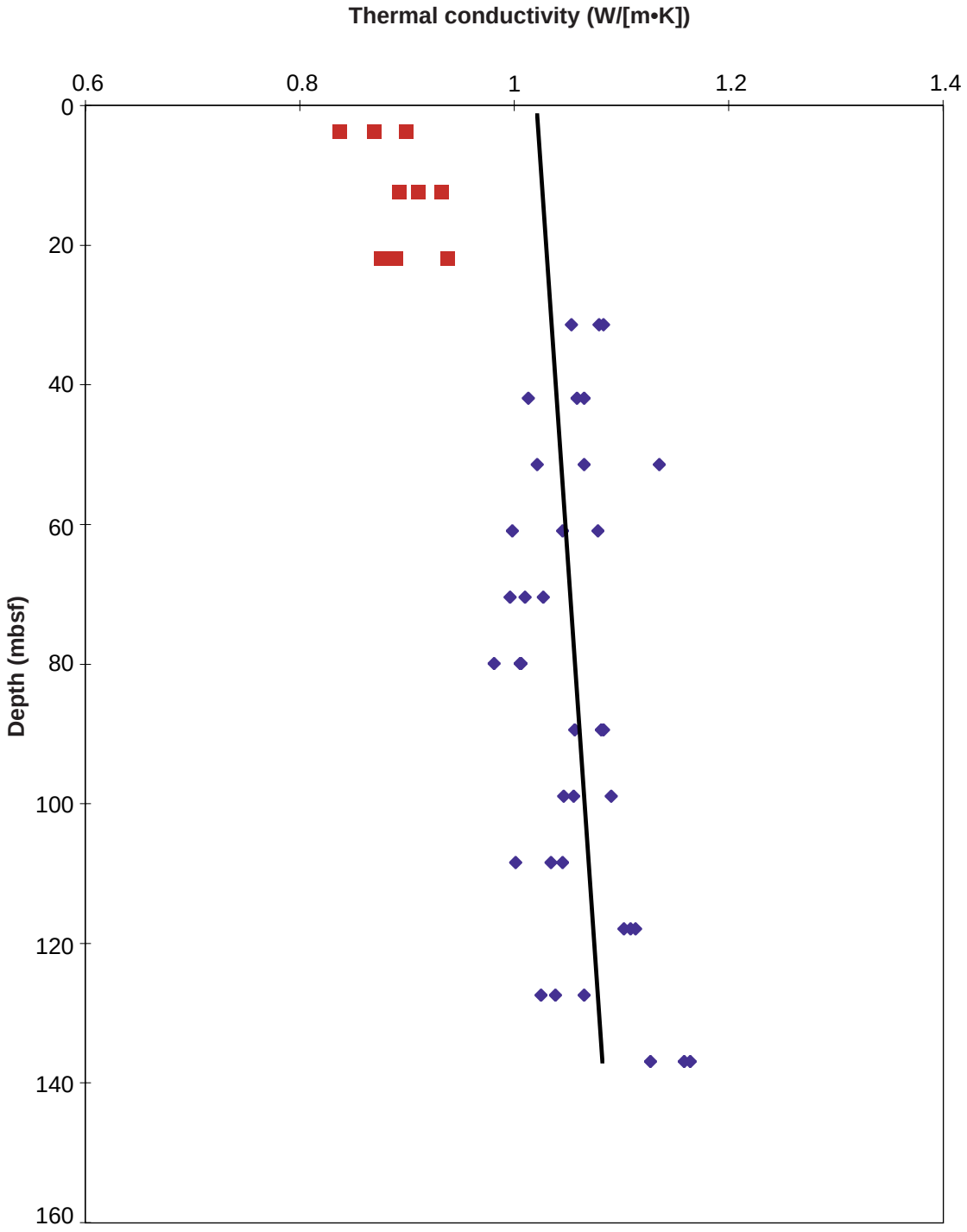

Figure F33. Downhole temperature measurements at Site 1101. The straight line is the best fit to all temperatures except that taken at the seafloor.

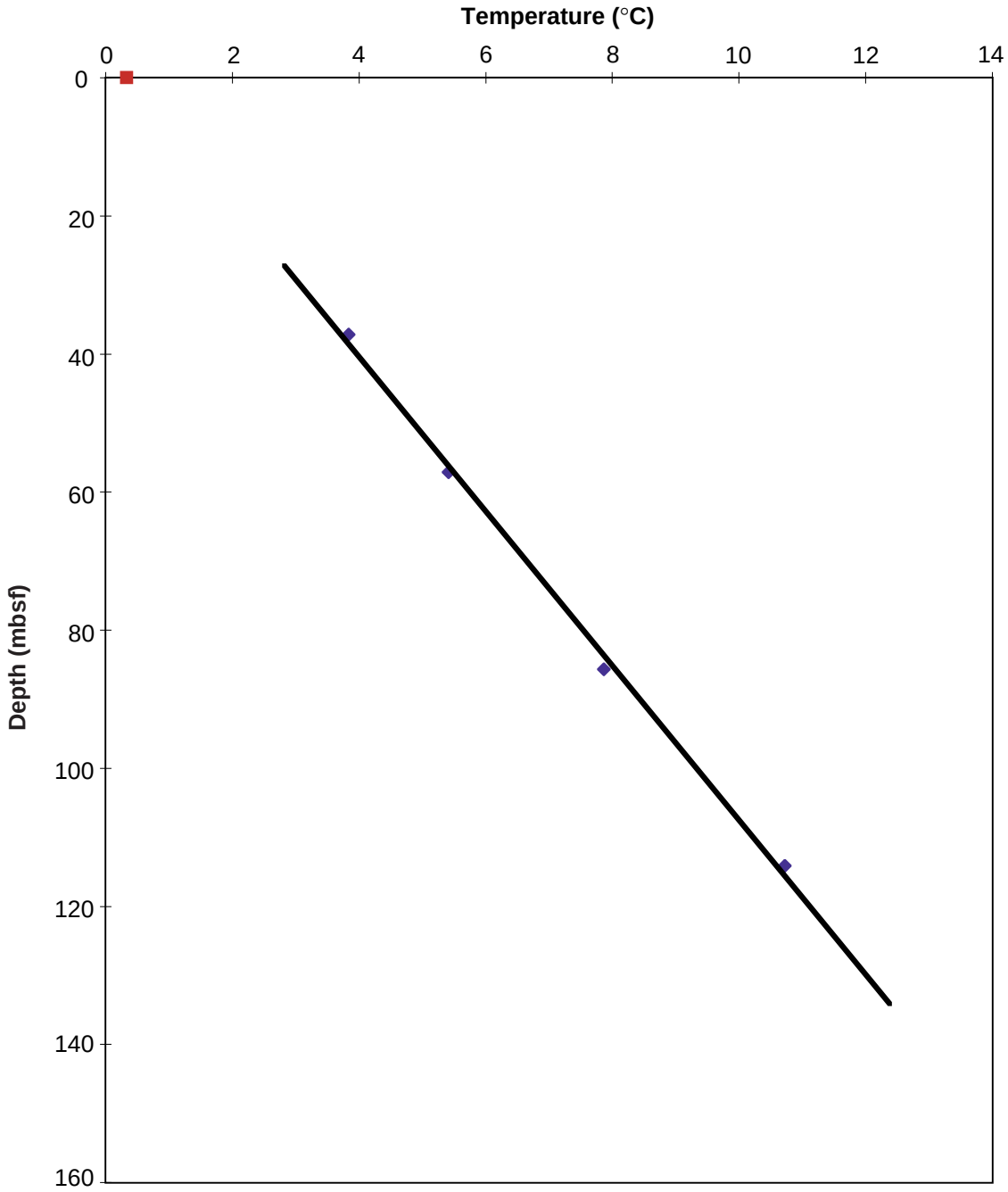

Figure F34. Depth-age profile determined from geomagnetic reversals and diatom and calcareous nannofossil datums. Diatom and calcareous nannofossil datum intervals are marked with bars indicating the distance between the samples used to define the interval. In labels showing species identity, B = base (first occurrence), T = top (last occurrence).

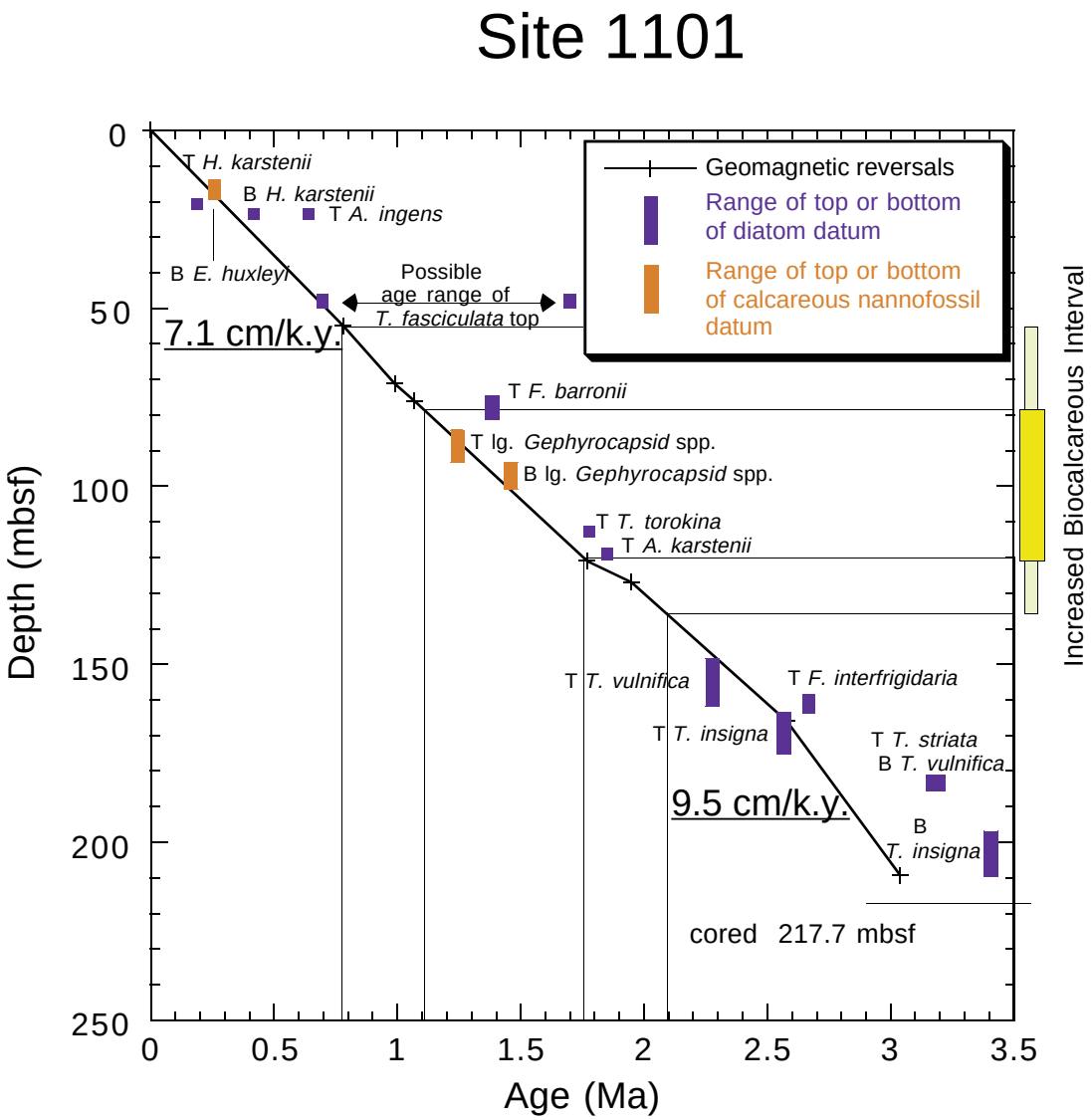

Figure F35. A. Sedimentation rate (cm/k.y.) vs. depth (mbsf). **B.** Sedimentation rate (cm/k.y.) vs. age (Ma). In both figures, the thick solid line represents paleomagnetic data, the thin solid line represents diatom datums, and the broken line represents calcareous nannofossil datums.

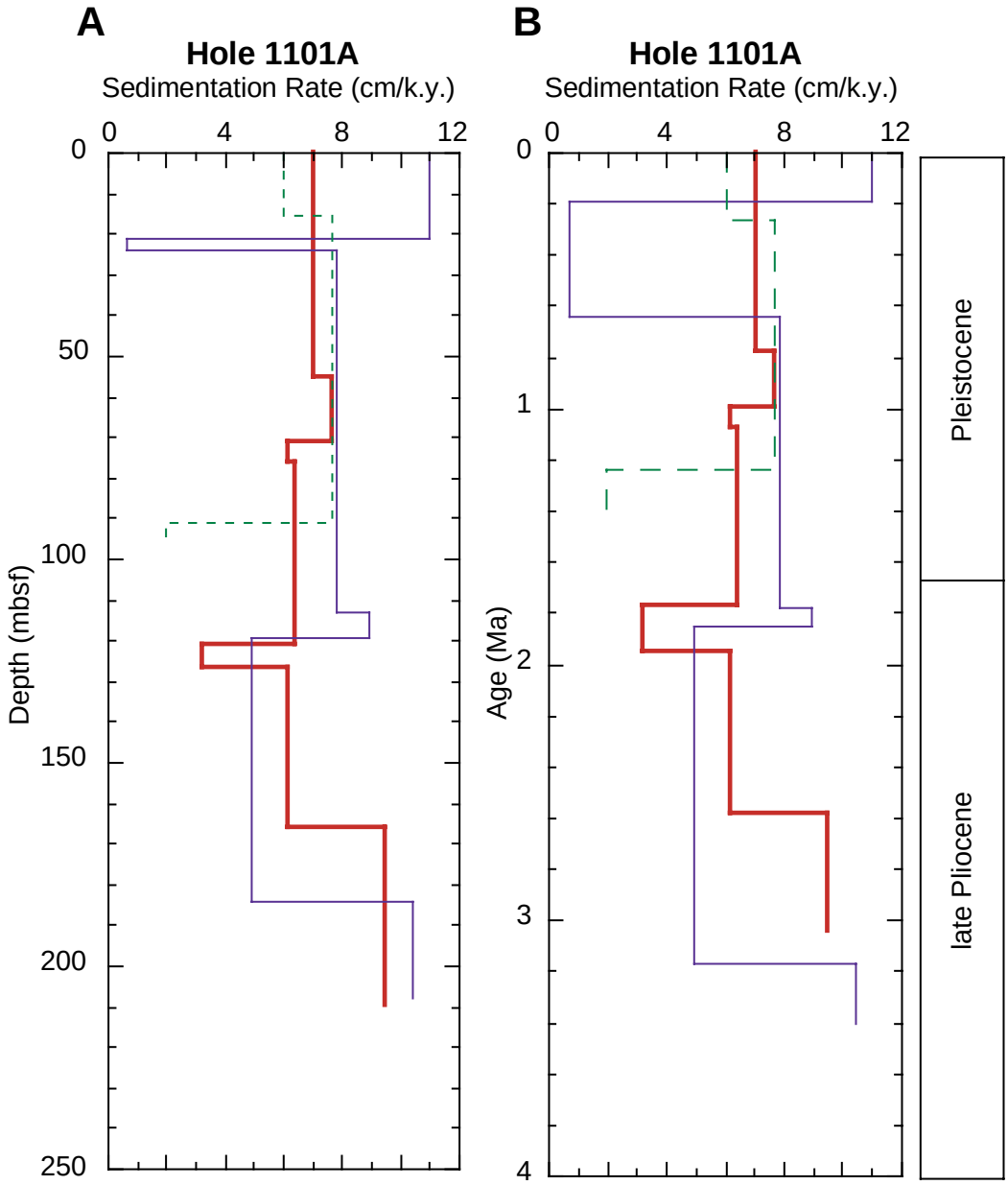

Figure F36. Uninterpreted (**A**) and interpreted (**B**) multichannel seismic profile IT92AW-114 across Drift 4, showing location and drilled depth at Site 1101. S.P. = shotpoint.

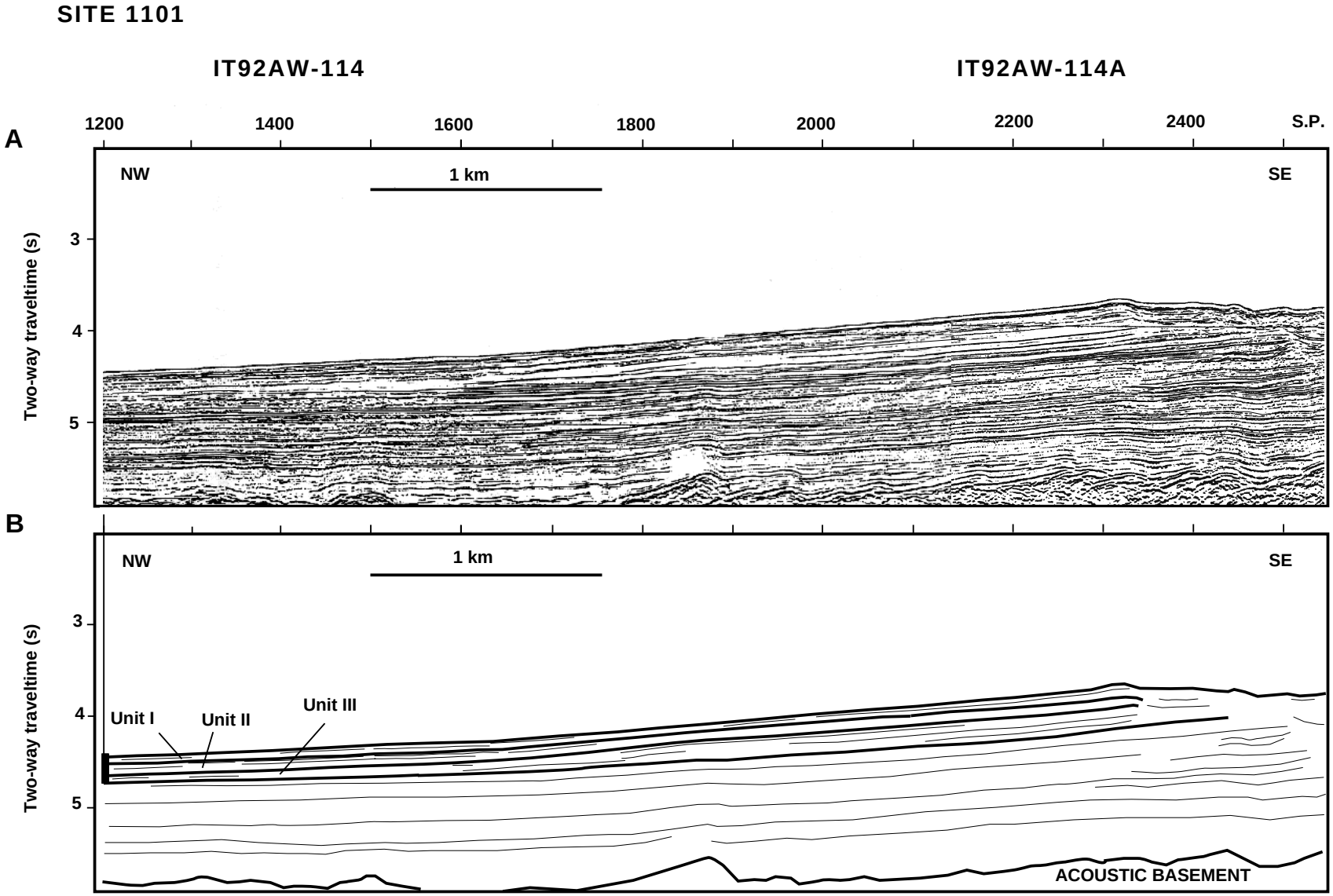

Figure F37. Time-depth model for Site 1101, based on linear fit to PWS3 (Hamilton Frame) velocity measurements (Fig. F31, p. 56).

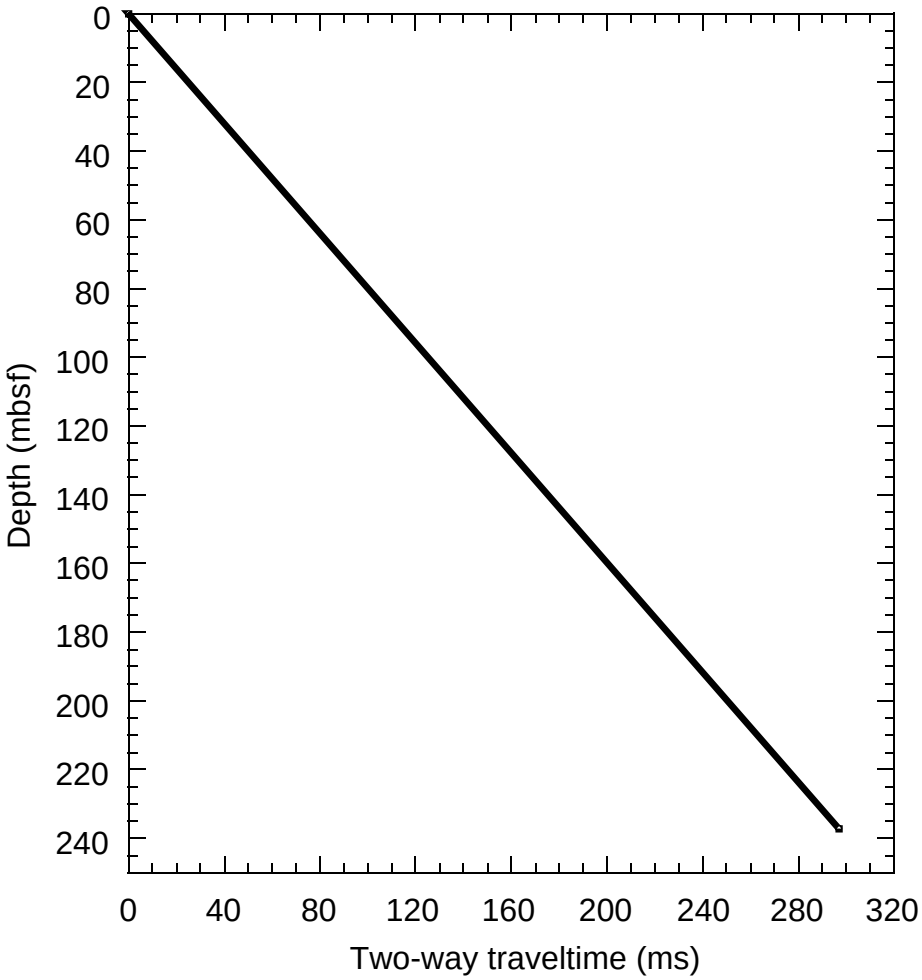

Figure F38. Seismic section over Site 1101 showing depths to major seismic and lithostratigraphic units and ages of seismic units. S.P. = shotpoint.

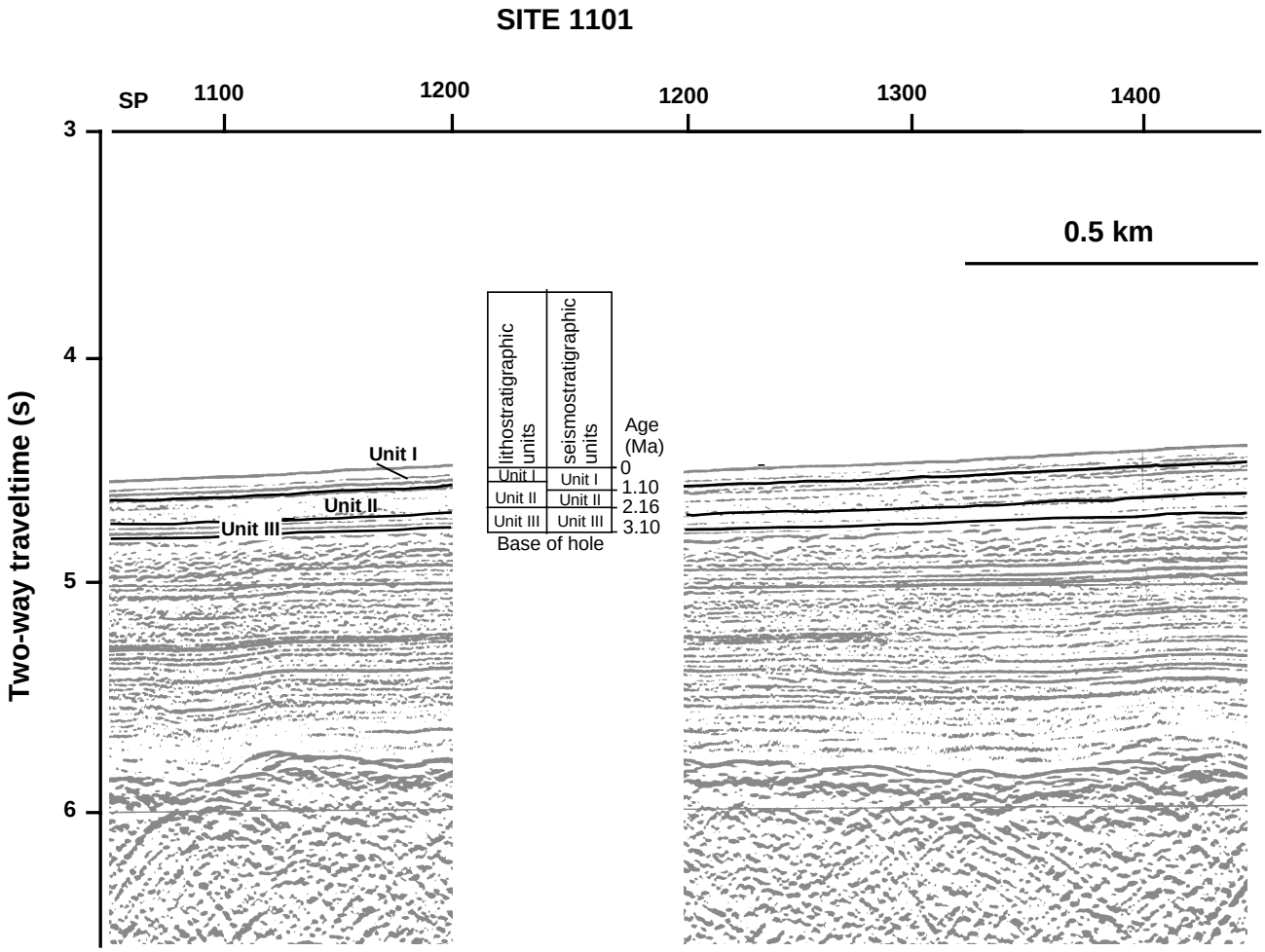

Table T1. Site 1101 coring summary.

Core	Date (March 1998)	Time (UTC)	Depth (mbsf)	Length cored (m)	Length recovered (m)	Recovery (%)
178-1101A-						
1H	18	1835	0.0-8.7	8.7	8.65	99.4
2H	18	2000	8.7-18.2	9.5	9.83	103.5
3H	18	2050	18.2-27.7	9.5	9.68	101.9
4H	18	2155	27.7-37.2	9.5	10.33	108.7
5H	18	2245	37.2-38.2	1.0	0.67	67.0
6H	19	0005	38.2-47.7	9.5	10.08	106.1
7H	19	0120	47.7-57.2	9.5	9.82	103.4
8H	19	0220	57.2-66.7	9.5	9.55	100.5
9H	19	0305	66.7-76.2	9.5	9.40	98.9
10H	19	0405	76.2-85.7	9.5	8.86	93.3
11H	19	0500	85.7-95.2	9.5	8.52	89.7
12H	19	0550	95.2-104.7	9.5	9.59	100.9
13H	19	0650	104.7-114.2	9.5	9.24	97.3
14H	19	0740	114.2-123.7	9.5	9.83	103.5
15H	19	0830	123.7-133.2	9.5	9.75	102.6
16H	19	0920	133.2-142.7	9.5	7.53	79.3
17X	19	1130	142.7-150.5	7.8	9.68	124.1
18X	19	1305	150.5-160.1	9.6	9.62	100.2
19X	19	1400	160.1-169.7	9.6	6.68	69.6
20X	19	1515	169.7-179.3	9.6	9.66	100.6
21X	19	1620	179.3-188.9	9.6	9.65	100.5
22X	19	1715	188.9-198.5	9.6	9.60	100.0
23X	19	1815	198.5-208.1	9.6	9.73	101.4
24X	19	1940	208.1-217.7	9.6	9.80	102.1
Coring totals:				217.7	215.75	99.1

Notes: UTC = Universal Time Coordinated. An expanded version of this coring summary table that includes lengths and depths of sections and comments on sampling is included in ASCII format in the **TABLES** directory.

Table T2. Relative intensities of selected X-ray diffraction peaks and percent $CaCO_3$ from bulk mineral samples of Site 1101 sediments.

Core, section, interval (cm)	Depth (mbsf)	Chlorite (7 Å)	Quartz (3.34 Å)	Plagioclase (3.19 Å)	Calcite (3.03 Å)	Calcite (wt%)
178-1101A-						
10H-2, 14-16	77.84	8	100	42	—	0.8
10H-2, 86-88	78.56	9	100	35	—	1.0
10H-3, 40-42	79.60	8	100	43	8	1.8
10H-3, 86-88	80.06	11	100	56	41	8.6
10H-3, 118-120	80.38	14	100	48	96	22.5
10H-3, 141-143	80.61	11	84	44	100	23.0
10H-4, 15-17	80.85	9	100	59	62	12.1
10H-4, 40-42	81.10	6	100	38	6	1.1
10H-4, 64-66	81.34	8	100	41	—	0.5
10H-4, 77-79	81.47	4	100	26	—	0.8
10H-4, 101-103	81.71	6	100	36	—	0.4
10H-4, 129-131	81.99	10	100	42	—	0.7
17X-2, 60-62	144.80	8	100	41	—	0.4
17X-4, 60-62	147.80	11	100	43	—	0.7
20X-5, 138-140	176.98	11	100	43	—	0.4
20X-6, 138-140	178.58	13	100	58	—	0.4

Note: Highest selected peak intensity is normalized to 100. — = mineral not detected.

Table T3. Diatom datums observed at Site 1101.

Diatom events	Age (Ma) A	Age (Ma) B	Age (Ma) C	Hole 1101A	Top depth (mbsf)	Bottom depth (mbsf)
		BKSA95	BKSA95			
TC *Hemidiscus karstenii*			**0.19**	<3H-2, 110		20.80
BC *Hemidiscus karstenii*			0.42	>3H-4, 110	23.80	
T *Actinocyclus ingens*	**0.64**	**0.64**	**0.65**	<3H-4, 110		23.80
T *Thalassiosira fasciculata*	1.7	0.7		6H-CC, 7H-1, 75	47.70	48.60
T *Fragilariopsis barronii*	**1.39**	**1.4**	**1.3**	>9H-CC, <10H-3, 30	76.05	79.50
T *Thalassiosira torokina*	1.85	1.8		<14H-4, 44		119.14
T *Thalassiosira kolbei*	1.85	2	2			
T *Actinocyclus karstenii*	1.78–2.9			<13H-6, 68		112.88
T *Thalassiosira vulnifica*	**2.28**	**2.5**	**2.3**	17X-CC, <18X-CC	150.50	160.12
T *Thalassiosira insigna*	**2.57**	**2.63**	**2.6**	19X-3, 70, <20X-3, 70	165.30	173.40
T *Fragilariopsis interfrigidaria*	2.67	2.63		18X-CC, 19X-2, 70	160.12	162.30
T *Thalassiosira striata*	2.92–3.4			>21X-3, 58, <21X-4, 40	182.88	184.20
B *Thalassiosira vulnifica*	**3.17**	**3.26**		>21X-3, 58, <21X-4, 40	182.88	184.20
B *Thalassiosira insigna*	3.4	3.4		>23X-1, 29, <23X-CC	198.79	208.23
				Base of hole = 217.7 mbsf		

Notes: Species listed in bold print are zonal boundary markers. Three age columns are shown: (A) Harwood and Maruyama (1992); (B) Gersonde, Hodell, Blum, et al. (1999, Leg 177); and (C) Gersonde and Bárcena (1998). The chrons were assigned by Harwood and Maruyama (1992). T = top/last occurrence datum, B = base/first occurrence datum, BC = base common/first common occurrence datum, TC = top common/last common occurrence datum.

Table T4. Split-core paleomagnetic measurements for Hole 1101A before demagnetization (NRM results).

Leg	Site	Hole	Core	Type	Section	Interval (cm)	Depth (mbsf)	Inclination (°)	Declination (°)	Intensity (A/m)	Demagnetization step (mT)	Run #
178	1101	A	1	H	1	10	0.1	–27.59	50.19	4.48E-02	0	12230
178	1101	A	1	H	1	15	0.15	–32.6	60.3	3.00E-02	0	12230
178	1101	A	1	H	1	20	0.2	–16.79	56.7	2.52E-02	0	12230
178	1101	A	1	H	1	25	0.25	6.43	38.38	2.54E-02	0	12230
178	1101	A	1	H	1	30	0.3	16.85	40.59	3.40E-02	0	12230
178	1101	A	1	H	1	35	0.35	15.95	37.6	3.55E-02	0	12230
178	1101	A	1	H	1	40	0.4	0.04	56.81	2.67E-02	0	12230
178	1101	A	1	H	1	45	0.45	–26.23	49.42	3.94E-02	0	12230
178	1101	A	1	H	1	50	0.5	–44.39	55.02	5.04E-02	0	12230
178	1101	A	1	H	1	55	0.55	–61.75	45.3	5.02E-02	0	12230
178	1101	A	1	H	1	60	0.6	–34.55	56.46	7.31E-02	0	12230
178	1101	A	1	H	1	65	0.65	–27.38	63.05	8.06E-02	0	12230
178	1101	A	1	H	1	70	0.7	–60.76	66.86	7.06E-02	0	12230
178	1101	A	1	H	1	75	0.75	–82.72	88.96	9.75E-02	0	12230
178	1101	A	1	H	1	80	0.8	–73.57	78.73	1.14E-01	0	12230
178	1101	A	1	H	1	85	0.85	–61.99	66.43	1.09E-01	0	12230
178	1101	A	1	H	1	90	0.9	–69.28	48.51	1.04E-01	0	12230
178	1101	A	1	H	1	95	0.95	–71.51	31.69	9.67E-02	0	12230
178	1101	A	1	H	1	100	1	–56.32	32.04	8.92E-02	0	12230
178	1101	A	1	H	1	105	1.05	–34.63	33.71	6.56E-02	0	12230
178	1101	A	1	H	1	110	1.1	–49.58	28.89	3.04E-02	0	12230
178	1101	A	1	H	1	115	1.15	–60.57	35.69	4.11E-02	0	12230
178	1101	A	1	H	1	120	1.2	–38.01	32.57	5.63E-02	0	12230
178	1101	A	1	H	1	125	1.25	–16.7	37.08	6.42E-02	0	12230
178	1101	A	1	H	1	130	1.3	–3.46	40.2	6.95E-02	0	12230
178	1101	A	1	H	1	135	1.35	20.99	52.06	7.42E-02	0	12230
178	1101	A	1	H	1	140	1.4	12.12	59.59	6.42E-02	0	12230
178	1101	A	1	H	2	10	1.6	–32.79	27.29	9.06E-02	0	12234
178	1101	A	1	H	2	15	1.65	–21.52	29.2	1.01E-01	0	12234
178	1101	A	1	H	2	20	1.7	23.85	23.93	1.32E-01	0	12234
178	1101	A	1	H	2	25	1.75	68.48	32.19	1.82E-01	0	12234
178	1101	A	1	H	2	30	1.8	76.65	82.67	2.42E-01	0	12234
178	1101	A	1	H	2	35	1.85	76.61	86.77	2.41E-01	0	12234
178	1101	A	1	H	2	40	1.9	81.35	155.67	1.96E-01	0	12234
178	1101	A	1	H	2	45	1.95	84.43	193.32	1.75E-01	0	12234
178	1101	A	1	H	2	50	2	84.97	176.69	1.67E-01	0	12234
178	1101	A	1	H	2	55	2.05	83.73	148.8	1.49E-01	0	12234
178	1101	A	1	H	2	60	2.1	87.14	123.49	1.85E-01	0	12234
178	1101	A	1	H	2	65	2.15	84.74	15.29	2.65E-01	0	12234
178	1101	A	1	H	2	70	2.2	80.94	354.52	2.86E-01	0	12234
178	1101	A	1	H	2	75	2.25	79.54	299.12	2.04E-01	0	12234
178	1101	A	1	H	2	80	2.3	87.05	346.74	9.06E-02	0	12234
178	1101	A	1	H	2	85	2.35	56.56	29.42	9.96E-02	0	12234
178	1101	A	1	H	2	90	2.4	65.04	9.2	1.09E-01	0	12234
178	1101	A	1	H	2	95	2.45	54.24	150.67	7.08E-02	0	12234
178	1101	A	1	H	2	100	2.5	15.83	131.07	3.95E-02	0	12234
178	1101	A	1	H	2	105	2.55	20.17	53.24	4.11E-02	0	12234
178	1101	A	1	H	2	110	2.6	29.02	51.89	7.04E-02	0	12234
178	1101	A	1	H	2	115	2.65	37.66	65.99	9.07E-02	0	12234
178	1101	A	1	H	2	120	2.7	50.98	45.97	9.02E-02	0	12234
178	1101	A	1	H	2	125	2.75	61.96	31.65	9.98E-02	0	12234
178	1101	A	1	H	2	130	2.8	56.29	49.88	1.18E-01	0	12234
178	1101	A	1	H	3	10	3.1	41.7	6.51	8.16E-02	0	12238
178	1101	A	1	H	3	15	3.15	36.69	12.35	8.77E-02	0	12238
178	1101	A	1	H	3	20	3.2	36.96	14.23	9.36E-02	0	12238
178	1101	A	1	H	3	25	3.25	37.94	7.57	9.10E-02	0	12238
178	1101	A	1	H	3	30	3.3	34.85	19.11	7.62E-02	0	12238
178	1101	A	1	H	3	35	3.35	14.54	27.22	6.30E-02	0	12238
178	1101	A	1	H	3	40	3.4	–13.48	31.86	5.85E-02	0	12238
178	1101	A	1	H	3	45	3.45	–20.43	24.9	8.42E-02	0	12238
178	1101	A	1	H	3	50	3.5	–19.67	21.8	8.11E-02	0	12238
178	1101	A	1	H	3	55	3.55	–14.34	20.94	8.99E-02	0	12238
178	1101	A	1	H	3	60	3.6	–14.65	28.99	1.02E-01	0	12238
178	1101	A	1	H	3	65	3.65	–3.96	23.91	9.01E-02	0	12238
178	1101	A	1	H	3	70	3.7	17.52	23.12	5.37E-02	0	12238

Note: Only a portion of this table appears here. The complete table is available in ASCII format in the **TABLES** directory.

Table T5. Split-core paleomagnetic measurements for Hole 1101A after 10-mT demagnetization.

Leg	Site	Hole	Core	Type	Section	Interval (cm)	Depth (mbsf)	Inclination (°)	Declination (°)	Intensity (A/m)	Demagnetization step (mT)	Run #
178	1101	A	1	H	1	10	0.1	–69.55	64.52	7.88E-02	10	12231
178	1101	A	1	H	1	15	0.15	–78.2	83.92	7.95E-02	10	12231
178	1101	A	1	H	1	20	0.2	–80.42	81.11	7.75E-02	10	12231
178	1101	A	1	H	1	25	0.25	–79.16	50.4	7.29E-02	10	12231
178	1101	A	1	H	1	30	0.3	–74.77	48.06	7.29E-02	10	12231
178	1101	A	1	H	1	35	0.35	–74.52	52.44	7.65E-02	10	12231
178	1101	A	1	H	1	40	0.4	–79.78	70.95	8.08E-02	10	12231
178	1101	A	1	H	1	45	0.45	–76.33	55.58	8.78E-02	10	12231
178	1101	A	1	H	1	50	0.5	–72.1	51.53	9.61E-02	10	12231
178	1101	A	1	H	1	55	0.55	–70.75	83.24	1.08E-01	10	12231
178	1101	A	1	H	1	60	0.6	–70.25	80.5	1.16E-01	10	12231
178	1101	A	1	H	1	65	0.65	–68.81	71.82	1.17E-01	10	12231
178	1101	A	1	H	1	70	0.7	–78.03	89.25	1.25E-01	10	12231
178	1101	A	1	H	1	75	0.75	–84.1	155.06	1.51E-01	10	12231
178	1101	A	1	H	1	80	0.8	–81.84	128.89	1.60E-01	10	12231
178	1101	A	1	H	1	85	0.85	–78.54	99.05	1.51E-01	10	12231
178	1101	A	1	H	1	90	0.9	–85.29	83.71	1.48E-01	10	12231
178	1101	A	1	H	1	95	0.95	–86.24	42.47	1.39E-01	10	12231
178	1101	A	1	H	1	100	1	–79.66	40.73	1.28E-01	10	12231
178	1101	A	1	H	1	105	1.05	–73.88	37.84	9.94E-02	10	12231
178	1101	A	1	H	1	110	1.1	–86.18	9.42	7.83E-02	10	12231
178	1101	A	1	H	1	115	1.15	–88.23	35.36	8.50E-02	10	12231
178	1101	A	1	H	1	120	1.2	–71.38	30.89	8.45E-02	10	12231
178	1101	A	1	H	1	125	1.25	–57.36	41.33	7.51E-02	10	12231
178	1101	A	1	H	1	130	1.3	–53.5	45.07	7.36E-02	10	12231
178	1101	A	1	H	1	135	1.35	–54.43	65.57	5.48E-02	10	12231
178	1101	A	1	H	1	140	1.4	–54.47	83.74	7.60E-02	10	12231
178	1101	A	1	H	2	10	1.6	–60.66	24.51	1.25E-01	10	12235
178	1101	A	1	H	2	15	1.65	–59.95	28.51	1.33E-01	10	12235
178	1101	A	1	H	2	20	1.7	–36.21	26.62	1.01E-01	10	12235
178	1101	A	1	H	2	25	1.75	40.96	48.48	4.58E-02	10	12235
178	1101	A	1	H	2	30	1.8	62.27	122.44	8.11E-02	10	12235
178	1101	A	1	H	2	35	1.85	54.19	114.06	8.46E-02	10	12235
178	1101	A	1	H	2	40	1.9	44.26	161.29	6.30E-02	10	12235
178	1101	A	1	H	2	45	1.95	44.9	205.09	5.05E-02	10	12235
178	1101	A	1	H	2	50	2	46.7	189.92	4.25E-02	10	12235
178	1101	A	1	H	2	55	2.05	22.77	146.1	3.01E-02	10	12235
178	1101	A	1	H	2	60	2.1	25.6	181.19	5.81E-02	10	12235
178	1101	A	1	H	2	65	2.15	30.25	217.48	8.22E-02	10	12235
178	1101	A	1	H	2	70	2.2	30.38	255.4	7.01E-02	10	12235
178	1101	A	1	H	2	75	2.25	18.51	278.51	2.69E-02	10	12235
178	1101	A	1	H	2	80	2.3	–28.32	66.49	1.83E-02	10	12235
178	1101	A	1	H	2	85	2.35	15.73	33.88	3.86E-02	10	12235
178	1101	A	1	H	2	90	2.4	14.55	358.59	2.10E-02	10	12235
178	1101	A	1	H	2	95	2.45	–41.76	159.2	4.96E-02	10	12235
178	1101	A	1	H	2	100	2.5	–58.23	147.35	7.21E-02	10	12235
178	1101	A	1	H	2	105	2.55	–73.7	86.1	7.02E-02	10	12235
178	1101	A	1	H	2	110	2.6	–65.29	74.71	7.87E-02	10	12235
178	1101	A	1	H	2	115	2.65	–52.97	82.19	8.77E-02	10	12235
178	1101	A	1	H	2	120	2.7	–60.14	71.51	7.64E-02	10	12235
178	1101	A	1	H	2	125	2.75	–68.18	65	6.35E-02	10	12235
178	1101	A	1	H	2	130	2.8	–56.24	78.93	7.20E-02	10	12235
178	1101	A	1	H	3	10	3.1	–44.28	16.33	6.18E-02	10	12239
178	1101	A	1	H	3	15	3.15	–38.21	19.28	6.88E-02	10	12239
178	1101	A	1	H	3	20	3.2	–38.49	22.32	6.80E-02	10	12239
178	1101	A	1	H	3	25	3.25	–52.09	20.64	7.13E-02	10	12239
178	1101	A	1	H	3	30	3.3	–50.11	27.15	8.24E-02	10	12239
178	1101	A	1	H	3	35	3.35	–55.02	31.99	9.14E-02	10	12239
178	1101	A	1	H	3	40	3.4	–64.6	42.43	1.06E-01	10	12239
178	1101	A	1	H	3	45	3.45	–63.5	37.7	1.33E-01	10	12239
178	1101	A	1	H	3	50	3.5	–65.42	34.52	1.38E-01	10	12239
178	1101	A	1	H	3	55	3.55	–61.78	30.06	1.43E-01	10	12239
178	1101	A	1	H	3	60	3.6	–60.35	35.48	1.50E-01	10	12239
178	1101	A	1	H	3	65	3.65	–61.34	28.82	1.31E-01	10	12239
178	1101	A	1	H	3	70	3.7	–67.67	29.89	9.26E-02	10	12239

Note: Only a portion of this table appears here. The complete table is available in ASCII format in the **TABLES** directory.

Table T6. Split-core paleomagnetic measurements for Hole 1101A after 20-mT demagnetization.

Leg	Site	Hole	Core	Type	Section	Interval (cm)	Depth (mbsf)	Inclination (°)	Declination (°)	Intensity (A/m)	Demagnetization step (mT)	Run #
178	1101	A	1	H	1	10	0.1	–71.71	66.66	6.65E-02	20	12232
178	1101	A	1	H	1	15	0.15	–79.47	85.46	6.86E-02	20	12232
178	1101	A	1	H	1	20	0.2	–82.15	82.48	6.78E-02	20	12232
178	1101	A	1	H	1	25	0.25	–80.73	48.5	6.47E-02	20	12232
178	1101	A	1	H	1	30	0.3	–76.66	45.74	6.55E-02	20	12232
178	1101	A	1	H	1	35	0.35	–76.62	50.27	6.89E-02	20	12232
178	1101	A	1	H	1	40	0.4	–82.05	73.02	7.35E-02	20	12232
178	1101	A	1	H	1	45	0.45	–78.99	55.01	8.06E-02	20	12232
178	1101	A	1	H	1	50	0.5	–74.15	50.51	8.91E-02	20	12232
178	1101	A	1	H	1	55	0.55	–71.13	84.93	1.01E-01	20	12232
178	1101	A	1	H	1	60	0.6	–71.86	84.14	1.07E-01	20	12232
178	1101	A	1	H	1	65	0.65	–72.39	77.29	1.06E-01	20	12232
178	1101	A	1	H	1	70	0.7	–79.76	104.27	1.16E-01	20	12232
178	1101	A	1	H	1	75	0.75	–83.83	163.46	1.41E-01	20	12232
178	1101	A	1	H	1	80	0.8	–81.95	144.1	1.49E-01	20	12232
178	1101	A	1	H	1	85	0.85	–80.49	113.53	1.40E-01	20	12232
178	1101	A	1	H	1	90	0.9	–87.27	128.82	1.38E-01	20	12232
178	1101	A	1	H	1	95	0.95	–89.15	30.52	1.29E-01	20	12232
178	1101	A	1	H	1	100	1	–83.35	39.24	1.18E-01	20	12232
178	1101	A	1	H	1	105	1.05	–78.44	34.56	9.13E-02	20	12232
178	1101	A	1	H	1	110	1.1	–87.05	304.83	7.31E-02	20	12232
178	1101	A	1	H	1	115	1.15	–87.71	261.05	7.88E-02	20	12232
178	1101	A	1	H	1	120	1.2	–74.98	22.36	7.66E-02	20	12232
178	1101	A	1	H	1	125	1.25	–61.95	38.19	6.61E-02	20	12232
178	1101	A	1	H	1	130	1.3	–58.09	42.67	6.47E-02	20	12232
178	1101	A	1	H	1	135	1.35	–62.61	66.98	4.84E-02	20	12232
178	1101	A	1	H	1	140	1.4	–61.1	92.47	6.88E-02	20	12232
178	1101	A	1	H	2	10	1.6	–62.53	21.64	1.16E-01	20	12236
178	1101	A	1	H	2	15	1.65	–62.59	24.35	1.20E-01	20	12236
178	1101	A	1	H	2	20	1.7	–41.59	23.22	8.29E-02	20	12236
178	1101	A	1	H	2	25	1.75	37.95	47.37	2.94E-02	20	12236
178	1101	A	1	H	2	30	1.8	61.86	131.29	5.79E-02	20	12236
178	1101	A	1	H	2	35	1.85	53.57	118.68	6.10E-02	20	12236
178	1101	A	1	H	2	40	1.9	40.79	164.88	4.75E-02	20	12236
178	1101	A	1	H	2	45	1.95	39.59	208.24	3.86E-02	20	12236
178	1101	A	1	H	2	50	2	41.11	193.34	3.08E-02	20	12236
178	1101	A	1	H	2	55	2.05	14.72	149.55	2.21E-02	20	12236
178	1101	A	1	H	2	60	2.1	18.29	182.62	4.56E-02	20	12236
178	1101	A	1	H	2	65	2.15	21.73	216.67	6.26E-02	20	12236
178	1101	A	1	H	2	70	2.2	18.58	253.82	5.32E-02	20	12236
178	1101	A	1	H	2	75	2.25	–3.46	275.17	2.20E-02	20	12236
178	1101	A	1	H	2	80	2.3	–41.69	68.56	1.65E-02	20	12236
178	1101	A	1	H	2	85	2.35	15.57	30.69	3.25E-02	20	12236
178	1101	A	1	H	2	90	2.4	12.57	348.66	1.68E-02	20	12236
178	1101	A	1	H	2	95	2.45	–42.59	164.83	4.82E-02	20	12236
178	1101	A	1	H	2	100	2.5	–58.78	151.49	6.83E-02	20	12236
178	1101	A	1	H	2	105	2.55	–76.21	94.74	6.45E-02	20	12236
178	1101	A	1	H	2	110	2.6	–69.05	78.16	6.96E-02	20	12236
178	1101	A	1	H	2	115	2.65	–57.41	84.13	7.49E-02	20	12236
178	1101	A	1	H	2	120	2.7	–64.82	72.81	6.56E-02	20	12236
178	1101	A	1	H	2	125	2.75	–72.83	67.41	5.51E-02	20	12236
178	1101	A	1	H	2	130	2.8	–61.21	81.56	6.02E-02	20	12236
178	1101	A	1	H	3	10	3.1	–49.6	18.35	5.18E-02	20	12240
178	1101	A	1	H	3	15	3.15	–42.88	21.01	5.85E-02	20	12240
178	1101	A	1	H	3	20	3.2	–43.35	24.35	5.88E-02	20	12240
178	1101	A	1	H	3	25	3.25	–56.94	24.02	6.29E-02	20	12240
178	1101	A	1	H	3	30	3.3	–53.64	28.82	7.24E-02	20	12240
178	1101	A	1	H	3	35	3.35	–57.09	32.4	8.11E-02	20	12240
178	1101	A	1	H	3	40	3.4	–65.54	43.23	9.35E-02	20	12240
178	1101	A	1	H	3	45	3.45	–64.23	38.7	1.15E-01	20	12240
178	1101	A	1	H	3	50	3.5	–66.3	35.53	1.18E-01	20	12240
178	1101	A	1	H	3	55	3.55	–62.69	30.55	1.21E-01	20	12240
178	1101	A	1	H	3	60	3.6	–61.58	35.49	1.25E-01	20	12240
178	1101	A	1	H	3	65	3.65	–62.8	28.78	1.10E-01	20	12240
178	1101	A	1	H	3	70	3.7	–68.89	28.96	7.97E-02	20	12240

Note: Only a portion of this table appears here. The complete table is available in ASCII format in the **TABLES** directory.

Table T7. Split-core paleomagnetic measurements for Hole 1101A after 30-mT demagnetization.

Leg	Site	Hole	Core	Type	Section	Interval (cm)	Depth (mbsf)	Inclination (°)	Declination (°)	Intensity (A/m)	Demagnetization step (mT)	Run #
178	1101	A	1	H	1	10	0.1	–73.13	68.62	5.37E-02	30	12233
178	1101	A	1	H	1	15	0.15	–79.95	87.08	5.66E-02	30	12233
178	1101	A	1	H	1	20	0.2	–82.73	82.95	5.67E-02	30	12233
178	1101	A	1	H	1	25	0.25	–81.38	48.03	5.50E-02	30	12233
178	1101	A	1	H	1	30	0.3	–77.38	45.33	5.67E-02	30	12233
178	1101	A	1	H	1	35	0.35	–77.38	49.59	6.01E-02	30	12233
178	1101	A	1	H	1	40	0.4	–82.87	73.43	6.47E-02	30	12233
178	1101	A	1	H	1	45	0.45	–80.3	55.26	7.21E-02	30	12233
178	1101	A	1	H	1	50	0.5	–75.26	51.85	8.09E-02	30	12233
178	1101	A	1	H	1	55	0.55	–71.62	85.48	9.21E-02	30	12233
178	1101	A	1	H	1	60	0.6	–72.6	84.44	9.74E-02	30	12233
178	1101	A	1	H	1	65	0.65	–74.01	80.68	9.53E-02	30	12233
178	1101	A	1	H	1	70	0.7	–80.62	111.59	1.05E-01	30	12233
178	1101	A	1	H	1	75	0.75	–83.76	164.42	1.27E-01	30	12233
178	1101	A	1	H	1	80	0.8	–81.78	149.96	1.34E-01	30	12233
178	1101	A	1	H	1	85	0.85	–81.36	122.79	1.26E-01	30	12233
178	1101	A	1	H	1	90	0.9	–87.06	163.07	1.24E-01	30	12233
178	1101	A	1	H	1	95	0.95	–89.28	241.68	1.17E-01	30	12233
178	1101	A	1	H	1	100	1	–85.4	36.88	1.06E-01	30	12233
178	1101	A	1	H	1	105	1.05	–80.91	29.85	8.23E-02	30	12233
178	1101	A	1	H	1	110	1.1	–85.97	282.36	6.65E-02	30	12233
178	1101	A	1	H	1	115	1.15	–85.8	256.68	7.14E-02	30	12233
178	1101	A	1	H	1	120	1.2	–76.79	14.24	6.87E-02	30	12233
178	1101	A	1	H	1	125	1.25	–64.96	34.85	5.82E-02	30	12233
178	1101	A	1	H	1	130	1.3	–61.09	40.64	5.69E-02	30	12233
178	1101	A	1	H	1	135	1.35	–67.36	66.44	4.34E-02	30	12233
178	1101	A	1	H	1	140	1.4	–65.49	98.53	6.19E-02	30	12233
178	1101	A	1	H	2	10	1.6	–63.31	19.46	1.06E-01	30	12237
178	1101	A	1	H	2	15	1.65	–64.18	20.78	1.05E-01	30	12237
178	1101	A	1	H	2	20	1.7	–46.48	20.69	6.56E-02	30	12237
178	1101	A	1	H	2	25	1.75	27.19	45.88	1.75E-02	30	12237
178	1101	A	1	H	2	30	1.8	60.54	133.3	3.70E-02	30	12237
178	1101	A	1	H	2	35	1.85	52.87	119.18	3.94E-02	30	12237
178	1101	A	1	H	2	40	1.9	37.79	165.07	3.14E-02	30	12237
178	1101	A	1	H	2	45	1.95	35.6	209.35	2.49E-02	30	12237
178	1101	A	1	H	2	50	2	37.52	195.48	1.86E-02	30	12237
178	1101	A	1	H	2	55	2.05	3.67	147.23	1.45E-02	30	12237
178	1101	A	1	H	2	60	2.1	13.56	179.93	2.89E-02	30	12237
178	1101	A	1	H	2	65	2.15	19.81	216.99	4.08E-02	30	12237
178	1101	A	1	H	2	70	2.2	15.25	256.4	3.71E-02	30	12237
178	1101	A	1	H	2	75	2.25	–11.25	276.61	1.79E-02	30	12237
178	1101	A	1	H	2	80	2.3	–51.02	68.18	1.53E-02	30	12237
178	1101	A	1	H	2	85	2.35	11.27	30.62	2.78E-02	30	12237
178	1101	A	1	H	2	90	2.4	4.27	347.45	1.49E-02	30	12237
178	1101	A	1	H	2	95	2.45	–44.31	166.14	4.51E-02	30	12237
178	1101	A	1	H	2	100	2.5	–59.2	151.61	6.34E-02	30	12237
178	1101	A	1	H	2	105	2.55	–76.38	96.19	5.78E-02	30	12237
178	1101	A	1	H	2	110	2.6	–70.68	77.63	5.83E-02	30	12237
178	1101	A	1	H	2	115	2.65	–60.55	83.59	5.93E-02	30	12237
178	1101	A	1	H	2	120	2.7	–67.32	71.78	5.19E-02	30	12237
178	1101	A	1	H	2	125	2.75	–74.73	65.73	4.41E-02	30	12237
178	1101	A	1	H	2	130	2.8	–64.24	81.42	4.67E-02	30	12237
178	1101	A	1	H	3	10	3.1	–53.71	21.17	4.02E-02	30	12241
178	1101	A	1	H	3	15	3.15	–46.94	23.67	4.61E-02	30	12241
178	1101	A	1	H	3	20	3.2	–47.35	26.79	4.79E-02	30	12241
178	1101	A	1	H	3	25	3.25	–59.41	26.37	5.23E-02	30	12241
178	1101	A	1	H	3	30	3.3	–55.89	29.69	5.99E-02	30	12241
178	1101	A	1	H	3	35	3.35	–58.46	33.01	6.79E-02	30	12241
178	1101	A	1	H	3	40	3.4	–65.55	43.44	7.79E-02	30	12241
178	1101	A	1	H	3	45	3.45	–64.2	39.13	9.30E-02	30	12241
178	1101	A	1	H	3	50	3.5	–66.64	35.56	9.20E-02	30	12241
178	1101	A	1	H	3	55	3.55	–63.12	30.56	9.30E-02	30	12241
178	1101	A	1	H	3	60	3.6	–62.28	34.5	9.44E-02	30	12241
178	1101	A	1	H	3	65	3.65	–63.95	27.77	8.31E-02	30	12241
178	1101	A	1	H	3	70	3.7	–69.42	26.36	6.28E-02	30	12241

Note: Only a portion of this table appears here. The complete table is available in ASCII format in the **TABLES** directory.

Table T8. Split-core paleomagnetic measurements for Hole 1101A after processing the results from the 30-mT demagnetization steps by removing measurements from drilling-disturbed intervals and measurements made within 10 cm of the ends of each core section.

Leg	Site	Hole	Core	Type	Section	Interval (cm)	Depth (mbsf)	Inclination (°)	Declination (°)	Intensity (A/m)	Demagnetization step (mT)	Run #
178	1101	A	1	H	1	25	0.25	–81.38	48.03	5.50E-02	30	1223
178	1101	A	1	H	1	30	0.3	–77.38	45.33	5.67E-02	30	1223
178	1101	A	1	H	1	35	0.35	–77.38	49.59	6.01E-02	30	1223
178	1101	A	1	H	1	40	0.4	–82.87	73.43	6.47E-02	30	1223
178	1101	A	1	H	1	45	0.45	–80.3	55.26	7.21E-02	30	1223
178	1101	A	1	H	1	50	0.5	–75.26	51.85	8.09E-02	30	1223
178	1101	A	1	H	1	55	0.55	–71.62	85.48	9.21E-02	30	1223
178	1101	A	1	H	1	60	0.6	–72.6	84.44	9.74E-02	30	1223
178	1101	A	1	H	1	65	0.65	–74.01	80.68	9.53E-02	30	1223
178	1101	A	1	H	1	70	0.7	–80.62	111.59	1.05E-01	30	1223
178	1101	A	1	H	1	75	0.75	–83.76	164.42	1.27E-01	30	1223
178	1101	A	1	H	1	80	0.8	–81.78	149.96	1.34E-01	30	1223
178	1101	A	1	H	1	85	0.85	–81.36	122.79	1.26E-01	30	1223
178	1101	A	1	H	1	90	0.9	–87.06	163.07	1.24E-01	30	1223
178	1101	A	1	H	1	95	0.95	–89.28	241.68	1.17E-01	30	1223
178	1101	A	1	H	1	100	1	–85.4	36.88	1.06E-01	30	1223
178	1101	A	1	H	1	105	1.05	–80.91	29.85	8.23E-02	30	1223
178	1101	A	1	H	1	110	1.1	–85.97	282.36	6.65E-02	30	1223
178	1101	A	1	H	1	115	1.15	–85.8	256.68	7.14E-02	30	1223
178	1101	A	1	H	1	120	1.2	–76.79	14.24	6.87E-02	30	1223
178	1101	A	1	H	1	125	1.25	–64.96	34.85	5.82E-02	30	1223
178	1101	A	1	H	1	130	1.3	–61.09	40.64	5.69E-02	30	1223
178	1101	A	1	H	1	135	1.35	–67.36	66.44	4.34E-02	30	1223
178	1101	A	1	H	1	140	1.4	–65.49	98.53	6.19E-02	30	1223
178	1101	A	1	H	2	10	1.6	–63.31	19.46	1.06E-01	30	1223
178	1101	A	1	H	2	15	1.65	–64.18	20.78	1.05E-01	30	1223
178	1101	A	1	H	2	20	1.7	–46.48	20.69	6.56E-02	30	1223
178	1101	A	1	H	2	25	1.75	27.19	45.88	1.75E-02	30	1223
178	1101	A	1	H	2	30	1.8	60.54	133.3	3.70E-02	30	1223
178	1101	A	1	H	2	35	1.85	52.87	119.18	3.94E-02	30	1223
178	1101	A	1	H	2	40	1.9	37.79	165.07	3.14E-02	30	1223
178	1101	A	1	H	2	45	1.95	35.6	209.35	2.49E-02	30	1223
178	1101	A	1	H	2	50	2	37.52	195.48	1.86E-02	30	1223
178	1101	A	1	H	2	55	2.05	3.67	147.23	1.45E-02	30	1223
178	1101	A	1	H	2	60	2.1	13.56	179.93	2.89E-02	30	1223
178	1101	A	1	H	2	65	2.15	19.81	216.99	4.08E-02	30	1223
178	1101	A	1	H	2	85	2.35	11.27	30.62	2.78E-02	30	1223
178	1101	A	1	H	2	90	2.4	4.27	347.45	1.49E-02	30	1223
178	1101	A	1	H	2	95	2.45	–44.31	166.14	4.51E-02	30	1223
178	1101	A	1	H	2	100	2.5	–59.2	151.61	6.34E-02	30	1223
178	1101	A	1	H	2	105	2.55	–76.38	96.19	5.78E-02	30	1223
178	1101	A	1	H	2	110	2.6	–70.68	77.63	5.83E-02	30	1223
178	1101	A	1	H	2	115	2.65	–60.55	83.59	5.93E-02	30	1223
178	1101	A	1	H	2	120	2.7	–67.32	71.78	5.19E-02	30	1223
178	1101	A	1	H	2	125	2.75	–74.73	65.73	4.41E-02	30	1223
178	1101	A	1	H	2	130	2.8	–64.24	81.42	4.67E-02	30	1223
178	1101	A	1	H	3	10	3.1	–53.71	21.17	4.02E-02	30	1224
178	1101	A	1	H	3	15	3.15	–46.94	23.67	4.61E-02	30	1224
178	1101	A	1	H	3	20	3.2	–47.35	26.79	4.79E-02	30	1224
178	1101	A	1	H	3	25	3.25	–59.41	26.37	5.23E-02	30	1224
178	1101	A	1	H	3	30	3.3	–55.89	29.69	5.99E-02	30	1224
178	1101	A	1	H	3	35	3.35	–58.46	33.01	6.79E-02	30	1224
178	1101	A	1	H	3	40	3.4	–65.55	43.44	7.79E-02	30	1224
178	1101	A	1	H	3	45	3.45	–64.2	39.13	9.30E-02	30	1224
178	1101	A	1	H	3	50	3.5	–66.64	35.56	9.20E-02	30	1224
178	1101	A	1	H	3	55	3.55	–63.12	30.56	9.30E-02	30	1224
178	1101	A	1	H	3	60	3.6	–62.28	34.5	9.44E-02	30	1224
178	1101	A	1	H	3	65	3.65	–63.95	27.77	8.31E-02	30	1224
178	1101	A	1	H	3	70	3.7	–69.42	26.36	6.28E-02	30	1224
178	1101	A	1	H	3	75	3.75	–73.98	63.21	8.76E-02	30	1224
178	1101	A	1	H	3	80	3.8	–74.38	56.48	1.22E-01	30	1224
178	1101	A	1	H	3	85	3.85	–78.81	50.27	1.31E-01	30	1224
178	1101	A	1	H	3	90	3.9	–75.28	64.87	1.23E-01	30	1224
178	1101	A	1	H	3	95	3.95	–66.83	58.11	1.02E-01	30	1224

Note: Only a portion of this table appears here. The complete table is available in ASCII format in the **TABLES** directory.

Table T9. Discrete sample NRM and AF demagnetization results for Hole 1101A.

Leg	Site	Hole	Core	Type	Section	Interval (cm)	Depth (mbsf)	Inclination (°)	Declination (°)	Intensity (A/m)	Mx (A·m)	My (A·m)	Mz (A·m)	Demagnetization step (mT)
178	1101	A	8	H	3	90	61.1	68.15	292.65	2.10E-01	2.40E-07	–5.76E-07	1.56E-06	0
178	1101	A	8	H	3	90	61.1	61.23	291.76	1.16E-01	1.66E-07	–4.16E-07	8.16E-07	10
178	1101	A	8	H	3	90	61.1	62	291.92	9.58E-02	1.34E-07	–3.34E-07	6.76E-07	20
178	1101	A	8	H	3	90	61.1	63.39	293.15	6.98E-02	9.84E-08	–2.30E-07	4.99E-07	30
178	1101	A	8	H	3	90	61.1	64.71	290.14	5.08E-02	5.98E-08	–1.63E-07	3.68E-07	40
178	1101	A	8	H	3	90	61.1	64.19	291.84	3.41E-02	4.42E-08	–1.10E-07	2.45E-07	50
178	1101	A	8	H	3	90	61.1	72.33	285.2	2.54E-02	1.62E-08	–5.95E-08	1.94E-07	60
178	1101	A	8	H	3	90	61.1	69.25	304.72	1.40E-02	2.27E-08	–3.27E-08	1.05E-07	70
178	1101	A	8	H	3	90	61.1	79.95	256.24	1.97E-02	–6.56E-09	–2.68E-08	1.56E-07	80
178	1101	A	20	X	3	116	173.86	51.03	342.58	4.85E-02	2.33E-07	–7.30E-08	3.02E-07	0
178	1101	A	20	X	3	116	173.86	–53.72	340.65	2.59E-02	1.16E-07	–4.07E-08	–1.67E-07	10
178	1101	A	20	X	3	116	173.86	–67.07	342.51	2.60E-02	7.72E-08	–2.43E-08	–1.91E-07	20
178	1101	A	20	X	3	116	173.86	–73.73	342.45	2.07E-02	4.42E-08	–1.40E-08	–1.59E-07	30
178	1101	A	20	X	3	116	173.86	–75.1	347.92	1.49E-02	3.00E-08	–6.43E-09	–1.15E-07	40
178	1101	A	20	X	3	116	173.86	–78.66	345.02	1.06E-02	1.60E-08	–4.29E-09	–8.28E-08	50
178	1101	A	20	X	3	116	173.86	–65.75	28.31	4.59E-03	1.33E-08	7.16E-09	–3.35E-08	60
178	1101	A	20	X	3	116	173.86	–47.06	355.6	9.36E-03	5.09E-08	–3.92E-09	–5.48E-08	70
178	1101	A	20	X	3	116	173.86	79.01	357.31	3.46E-03	5.28E-09	–2.48E-10	2.72E-08	80
178	1101	A	22	X	1	62	189.52	–75.6	318.64	5.62E-02	8.38E-08	–7.38E-08	–4.35E-07	0
178	1101	A	22	X	1	62	189.52	–84.39	7.18	9.13E-02	7.09E-08	8.93E-09	–7.27E-07	10
178	1101	A	22	X	1	62	189.52	–84.62	8.83	7.23E-02	5.36E-08	8.33E-09	–5.76E-07	20
178	1101	A	22	X	1	62	189.52	–84.84	14.41	5.15E-02	3.59E-08	9.22E-09	–4.10E-07	30
178	1101	A	22	X	1	62	189.52	–84.72	16.71	3.63E-02	2.56E-08	7.68E-09	–2.89E-07	40
178	1101	A	22	X	1	62	189.52	–84.85	23.19	2.40E-02	1.58E-08	6.79E-09	–1.91E-07	50
178	1101	A	22	X	1	62	189.52	–84.32	34.14	1.48E-02	9.71E-09	6.58E-09	–1.18E-07	60
178	1101	A	22	X	1	62	189.52	–84.97	18.98	1.01E-02	6.66E-09	2.29E-09	–8.01E-08	70
178	1101	A	22	X	1	62	189.52	–75.06	61.85	4.37E-03	4.26E-09	7.96E-09	–3.38E-08	80
178	1101	A	24	X	1	139	209.49	24.07	146.91	3.02E-02	–1.85E-07	1.21E-07	9.86E-08	0
178	1101	A	24	X	1	139	209.49	–69.55	169.34	3.56E-02	–9.78E-08	1.84E-08	–2.67E-07	10
178	1101	A	24	X	1	139	209.49	–71.66	166.64	2.74E-02	–6.70E-08	1.59E-08	–2.08E-07	20
178	1101	A	24	X	1	139	209.49	–71.56	169.5	1.81E-02	–4.51E-08	8.37E-09	–1.38E-07	30
178	1101	A	24	X	1	139	209.49	–67.68	171.42	1.19E-02	–3.57E-08	5.38E-09	–8.79E-08	40
178	1101	A	24	X	1	139	209.49	–65.39	193.9	6.68E-03	–2.16E-08	–5.35E-09	–4.86E-08	50
178	1101	A	24	X	1	139	209.49	–60.34	161.72	2.18E-03	–8.20E-09	2.71E-09	–1.52E-08	60
178	1101	A	24	X	1	139	209.49	–72.92	326.49	2.82E-03	5.53E-09	–3.66E-09	–2.16E-08	70
178	1101	A	24	X	1	139	209.49	78.84	211.96	2.83E-03	–3.72E-09	–2.32E-09	2.22E-08	80

Note: This table also appears in ASCII format in the **TABLES** directory.

Table T10. Results from the principal component analysis of discrete paleomagnetic samples.

Leg	Site	Core	Type	Section	Interval (cm)	Depth (mbsf)	Inclination (°)	Declination (°)	MAD	Length	Devang	Steps	Low	High	Option
178	1101A	8	H	3	90	61.1	57.5	294.6	1.44	7.77E-01	8.28	4	20	80	FRE
178	1101A	20	X	3	116	173.86	–80.6	339.8	5.51	1.81E-01	8.99	4	40	80	FRE
178	1101A	22	X	1	62	189.52	–85.1	2.8	0.37	4.72E-01	1.87	4	30	80	FRE
178	1101A	24	X	1	139	209.49	–73.7	165.7	1.51	2.99E-01	4.31	4	20	80	FRE

Notes: MAD = maximum angular deviation, Devang = deviation angle (degrees). This table also appears in ASCII format in the **TABLES** directory.

Table T11. Depths of geomagnetic reversals in Hole 1101A.

Chron	Depth interval (mbsf)	Age (Ma)
C1n(o)	55.05-55.10	0.78
C1r.1n(t)	71.05-71.35	0.99
C1r.1n(o)	75.90-76.40	1.07
C2n(t)	121.20-121.25	1.77
C2n(o)	126.95-127.00	1.95
C2r.1n(t)	—	2.14
C2r.1n(o)	—	2.15
C2An.1n(t)	165.95-166	2.581
C2An.1n(o)	209.30-209.50	3.04

Notes: Ages after Berggren et al. (1995). (t) = termination, (o) = onset, — = chron not interpreted in this interval.

Table T12. Headspace gas concentrations for Hole 1101A.

Core, section, interval (cm)	Depth (mbsf)	Methane (ppm)	Ethane (ppm)
178-1101A-			
1H-6, 0-5	7.50	3	0
2H-6, 0-5	16.20	4	0
3H-6, 0-5	25.70	3	0
4H-6, 0-5	35.20	3	0
6H-6, 0-5	45.70	5	0
7H-4, 0-5	52.20	8	0
8H-4, 0-5	61.70	12	0
9H-4, 0-5	71.20	26	0
10H-4, 0-5	80.70	20	0
11H-4, 0-5	90.20	14	0
12H-4, 0-5	99.70	13	0
13H-4, 0-5	109.20	11	0
14H-4, 0-5	118.70	74	0
15H-5, 0-5	128.33	1,570	0
16H-3, 0-5	136.20	1,900	0
17X-4, 0-5	147.20	4,290	1
18X-4, 0-5	155.00	3,590	1
19X-3, 0-5	163.10	22,100	5
20X-4, 0-5	174.20	17,200	4
21X-4, 0-5	183.80	19,200	4
22X-4, 0-5	193.40	21,000	4
23X-4, 0-5	203.00	28,100	5
24X-4, 0-5	212.60	20,400	4

Table T13. Summary of inorganic carbon, carbonate, and total organic carbon analyses for Hole 1101A. (Continued on next page.)

Core, section, interval (cm)	Depth (mbsf)	IC (wt%)	$CaCO_3$ (wt%)	TC (wt%)	TOC (wt%)
178-1101A-					
1H-1, 45-46	0.45	0.04	0.34	0.19	0.15
1H-3, 45-46	3.45	0.09	0.76	0.22	0.13
1H-5, 45-46	6.45	0.20	1.70	0.43	0.23
2H-1, 93-94	9.63	0.05	0.38	0.15	0.11
2H-3, 93-94	12.63	0.10	0.87	0.27	0.16
2H-5, 92-94	15.62	0.08	0.67	0.18	0.10
3H-1, 80-81	19.00	0.30	2.51	0.47	0.17
3H-3, 80-81	22.00	0.03	0.28	0.11	0.08
3H-5, 80-81	25.00	0.05	0.38	0.19	0.14
4H-1, 110-111	28.80	0.10	0.86	0.24	0.14
4H-3, 110-111	31.80	0.11	0.91	0.22	0.11
4H-5, 110-111	34.80	0.07	0.59	0.27	0.20
4H-7, 70-71	37.40	0.37	3.12	0.49	0.11
5H-1, 48-49	37.68	0.10	0.85	0.32	0.21
6H-2, 47-48	40.17	0.18	1.51	0.28	0.10
6H-4, 47-48	43.17	0.09	0.72	0.24	0.16
6H-6, 46-48	46.16	0.12	1.03	0.39	0.27
7H-1, 19-21	47.89	0.11	0.92	0.23	0.12
7H-3, 19-20	50.89	0.05	0.38	0.25	0.20
7H-4, 110-111	53.30	0.29	2.41		
7H-4, 140-141	53.60	1.18	9.82		
7H-5, 11-12	53.81	0.49	4.04		
7H-5, 40-41	54.10	0.06	0.53	0.09	0.03
7H-5, 70-71	54.40	0.11	0.91		
7H-5, 101-102	54.71	0.36	3.00		
7H-5, 134-135	55.04	0.87	7.23		
7H-6, 14-15	55.34	0.05	0.42		
7H-6, 100-101	56.20	0.13	1.11		
7H-6, 130-131	56.50	0.19	1.56		
7H-7, 11-12	56.81	1.98	16.50		
7H-7, 40-41	57.10	0.07	0.54		
7H-7, 70-71	57.40	0.06	0.48		
8H-2, 28-29	58.98	0.10	0.86	0.45	0.34
8H-4, 35-36	62.05	0.08	0.67	0.23	0.15
8H-6, 100-100.5	65.70	0.09	0.77	0.28	0.19
9H-2, 30-31	68.50	0.21	1.72		
9H-2, 60-61	68.80	1.55	12.87		
9H-2, 94-95	69.14	0.03	0.22	0.25	0.22
9H-3, 60-61	70.30	0.14	1.14		
9H-3, 102-103	70.72	0.54	4.50		
9H-3, 134-135	71.04	0.50	4.12		
9H-4, 23-24	71.43	0.08	0.67	0.11	0.03
9H-4, 60-61	71.80	0.20	1.65		
9H-4, 98-99	72.18	2.06	17.12	1.95	0.00
9H-4, 123-124	72.43	0.20	1.67		
9H-6, 95-96	75.15	0.09	0.73	0.27	0.18
10H-1, 15-16	76.35	0.84	7.03		
10H-1, 48-49	76.68	0.07	0.60		
10H-1, 120-121	77.40	0.04	0.30	0.11	0.07
10H-3, 118-119	80.38	2.69	22.37	2.86	0.18
10H-5, 120-121	83.40	0.11	0.93	0.27	0.16
10H-6, 117-118	84.87	1.94	16.19		
11H-1, 121-122	86.91	0.08	0.63		
11H-3, 46-47	89.16	0.10	0.83	0.18	0.08
11H-4, 17-18	90.37	0.48	3.98		
11H-4, 47-48	90.67	2.05	17.09		
11H-4, 78-79	90.98	3.01	25.05		
11H-4, 110-111	91.30	0.84	7.00		
11H-4, 140-141	91.60	0.05	0.43		
11H-5, 121-122	92.91	0.19	1.56		
11H-6, 2-3	93.22	0.10	0.84		
11H-6, 30-31	93.50	0.07	0.61		
11H-6, 59-60	93.79	3.33	27.72		
11H-6, 88-89	94.08	2.44	20.32		
12H-1, 120-121	96.40	0.07	0.62		

Table T13 (continued).

Core, section, interval (cm)	Depth (mbsf)	IC (wt%)	$CaCO_3$ (wt%)	TC (wt%)	TOC (wt%)
12H-2, 33-34	97.03	2.51	20.87		
12H-2, 64-65	97.34	1.40	11.62		
12H-2, 94-95	97.64	0.22	1.85		
12H-3, 55-56	98.75	0.97	8.09		
12H-3, 90-91	99.10	1.86	15.52		
12H-3, 120-121	99.40	0.07	0.55	0.08	0.02
12H-5, 40-41	101.60	0.38	3.20		
12H-5, 70-71	101.90	0.24	1.96		
12H-5, 100-101	102.20	0.06	0.46		
12H-7, 50-51	104.70	0.31	2.61		
13H-1, 121-122	105.91	0.11	0.90		
13H-2, 136-137	107.56	0.43	3.61		
13H-3, 15-16	107.85	1.26	10.50		
13H-3, 45-46	108.15	0.90	7.47	0.85	0.00
13H-3, 69-70	108.39	0.09	0.73		
13H-4, 140-141	110.60	1.33	11.12		
13H-5, 21-22	110.91	2.21	18.37		
13H-5, 54-55	111.24	0.48	3.98		
13H-5, 121-122	111.91	0.06	0.51		
14H-2, 109-110	116.79	0.24	2.01	0.22	0.00
14H-4, 45-46	119.15	0.83	6.93		
14H-4, 75-76	119.45	0.67	5.59		
14H-4, 121-122	119.91	0.06	0.47		
14H-5, 91-92	121.11	1.47	12.21		
14H-6, 46-47	122.16	0.05	0.38		
15H-1, 100-101	124.70	0.14	1.17		
15H-3, 44-45	127.14	0.07	0.57	0.06	0.00
15H-5, 40-41	128.73	0.06	0.54		
15H-7, 43-44	131.70	0.10	0.87		
16H-1, 67-68	133.87	5.60	46.69		
16H-1, 90-91	134.10	0.12	1.02		
16H-1, 120-121	134.40	0.04	0.35		
16H-1, 147-148	134.67	0.03	0.25		
16H-3, 41-41	136.61	0.04	0.35	0.21	0.17
16H-3, 90-91	137.10	0.12	0.96		
16H-7, 28-29	140.17	0.05	0.41		
17X-1, 104-105	143.74	0.06	0.48		
17X-3, 104-105	146.74	0.05	0.41	0.15	0.10
17X-5, 104-105	149.74	0.06	0.47		
17X-7, 29-30	151.99	0.04	0.34		
18X-2, 46-47	152.46	0.10	0.85	0.32	0.22
18X-4, 46-47	155.46	0.06	0.53		
18X-6, 46-47	158.46	0.06	0.53		
19X-1, 60-61	160.70	0.05	0.43		
19X-3, 60-61	163.70	0.04	0.29	0.29	0.25
19X-5, 30-31	166.40	0.00	0.00		
21X-1, 45-46	179.75	0.03	0.24	0.31	0.28
21X-3, 17-18	182.47	0.05	0.42		
21X-5, 52-53	185.82	0.04	0.36		
22X-1, 57-58	189.47	0.04	0.36	0.22	0.17
22X-3, 130-131	193.20	0.03	0.26		
22X-5, 76-77	195.66	0.03	0.26		
23X-1, 14-15	198.64	0.04	0.34	0.41	0.37
23X-3, 81-82	202.31	0.03	0.24		
23X-5, 106-107	205.56	0.04	0.33		
24X-1, 49-50	208.59	0.05	0.43	0.45	0.40
24X-3, 39-40	211.49	0.03	0.25		
24X-5, 131-132	215.41	0.03	0.21		

Notes: IC = inorganic carbon, $CaCO_3$ = calcium carbonate, TOC = total organic carbon, TC = total carbon, TS = total sulfur. * = samples collected in a second round of sampling.

Table T14. Results of interstitial water analyses for Hole 1101A.

Core, section, interval (cm)	Depth (mbsf)	pH	Salinity	Cl^- (mM)	Alkalinity (mM)	NH_4^+ (mM)	$Si(OH)_4$ (mM)	SO_4^{2-} (mM)	Mn^{2+} (μM)	Fe^{2+} (μM)	PO_4^{3-} (μM)	F^- (μM)	Ca^{2+} (mM)	Mg^{2+} (mM)	K^+ (mM)	Sr^{2+} (μM)
178-1101A-																
1H-2, 145-150	2.95	7.8	34.5	557	3.80	0.04	0.58	27.8	78	0.8	24.5	58.5	11.8	53.1	12.6	87
1H-5, 145-150	7.45	7.8	34.5	556	4.04	0.09	0.49	27.8	169	0.4	29.6	49.6	9.9	52.8	12.5	87
2H-2, 145-150	11.65	7.8	35.0	559	4.64	0.14	0.70	28.8	172	2.2	14.8	38.2	12.9	52.3	12.5	87
2H-5, 145-150	16.15	7.8	35.0	561	5.03	0.14	0.81	26.9	126	1.2	15.7	31.8	13.2	49.4	12.1	87
3H-2, 145-150	21.15	7.8	35.0	560	5.01	0.23	0.63	27.1	151	0.0	11.1	27.0	14.3	50.4	11.9	87
3H-5, 145-150	25.65	7.6	35.0	565	5.23	0.25	0.78	28.5	141	1.6	10.7	22.6	13.7	48.5	12.0	86
4H-2, 145-150	30.65	7.8	34.5	562	5.36	0.30	0.64	21.8	122	0.1	9.1	20.6	14.2	47.7	11.7	86
4H-6, 145-150	36.65	7.9	34.0	563	5.08	0.28	0.62	21.5	78	0.2	6.8	16.9	14.7	47.6	11.3	86
6H-2, 145-150	41.15	7.9	34.5	566	5.31	0.39	0.70	21.2	92	0.1	6.0	15.3	14.4	46.4	11.4	86
6H-5, 145-150	45.65	8.1	34.0	567	5.39	0.41	0.56	19.0	61	0.0	3.6	14.3	13.5	42.9	11.7	83
7H-3, 145-150	52.15	8.0	34.0	565	5.71	0.48	0.69	17.8	64	0.1	6.2	11.2	13.5	41.6	10.2	84
8H-3, 145-150	61.65	8.1	33.0	561	5.51	0.52	0.76	16.9	49	0.0	3.4	10.2	13.6	39.3	10.5	84
9H-3, 145-150	71.15	8.0	33.0	562	5.53	0.56	0.76	11.6	37	0.2	3.9	9.8	11.6	35.8	8.9	81
10H-3, 145-150	80.65	7.8	32.5	565	4.72	0.62	0.81	11.8	28	6.6	2.4	8.7	12.5	38.7	8.6	81
11H-3, 145-150	90.15	7.9	32.0	563	5.39	0.69	0.81	9.0	25	0.6	2.7	10.4	14.0	38.0	8.9	84
12H-3, 145-150	99.65	7.9	32.0	565	5.57	0.71	0.84	6.4	17	0.4	3.0	10.2	11.4	36.2	8.6	82
15H-3, 145-150	128.15	7.9	32.0	565	7.05	0.97	0.87	1.7	15	1.3	3.8	8.6	9.3	31.3	7.9	103
18X-3, 145-150	154.95	7.9	32.0	555	7.31	1.01	1.00	1.0	21	0.4	6.4	6.9	9.1	29.2	7.7	96
21X-3, 145-150	183.75	7.8	32.0	553	7.74	1.29	1.01	1.5	14	1.9	3.1	8.8	10.7	29.1	7.8	101
24X-3, 145-150	212.55	8.0	32.0	557	8.03	1.55	1.00	2.8	18	2.1	1.9	8.3	11.8	28.1	8.3	103

Table T15. Relative intensities of selected X-ray diffraction peaks from clay mineral samples of Site 1101 sediments.

Core, section, interval (cm)	Depth (mbsf)	Chlorite (7 Å)	Illite (5 Å)	Mixed layer (~12 Å)
178-1101A-				
10H-2, 14-16	77.84	100	12	28
10H-2, 86-88	78.56	100	15	31
10H-3, 40-42	79.60	100	16	45
10H-3, 86-88	80.06	100	22	55
10H-3, 118-120	80.38	100	21	89
10H-3, 141-143	80.61	100	24	76
10H-4, 15-17	80.85	100	25	73
10H-4, 40-42	81.10	100	31	67
10H-4, 64-66	81.34	100	23	64
10H-4, 77-79	81.47	100	20	51
10H-4, 101-103	81.71	100	14	57
10H-4, 129-131	81.99	100	14	41
17X-2, 60-62	144.80	100	20	70
17X-4, 60-62	147.80	100	10	30
20X-5, 138-140	176.98	100	14	34
20X-6, 138-140	178.58	100	9	45

Note: Highest selected peak intensity is normalized to 100.

Table T16. Sedimentation rates calculated from geomagnetic polarity transition data.

Depth (mbsf)	Age (Ma)	Chron	SR (cm/k.y.)
0	0		
			7.1
55.08	0.78	C1n(o)	
			7.7
71.20	0.99	C1r.1n(t)	
			6.2
76.15	1.07	C1r.1n(o)	
			6.4
121.12	1.77	C2n(t)	
			3.2
126.98	1.95	C2n(o)	
			6.2
165.98	2.581	C2An.1n(t)	
			9.5
209.40	3.04	C2An.1n(o)	

Note: SR = sedimentation rate.

Table T17. Sedimentation rates calculated from diatom datums.

Depth (mbsf)	SR (cm/k.y.)	Age (Ma)	Comments
0.00		0.00	Top of hole
	10.9		
20.80		0.19	T *Hemidiscus karstenii*
	0.7		
23.80		0.64	T *Actinocyclus ingens*
	7.8		
112.88		1.78	T *Actinocyclus karstenii*
	8.9		
119.14		1.85	T *Thalassiosira torokina*
	4.9		
184.20		3.17	B *Thalassiosira vulnifica*
	10.4		
208.23		3.40	B *Thalassiosira insigna*

Note: SR = sedimentation rate, T = top/last occurrence, B = base/first occurrence.

Table T18. Sedimentation rates (cm/k.y.) calculated from calcareous nannofossil datums.

Depth (mbsf)	SR (cm/k.y.)	Age (Ma)	Comments
0.0		0.00	Top of hole
	6.0		
15.6		0.26	B *Emiliania huxleyi*
	7.7		
90.9		1.24	T large *Gephyrocapsa*
	2.0		
95.2		1.46	B large *Gephyrocapsa*

Note: SR = sedimentation rate, T = top/last occurrence, B = base/first occurrence.

Table T19. Two-way traveltime (TWT) and depth to base of seismic units at Site 1101.

Seismic Unit	TWT (ms)	Depth (mbsf)	Age (Ma)
Unit I	100	78.6	1.10
Unit II	178	141.0	2.16
Base of hole	272	217.7	3.10

Note: Ages according to magnetic reversal identifications (Table **T16,** p. 80).